Photoelectron Calculations for the ZEUS Calorimeter

by

Marc St-Laurent
Department of Physics, McGill University
Montréal, Québec
August 1993

A Thesis submitted to the
Faculty of Graduate Studies and Research
in partial fulfillment of the requirements for the degree of
Master of Science

Abstract

Two different methods for calculating the number of photoelectrons per GeV for the PMTs of the ZEUS calorimeter are described. The first uses laser data taken at DESY Hall II during the cosmic ray tests of the forward and rear calorimeters. The second uses the signal from the radioactive decay of the depleted uranium in the calorimeter. This quantity is a measure of the gain of the PMT and can be used as a monitor of PMT gain variations. Results from the two methods are compared with other methods in use at ZEUS.

Résumé

Deux méthodes de calcul du nombre de photoélectrons par GeV des photomultiplicateurs du calorimètre de ZEUS sont décrits. La première méthode utilise les données obtenues avec un laser lors des tests avec rayons cosmiques des calorimètres avant et arrière du détecteur ZEUS. La deuxième utilise le signal de la désintégration de l'uranium dans le calorimètre. Le nombre de photoélectrons par GeV est une mesure du gain d'un photomultiplicateur et permet aussi de mesurer les variations du gain de celui-ci. Des résultats des deux méthodes sont comparés a ceux obtenus avec d'autres méthodes utilisées pour ZEUS.

Contents

Acknowledgements

This thesis would not have been possible were it not for the contributions made by many people.

I would like to thank the members of the ZEUS collaboration for the many years spent planning, testing and building the ZEUS detector. I would like to thank in particular my supervisor, David Hanna, for allowing me to participate in this most exciting world of experimental particle physics as well as providing me with guidance and advice during the course of this work (and also for displaying remarkable patience on occasion!). He also introduced me to the Hall II method described in this thesis.

I would also like to express my gratitude to Alan Caldwell for pioneering the UNO model and Reena Meijer-Drees for showing me the ropes back in February, she also contributed to the "means and sigmas" code in the transputers which plays a central role in the application of the UNO method. I would also like to thank Andres Kruse for doing much of the work related to the calorimeter transputer readout.

In addition, I would like to thank my collegues of the Laser group for letting me use their data for comparison purposes as well as for their helpful advice.

Coming to Germany and living away from home for the first time might not have been as easy and fun as it has been were it not for my fellow Canadian collegues who where always available with helpful advice or at least a good laugh. I would also like to thank my German hosts for making me feel welcome and quite at home.

Finally, I would like to thank my family and friends back home for cheering me on throughout this entire project.

Foreword

High energy physics experiments involve large, complex detectors. In order to measure the kinematic variables of the the decay products of the collisions produced at these experiments, one requires accurate calibration of the detector. One also requires good monitoring to maintain the calibration and detect problems in the detector as they occur.

The high resolution compensating calorimeter is the center-piece of the ZEUS detector. It measures the energy and timing of the final state products of collisions. Each part of the readout must be well calibrated in order to provide meaningful results. The signals produced in the calorimeter are ultimately sent to photomultiplier tubes (PMTs) which amplify these signals to levels easily measured by the subsequent electronics. Clearly the gain of these PMTs is a important quantity in the overall calibration.

In this thesis, two different methods of calculating the number of photoelectrons per GeV of deposited energy for each PMT (denoted n_{pe}) are described. This quantity is related to the gain of the PMT (in the simplest model, it is simply the inverse of the PMT gain). The number of photoelectrons per GeV and can also be used as a monitor of variations in the PMT gain.

In the first chapter, an introduction to the HERA electron proton collider is given, followed by a brief discussion of some of the physics of electron proton collisions and concludes with an overview of the ZEUS detector.

The next chapter discusses the ZEUS calorimeter in more detail, first giving a review of calorimetry followed by a description of the relevant components to this thesis. Also a description of the monitoring systems is given, concentrating mainly on the laser system.

Chapter three describes the two methods and presents some results from each.

Finally, in chapter four, comparisons of the two methods to other methods used to determine the quantity n_{pe} are presented followed by the conclusions of the thesis.

Chapter 1

Electron–Proton Physics at HERA

1.1 Introduction

To understand the fundamental structure of matter has been one of mankind's greatest quests. From the ancient Greeks to present-day particle physics, much effort and thought has gone into finding an answer to the question *What's it all made of?*.

In the last hundred years, our understanding has increased by leaps and bounds. From Mendeleev's Periodic Table, to the simple electron, proton, neutron model of the atom, followed by the "zoo" of sub-atomic particles discovered in the fifties and sixties to our present Standard Model with its quarks, leptons and gauge bosons, we have delved deep into the structure of matter in our quest.

The current picture of the fundamental constituents of matter is summarized in table 1.1. According to this model, all matter is made up of 6 quarks, 6 leptons and their antiparticles. These particles experience forces through the exchange of gauge bosons, each associated with the one of the four fundamental forces [1]. The leptons, such as the electron, the muon or the various neutrinos are believed to be fundamental as they continue to exhibit point-like properties in experiments, whereas hadrons

[1] Gravity is not described within the standard model as the strength of gravitational interactions is negligible on the scale of the other interactions and theoretical problems exist in the formulation of a quantum theory of gravity (using the so-called "gravitons" as mediator).

	Leptons	
e (electron)	μ (muon)	τ (tau)
ν_e (e-neutrino)	ν_μ (μ-neutrino)	ν_τ (τ-neutrino)
	Quarks	
u (up)	c (charm)	t (top)[2]
d (down)	s (strange)	b (beauty)
	Gauge Bosons	
γ (photon)		
$W^{\pm}$,Z (weak bosons)		
g_i (i = 1,...,8 gluons)		

Table 1.1: Fundamental particles of the Standard Model. Note that to each of these there is a corresponding antiparticle (usually denoted with an overlying bar as $\bar{u}$).

(protons, neutrons, pions etc ...) have since been shown to be composite structures and can be described as bound-state combinations of quarks "glued" together by the strong nuclear force.

A large part of this knowledge was obtained from experiments involving the scattering of leptons off stationary proton targets. In these experiments the typical centre-of-mass energies never exceeded $\sqrt{s} = 2\sqrt{E_l m_p} \simeq 30\ GeV$ and the square of the momentum transfer between lepton and proton, Q^2,was limited to $\simeq (20\ GeV/c)^2$. This was enough, however, to show that the cross-section measurements were not consistent with scattering from point-like protons but rather from a composite structure of point-like partons, as they were called, which later were identified with Murray Gell-Mann's "quarks" [17],[9].

[2]The top quark has not yet been detected experimentally.

1.2 The HERA Collider

On the 31st of May of 1992, the HERA collider began operation. The two experiments *H1* and *ZEUS* observed collisions of beams of protons and electrons for the first time, opening up new frontiers in lepton–hadron scattering previously unseen in traditional fixed target experiments. HERA is the first electron proton collider ever constructed, it is also the first collider to make extensive use of industry produced superconducting magnets [20].

1.2.1 A Brief History of HERA

The HERA project was approved and construction began in April of 1984. The tunnel was completed in August 1987. By 1988 the electron ring with its conventional magnet system was in operation. The superconducting proton ring was completed in 1990 and the first protons were stored in April 1991 at an energy of 40 GeV. By the end of 1991, HERA was operating with energies of 26.6 GeV and 480 GeV for the electron and proton beams respectively and a luminosity $L = 2 \cdot 10^{28}\ cm^{-1}s^{-1}$. The collider was subsequently shut down for a period of 4 months to allow for the installation of the H1 and ZEUS detectors [25].

1.2.2 General Layout

The HERA collider is located at the Deutsches Elektronen–Synchrotron (DESY) in Hamburg, Germany. The physical layout of the collider is shown in figure 1.1.

Independent magnet systems guide beams of protons and electrons at nominal energies of 820 GeV and 30 GeV respectively [3] around the 6.3 km circumference ring. There are four interaction regions, two of which are occupied by the H1 and ZEUS experiments, while a third has been allocated to the HERMES experiment which has been recently approved.

[3] For the first running period the maximum electron energy was limited to 26.6 GeV by the available RF power.

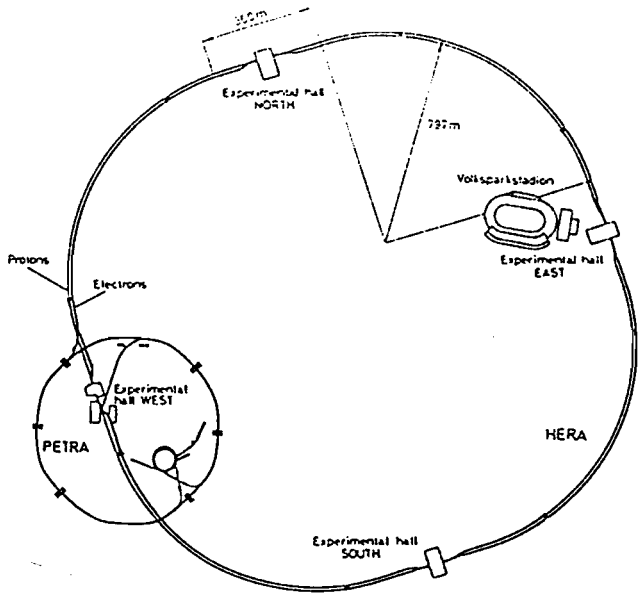

Figure 1.1: HERA Layout

The pre-existing accelerators in the DESY and PETRA rings were modified to serve as electron injectors, while an entirely new chain of accelerators (in the same tunnels) were built for proton injection. It is worth noting that the particles in the beam do not form a continuous stream but are accelerated in "bunches" which cross the interaction regions at a rate of once every 96 ns. This collision rate is an order of magnitude greater than at any existing collider requiring novel techniques in triggering and data acquisition [25].

The principal operating parameters of HERA are shown in table 1.2 [20].

1.3 Electron-proton Scattering

1.3.1 Kinematics

At HERA, the proton beam with energies of up to 820 GeV, colliding with 30 GeV electrons yield centre-of-mass energies $\sqrt{s} = 2\sqrt{E_e m_p} \simeq 314\ GeV$ and Q^2 up to $10^5\ (GeV)^2$. For $e-p$ scattering, the lowest order diagrams are shown in figure 1.2. Generally, the final state lepton and the quark jet emerge opposite each other with

Parameter	p-ring		e -ring	units
Nominal energy	820		30	GeV
Energy range	300–820		10–33	GeV
Injection energy	40		14	GeV
c.m. energy		314		GeV
Luminosity		$1.5 \cdot 10^{31}$		$cm^{-2}s^{-1}$
Interaction points		4		
Crossing angle		0		$mrad$
Circumference		6336		m
Magnetic field	4.68		0.165	T
Number of particles	2.1		0.8	10^{13}
Number of bunch buckets		220		
Number of bunches		210		
Bunch crossing time		96		ns
RF–frequency	52.033/208.13		499.776	MHz
RF–power	1		13.2	MW
Filling time	20		15	min

Table 1.2: General Parameters of HERA Collider

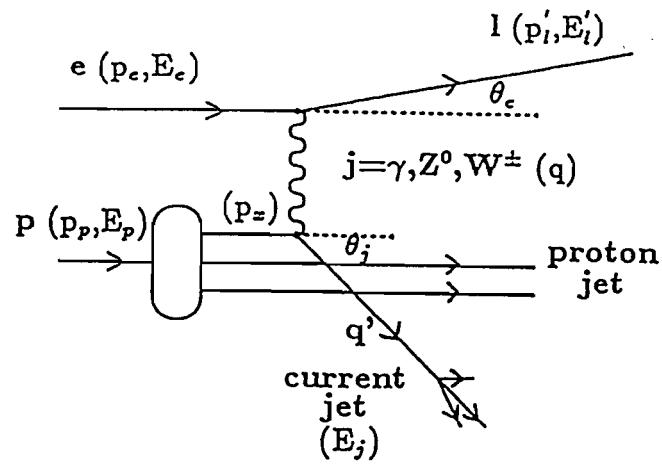

Figure 1.2: Feynman diagrams of the basic neutral current and charged current processes.

respect to the beam axis and the proton remnants continue down the beam pipe. In the case of the neutral current (NC) process (where the exchanged boson may be a γ or a Z^0) both the outgoing lepton and the quark jet are available for measurement. In contrast, the charged current process (CC), involving the exchange of a $W^{\pm}$, produces a neutrino as outgoing lepton, which escapes undetected. Thus the quality of the jet energy and direction measurements becomes very important. This means one must have good calorimetry and hence good calibration of the calorimeter as the higher energies attained limit the precision of tracking detectors and one has to rely on the calorimeter measurements.

It is useful to introduce here the various kinematic relations used in discussions of $e - p$ scattering.

The notation is as follows:

E = Energy m = rest mass

p = momentum 4-vector

subscript l = lepton subscript p = proton

subscript ν = neutrino

subscript e = electron

superscript prime = outgoing particle

The total invariant mass (cms) squared:

$$\begin{aligned} s &= (p_e + p_p)^2 \\ &\simeq 4E_eE_p \end{aligned}$$

the final form is used when one neglects the particle masses (which is an excellent approximation at HERA energies).

Square of 4-momentum transfer:

$$q^2 = (p_e - p_l')^2 = -Q^2$$

Square of total mass of final hadronic system:

$$W^2 = (q + p_p)^2$$

Energy transferred by the current in target (proton) rest frame:

$$\nu = \frac{q \cdot p_p}{m_p}$$

The maximum value ν can attain is given by:

$$\nu_{max} = 2E_eE_p/m_p$$

Note also the dimensionless Bjorken-x and y variables:

$$x = \frac{Q^2}{2(q \cdot p_p)} = \frac{Q^2}{2m_p\nu}$$

In the parton model, x, can be interpreted as the momentum fraction of the proton carried by the struck parton (quark).

$$y = \frac{(q \cdot p_p)}{(q \cdot pe)} = \nu/\nu_{max}$$

This variable is a measure of the inelasticity of the collision [26].

Note also that

$$Q^2 = sxy.$$

One can reconstruct the variables Q^2, x and y using several methods. For example, using the electron variables:

$$\begin{aligned} y_{elec} &= 1 - \frac{E_e'}{2E_e}(1 - \cos\theta) \\ Q^2_{elec} &= 2E_e E_e'(1 + \cos\theta) \\ x_{elec} &= x_0 \frac{E_e'(1 + \cos\theta)}{2E_e - E_e'(1 - \cos\theta)} \end{aligned}$$

where

$$x_0 = \frac{E_e}{E_p}$$

Or using the hadronic system [4] (such as when a charged current event occurs):

$$\begin{aligned} y_{JB} &= \frac{\sum_i (E_i - p_{zi})}{2E_e} \\ Q^2_{JB} &= \frac{(\sum_i p_{xi})^2 + (\sum_i p_{yi})^2}{1 - y_{JB}} \\ x_{JB} &= \frac{Q^2_{JB}}{s y_{JB}} \end{aligned}$$

where the sums run over all observed final state hadrons and the z-axis is in the proton beam direction [20].

1.3.2 Physics at HERA

Physics topics available at HERA include deep inelastic scattering (measurement of the proton structure functions), heavy quark spectroscopy, low-x physics, photoproduction as well as searches for exotic particles [26].

[4] This method is called the Jacquet-Blondel method [19]

In order to give some motivation for the usefulness of extending $e-p$ scattering to the ranges made available with HERA, it is instructive to compare the rates for γ and W exchange reactions. In this simplified discussion the cross-sections can be written as :

$$\begin{aligned}\frac{d\sigma(\gamma p)}{dxdy} &\simeq \alpha^2\frac{1}{Q^4}F(x,y)\\ \frac{d(Wp)}{dxdy} &\simeq \alpha^2(\frac{1}{Q^2+M_W^2})^2F(x,y)\end{aligned}$$

From the above, one can clearly see that for $Q^2 \to 0$ the NC process (γ exchange) dominates the CC process but as Q^2 increases, the two become comparable. Thus the study of electro-weak processes is possible at HERA.

More precise expressions for the cross sections can be written in terms of quark distribution functions. For example, the neutral current cross section can be written as:

$$\frac{d^2\sigma(\gamma+Z^0)}{dxdy} = \frac{4\pi\alpha^2}{sx^2y^2}\{(1-y)F_2(x,Q^2)+y^2xF_1(x,Q^2)\}$$

F_1 and F_2 are the so-called structure functions which can be re-expressed in terms of quark distribution functions as follows:

$$\frac{d^2\sigma(\gamma+Z^0)}{dxdy} = \frac{4\pi\alpha^2}{sx^2y^2}\sum_q\{xq(x)(A_q+(1-y)^2B_q)+x\bar{q}(x)(B_q+(1-y)^2A_q)\}$$

the A_q and B_q are constants that can be written in terms of the charges of the quarks and leptons as well as weak isospin and weak mixing angle.

For charged current processes the expression for the cross-section, expressed in terms of three structure functions, F_1, F_2 and F_3, is as follows:

$$\begin{aligned}\frac{d^2\sigma(e_L^-p\to\nu X)}{dxdy} &= \frac{G_F^2s}{\pi}\frac{1}{(1+\frac{Q^2}{M_W^2})^2}\\ &\{(1-y)F_2(x,Q^2)+y^2xF_1(x,Q^2)+(y-y^2/2)xF_3(x,Q^2)\}\end{aligned}$$

(Note that e_L denotes left-handed electrons since the cross section for right handed electrons vanishes due to the left-handedness of the neutrino.) The quark-parton

expressions for the structure functions are:

$$\begin{aligned} F_2(x) = 2xF_1(x) &= x[q(x) + \bar{q}(x)] \\ F_3(x) &= x[q(x) - \bar{q}(x)] \end{aligned}$$

where

$$\begin{aligned} q(x) &= u(x) + c(x) + \ldots \\ \bar{q}(x) &= \bar{d}(x) + \bar{s}(x) + \ldots \end{aligned}$$

Because of the large Q^2 range that is accessible at HERA, a stringent test of QCD will be possible. QCD predicts a logarithmic fall off of the structure functions as a function of Q^2. Gluon radiation leads to a scale breaking of the form:

$$F(x) \rightarrow \frac{F(x)}{1 + c\ln(Q^2/\Lambda^2)}$$

where Λ is the QCD scale parameter. Before HERA the available structure function data spanned the range $0 < Q^2 < 300\ GeV^2$. This range has been increased to 40000 GeV^2. If any variance from QCD predictions exists in this expanded Q^2 range, and is large enough, it will be measurable at HERA [26].

Other results from ZEUS include new mass limits on exotic particles such as excited electrons or leptoquarks and leptogluons, predicted by some extensions of the standard model [30],[31].

1.4 ZEUS

1.4.1 Requirements for HERA

The wide variety of reactions produced at HERA, as well as the need to detect and identify different types of particles (electron, photon, various hadrons) place different requirements on HERA's detectors. As an example, a typical deep inelastic scattering (DIS), neutral current (NC) event would produce a high energy electron whose transverse momentum (defined with respect to the beam direction) is balanced by the

current jet formed by the struck quark as it "hadronizes" producing several relatively grouped particles. The remnants from the break-up of the proton would travel mostly undetected down the beam pipe. To measure the kinematic variables of this type of event, one requires accurate electromagnetic and hadronic calorimeters. In the case of a CC event, only the current jet is observed (as the outgoing neutrino escapes undetected), thus one also requires a hermetic calorimeter. For the observation of low Q^2 processes, for example the production of pairs of heavy quark mesons, the deposited energy in the calorimeter is typically only a few GeV. Additional tracking information is therefore required for proper identification of particles.

Background is a major challenge at HERA, the ratio of interesting events compared to background events (typically the so-called "beam-gas" events–interactions of beam protons with residual gas in the beam pipe or interactions with the beam pipe wall) is very small (10^{-3} - 10^{-5}). These background events typically deposit large amounts of energy in the calorimeter and produce large numbers of tracks. In addition the collision rate is very high. This requires that the detectors be able to discriminate quickly - within microseconds - against backgrounds. This has lead to advances in signal processing techniques which will also prove useful for the next generation of pp colliders, SSC and LHC.

The design of both detectors at HERA is based around the calorimeters. ZEUS uses a compensating uranium-scintillator based design [5]. Compensation means that the calorimeter response to electromagnetic signals equals that of hadronic signals of the same energy (denoted by $e/h = 1$). H1 uses a liquid argon based calorimeter which, although non-compensating ($e/h \simeq 1.1 - 1.2$), allows for high segmentation. The responses are re-weighted off-line [25].

1.4.2 The Detector

[5] Refer to the next chapter for a definition of the various terms used here as well as a more detailed description of the ZEUS calorimeter

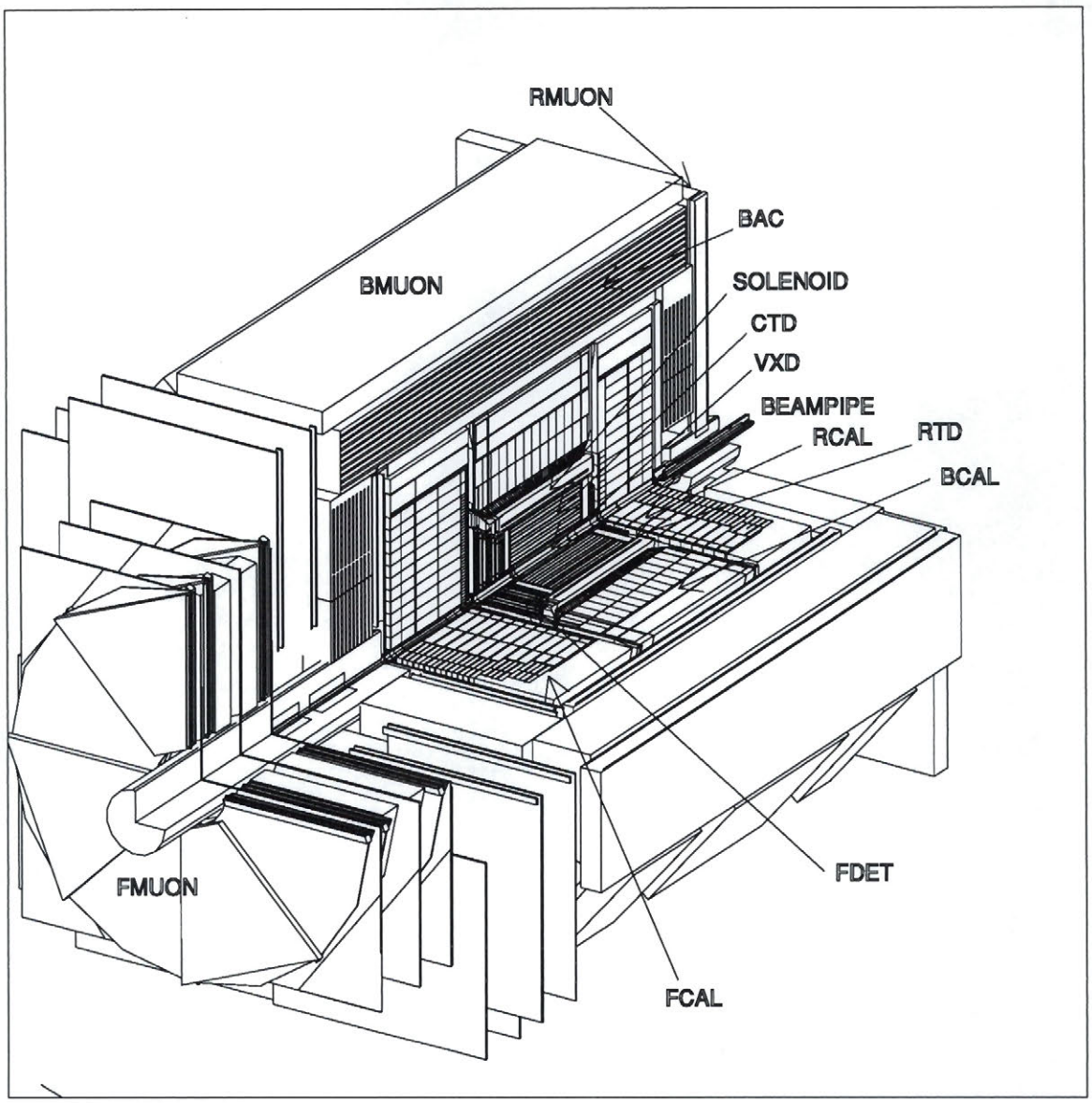

Figure 1.3: The ZEUS detector

A three dimensional view of the ZEUS detector is shown in figure 1.3. It was developed and constructed by a collaboration of nearly 50 institutes from 12 countries involving about 350 physicists. The asymmetry of the HERA collisions is reflected in the design of the detector, where more emphasis is placed on the forward (proton beam) direction. A description of the components of the detector follows.

Charged particle detection is provided by a number of subdetectors. Starting from the interaction region and moving outwards, the first of these is the Vertex Detector (VXD). Its primary function is the detection of short-lived particles in addition to improving momentum and angular resolution of charged tracks. It has a time expansion type drift cell structure. The VXD has 12 layers of sense wires, radially spaced 3 mm apart, with a wire length of 150 cm. The design position resolution is 50 μm.

Surrounding the VXD is the Central Tracking Detector (CTD). It consists of a cylindrical wire chamber with an outer radius of 85 cm and an overall length of 240 cm. Track position and $\frac{dE}{dx}$ losses are measured with nine superlayers, each with eight layers of sense wires. Five of the superlayers have wires parallel to the chamber axis and four have a small stereo angle. The stereo angle chosen (5°) is such that the angular resolution in polar and azimuthal angles are roughly equal. The position resolution of the CTD is 100-120 μm and its momentum resolution (at $\theta = 90°$) is $\sigma(p)/p = 0.0021p \oplus 0.0029\,(GeV/c)$.

In addition to the CTD are the forward and rear track detectors (FTD, RTD) consisting of three and one planar drift chambers respectively. Each chamber has 3 planes rotated by 60° with respect to each other. Each plane has 6 layers of sense wires. The design position resolution of 120 μm leads to a momentum resolution of $\sigma(p)/p = 0.01p$ at a forward angle of 140 $mrad$.

Enhancing electron identification in the forward direction is the Transition Radiation Detector (TRD). It consists of 4 modules sandwiched between the FTD chambers, improving hadron rejection by a factor of 30 at $p < 10\ GeV/c$.

Surrounding these detectors is a thin ($\sim 0.9X_0$ (radiation lengths)) superconducting solenoid of inner radius 86 cm and length 280 cm. Although it is capable of

providing a magnetic field of up to $1.8\,T$, mechanical constraints in the detector limit the field to $1.42\,T$.

This entire system is surrounded by the ZEUS high resolution calorimeter (CAL). It is a sampling type calorimeter consisting of depleted uranium (DU) plates clad in stainless steel as absorbing material interleaved with plastic scintillator (SCI) tiles as active layers. The tiles form towers which are read out by wavelength shifter bars (WLS) and light guides (LG) which carry the light signals to the photomultiplier tubes (PMTs).

The ratio of the thicknesses of the DU plates and SCI tiles ($3.3\,mm$ and $2.6\,mm$ respectively) was chosen in order to achieve compensation (based on prototype tests and monte carlo studies). The energy resolutions are $\sigma(E)/E = 0.18/\sqrt{E} \oplus 1\%\,GeV$ for electromagnetic signals and $\sigma(E)/E = 0.35/\sqrt{E} \oplus 2\%\,GeV$ for hadrons (which is currently the best hadron resolution in the world).

Identification of electrons within jets will be aided by the insertion of silicon pad detectors (the Hadron Electron Separator–HES) into the calorimeter. For RCAL and BCAL, the HES will be at a depth of $3X_0$ and for FCAL there are two HES planes at $3X_0$ and at $6X_0$. It has been shown that with a single plane HES, hadron rejection factors of 20-40 are achievable whereas a second plane increases the rejection by a factor of 6-10. Currently RHES is in the installation phase and FHES is in preparation. For BHES, alternate technologies are under study, as the large area that would need to be covered for BCAL renders the cost of using silicon pad techniques prohibitive.

The high resolution calorimeter is surrounded by the Backing Calorimeter (BAC), which measures the energy of late showering particles. The iron plates of the return yoke of the solenoid are used as absorber and readout is provided by aluminum tubes operating in proportional mode. The design energy resolution is $1.1/\sqrt{E}\,GeV$. The iron yoke consists of the bottom yoke, which supports the inner detector components and the retractable clam shells, which carry most of the backing calorimeter and muon detectors.

Muon identification is achieved in the forward direction in a spectrometer using drift and limited streamer tube chambers, interspersed between the magnetized iron yoke and toroids. The momentum resolutions for muons is $\simeq 25\%$ up to $100\,GeV/c$. In the barrel and rear areas, position and angle measurement of muons is provided by limited streamer tube chambers before and after the magnetized yoke. The momentum resolution in these regions is 20% at $20\,GeV/c$.

In addition to the main detector, are the electron and photon detectors installed at 38 and $108\,m$ downstream of ZEUS in the electron beam direction. These are used to measure the luminosity as well as tag small Q^2 and radiative processes. In the proton direction downstream with respect to ZEUS, is the Leading Proton Spectrometer (LPS), consisting of six measuring stations in the proton ring using miniature high resolution silicon strip detectors close to the beam. The LPS is used to detect very forward scattered protons that may be produced in diffractive photoproduction, photon gluon fusion as well as in neutral and charged current processes [32],[33].

Chapter 2

The High-Resolution ZEUS Calorimeter

2.1 Calorimetry

A basic definition of a calorimeter (as understood in high energy physics) can be given as an instrument that measures the energy of some incident particle or particles. With the higher energies available at particle colliders (such as HERA), calorimeters possess useful characteristics. Possibly the most important of these is the fact that the energy resolution improves with increasing energy[1]. In contrast, traditional magnetic spectrometers have a momentum resolution which scales as:

$$\frac{\sigma(p)}{p} \sim p$$

and thus degrades with increasing particle momentum (and hence energy). Calorimeters also possess the advantage of being sensitive to both charged and neutral particles, unlike tracking detectors which are only responsive to charged particles. Calorimeters are also well suited for the measurement of global event characteristics, such as the total transverse energy, total missing (transverse) energy, jet production etc. This is

[1] In the case of hadron calorimeters, one must modify the above statement to say compensating calorimeters; the importance of compensation will be discussed further.

especially relevant as modern experiments tend to produce more jet type reactions (with large multiplicities of particles leading to many tracks etc.). Yet another advantage of calorimeters is the fact that the depth required to contain a shower scales roughly as $\sim ln(E)$ with energy.

2.1.1 Sampling Calorimeters

One can classify calorimeters into one of two types. Homogeneous calorimeters use the entire volume of the detector to absorb the incident particle as well as read out the signal. Typical materials used for homogeneous calorimeters are BGO ($Bi_4Ge_3O_{12}$) crystals and lead glass blocks [27],[28],[11].

Sampling calorimeters use alternating active (or readout) layers where the energy of the showering particles is sampled and read out, and passive absorbing layers which are usually made of a dense material to promote showering. As mentioned before, the ZEUS calorimeter uses depleted uranium plates as absorber and plastic scintillator tiles as readout. The advantages gained in using a sampling calorimeter are in cost and size. Sampling calorimeters can be built large enough to contain the entire shower as well as cover the entire solid angle of the experiment using relatively inexpensive materials (such as plastic scintillator) whereas the equivalent homogeneous calorimeter would be prohibitively large and expensive.

Sampling Fraction

Only a small fraction of the particle energy is deposited in the active layers of a sampling calorimeter (for example, 4% for electrons in ZEUS). Of this, a small fraction is converted to light that yields a measurable signal in the PMTs. The ratio of visible (measurable) energy of a particle of type i in the active medium to the totally absorbed energy in the calorimeter is called the sampling fraction R_i. It depends on the material and thicknesses of the absorber and readout plates of the calorimeter as

well as particle type. It is defined as:

$$R_i = \frac{E_{vis,i}}{E_{abs,i}} = \frac{E_{vis,i}}{E_{invis,i} + E_{vis,i}}$$

where i = particle type (e, h, mip).

$E_{vis,i}$ = visible energy in the active layers for i.

$E_{invis,i}$ = invisible energy in the active and passive layers for i.

$E_{abs,i}$ = totally absorbed energy in the calorimeter for i.

Sampling fractions are often normalized to the sampling fraction of a hypothetical particle called a *minimum ionizing particle* or *mip*. R_{mip} (also written just *mip*) is defined as:

$$mip = \frac{(dE/dx)_s}{(dE/dx)_s + R(dE/dx)_t}$$

where $(dE/dx)_s$ and $(dE/dx)_t$ are the minimum ionizing losses per unit length of the active medium and the absorber, and $R = t/s$, where t and s are the thicknesses of an absorber plate and an active layer respectively. Muons at energies around 200 – 300 MeV behave similarly to and are often used as mips. One expresses sampling fractions as ratios to the mip value as R_i/R_{mip} or i/mip. For example, typical electron/mip ratios for heavy absorbers and light readout are between 0.6 and 0.7.

One expects fluctuations in the energy measurement due to the sampling structure of a sampling calorimeter as well as from the statistical nature of the physical processes occurring during a shower. Fluctuations in the sampling fractions (denoted Δi for particle type i) influence the overall energy resolution. They can be reduced by increasing the sampling frequency [11].

2.1.2 Electromagnetic Showers

High energy particles, upon penetration of the material of a calorimeter, deposit their energy by initiating "showers" of lower energy particles produced through various types of interactions. One generally distinguishes between two kinds of showers: *electromagnetic* (em), which only involve purely electromagnetic processes and *hadronic*,

which produce particles through nuclear interactions (though they also have an electromagnetic component due to pions, η's etc, that decay to γ's (photons)).

An electromagnetic shower is initiated when a high energy electron, positron or photon interacts with matter. The main energy loss mechanisms that come into play are governed by quantum electrodynamics (and involve only $e^{\pm}$s and γs as shower components) and are well understood:

- Ionization losses: The showering $e^{\pm}$ ionizes electrons from atoms of the absorber.
- Pair production: Photons with at least the threshold energy ($2m_e$) transform into e^+e^- pairs in the presence of a third body (usually an absorber nucleus) to conserve momentum.
- Compton scattering: The photon scatters off of an atomic electron.
- Photoelectric effect: The photon energy is completely absorbed by an atomic electron allowing it to escape from the atom.
- Bremsstrahlung: The charged e^+ or e^- interacts with the Coulomb field of an absorber nucleus, emitting a photon.

Initially, when the average shower particle energy is high, bremsstrahlung and pair production processes dominate the energy loss. Later, at energies below the *critical energy* (ϵ_0), defined as the energy at which energy loss due to bremsstrahlung and ionization are equal, ionization and the photoelectric effect become the dominant processes (for the charged particles and photons respectively) and eventually the shower stops when the average shower particle energy falls to a level where no new particles can be created.

Electromagnetic showers are usually characterized by the following two quantities: the *radiation length* (X_0) and the *Molière radius* (ρ_M). The radiation length is defined as the distance over which a high energy electron loses on average the fraction $1-1/e$ of its energy to bremsstrahlung. It is also approximately equal to 7/9 times the average distance a high energy photon travels before converting to a e^+e^- pair. The

Material	Z	$A[g]$	$\rho[g/cm^3]$	$X_0[g/cm^2]$	$X_0[cm]$	$\rho_M[cm]$	$\lambda[g/cm^2]$	$\lambda[cm]$
Polystyrene	$\simeq 3.4$	-	1.060	43.8	41.3	14.7	82.0	77.4
Al	13	26.98	2.70	24.01	8.89	5.38	106.4	39/4
Fe	26	55.85	7.87	13.84	1.76	1.91	131.9	16.8
Pb	82	207.19	11.35	6.37	0.56	1.56	194.0	17.1
U	92	238.03	18.95	6.00	0.32	0.96	199.0	10.5

Table 2.1: Values of radiation lengths X_0, Molière radii ρ_M, and interaction lengths λ, for some selected materials.

Molière radius is defined as the ratio of X_0 to the critical energy. The following relations approximately hold:

$$X_0 \approx 180A/Z^2 \ (g/cm^2)$$

and

$$\rho_M \approx 7A/Z \ (g/cm^2)$$

where A = atomic mass number of absorbing material

M = atomic number of absorbing material

The numerical value of X_0 and ρ_M for some materials (including those of the ZEUS calorimeter) are shown in table 2.1 [21].

These quantities parametrize the shower development in an approximately material independent way, X_0 being a characteristic of the longitudinal development, ρ_M, the transverse. Because all the processes that make up electromagnetic showers are well known, precise computer simulations (for example the Monte Carlo code EGS4 [16]) as well as approximate analytic descriptions of electromagnetic showers are possible.

Energy Resolution

For electromagnetic showers in sampling calorimeters, the visible energy is given by

$$E_{vis} = e \cdot E \ ,$$

where e $(= R_e)$ is the electromagnetic sampling fraction.

The electromagnetic energy resolution of a sampling calorimeter can be expressed as:

$$\frac{\Delta E_{vis}}{E_{vis}} = \frac{\Delta e}{e} = \frac{a}{\sqrt{E}},$$

where E is in GeV and ΔE_{vis} are the fluctuations in E_{vis} and Δe are the fluctuations in electromagnetic sampling fraction.

Experimentally, it is found that the parameter a is independent of energy and is approximately proportional to $\sqrt{t}$, where t is the absorber plate thickness. Other effects such as photostatistics and light attenuation in the scintillator degrade the energy resolution but it is the sampling fluctuations which usually dominate. The electromagnetic energy resolution of the ZEUS calorimeter is [33] $18\%/\sqrt{E} \oplus 1\%$.

2.1.3 Hadron Showers

Hadron showers consist of series of successive hadronic interactions initiated by a strongly interacting particle (such as protons, neutrons, pions, etc).

The composition of hadron showers is much more complex than electromagnetic showers. No simple analytic description exists for hadron showers and computer simulation packages, although detailed and complex, still only approximate real shower behaviour. One key feature of hadron showers is that a fraction of the incident particle energy is "invisible" i.e. it is lost in processes that produce no measurable signal in the calorimeter. Also there is a significant electromagnetic component in hadron showers (from neutral pions, η's that decay to photons) which fluctuates strongly from event to event. This electromagnetic fraction (f_{em}) is energy dependent and non-Gaussian.

Before initiating a hadronic shower, a charged hadron will (with high probability) first lose energy by ionization of the calorimeter material. For energies above 50 MeV, the hadronic interaction of the incoming hadron with the nucleons of the absorber material will induce a spallation process. This consists of many independent particle collisions inside absorber nuclei, followed by a de-excitation through p, n, $\pi^{\pm}$,π^0, γ,

...emission and evaporation. This intranuclear cascade will cause new particles to be emitted if their kinetic energy is above the binding energy. Also fission of heavy nuclei can be induced by high energy ($\gtrsim 50\ MeV$) pions, protons and neutrons. The production of nuclear fragments and excited nuclei results in lost nuclear binding energy in the absorber that is unmeasurable. Additionally, de-excitation may proceed via γ-emission. Although most γ's are prompt, neutron capture of U^{238} leads to delayed γ-radiation up to 1 μs. Neutrinos leave the calorimeter undetected and muons behave like mips and may escape the detector after depositing a certain fraction (a few GeV) of their energy.

The equivalent parameter to the radiation length for electromagnetic showers, which describes the hadron shower development in a material independent way is the nuclear interaction length λ. It is defined by:

$$\lambda = \frac{A}{N_A \cdot \sigma_i}$$

in (g/cm^2), where A = the mass number of the absorber, N_A = Avogadro's number and σ_i = inelastic cross section. A good approximation is given by:

$$\lambda \simeq 35 \frac{A^{1/3}}{\rho}$$

in (cm), where ρ = the specific density in (g/cm^3). Refer to table 2.1 for some typical values. One notices immediately that λ is much larger than X_0 for a given material, requiring larger calorimeters to fully contain hadron showers. For example, 300 GeV pions are contained to 95% in about 80 cm of uranium, whereas for 300 GeV electrons, a depth of 10 cm is sufficient. The depths of the ZEUS calorimeter in terms of λ are 7.1 λ for FCAL, 5.3 λ for BCAL and 3.1 λ for RCAL. Typical transverse dimensions of highly energetic hadron showers is about 0.1 to 0.3 λ. 95% radial containment of a hadron shower is achieved in a cylinder of radius $R \lesssim \lambda$, however R does not really scale with λ and decreases with high Z materials.

Energy Resolution and Compensation

The energy resolution of hadron sampling calorimeters is significantly worse than that of electromagnetic calorimeters. This is due to the different physical processes which contribute to the shower development, giving different measurable signals for the same amount of deposited energy. In addition, the relative fractions of these different contributions fluctuate from event to event.

Most important, the non-Gaussian fluctuations of f_{em} degrade the hadronic resolution if the response of the calorimeter to electromagnetic and hadronic signals are not equal (i.e. $e/h \neq 1$). Also the energy dependence of f_{em} cause e/h to be energy dependent as well, resulting in a nonlinearity in the calorimeter signal (i.e. the measured energy of an electron would be different from that of a jet with the same total energy).

Loss of nuclear binding energy (E_{bind}) also strongly influences the energy resolution of hadron calorimeters, for example, 10 GeV $\pi^{\pm}$'s spend about 20 % of their energy overcoming E_{bind}. However, the nuclear breakup produces neutrons in numbers that are $\sim E_{bind}$. Hence if one can detect the breakup neutrons, it should be possible to compensate for the E_{bind} loss.

Ignoring detector imperfections, the resolution of a hadronic calorimeter can be written in general as

$$\frac{E\sigma_{had}}{E} = \frac{A\sqrt{t_{abs}}}{\sqrt{E}} + C$$

where t_{abs} is the absorber layer thickness, $A = \sqrt{\sigma^2_{intr} + \sigma^2_{samp}}$ is the contribution from intrinsic fluctuations, nuclear binding losses and sampling fluctuations and C depends on the degree of compensation of the calorimeter and vanishes when $e/h = 1$.

In order to achieve compensation (and thus eliminate the C term, which dominates the resolution at high energies) we must compensate for the energy lost in breaking up the nuclei. This is done in the ZEUS calorimeter by using an active layer material with a high hydrogen content (plastic scintillator) in order to moderate the neutrons produced in the nuclear breakup of the (high Z) passive layers. The recoil protons

produce visible light in the scintillator by ionization and hence produce a measurable signal that is correlated with the binding energy losses. The most important parameter to achieve compensation turns out to be the ratio of absorber plate thickness to active layer thickness ($R_d = t_{abs}/t_{act}$). From Monte Carlo simulations and prototype tests it was found that a uranium scintillator calorimeter with $R_d = t_U/t_{scint}$ of about 1.3 would be compensating [11].

The hadron energy resolution of the ZEUS calorimeter, including all known instrumental imperfections such as nonuniformities, leakage etc, is [33]

$$\frac{\sigma_{had}}{E} = \frac{35\%}{\sqrt{E}} \oplus 2\% \, (GeV) \, .$$

2.2 The ZEUS Calorimeter

After an extensive test program with prototype calorimeters and detailed Monte Carlo studies, the design of the ZEUS calorimeter was finalized. The basic structure of the calorimeter consists of modules made up of stacks of depleted uranium (DU) plates sandwiched between scintillator tiles called towers. The DU plates are 3.3 mm thick corresponding to 1 X_0 and are wrapped in steel foil for handling safety and also to reduce the noise from the radioactivity of the uranium. The scintillator tiles are 2.6 mm thick. As discussed in the previous section, the choice of scintillator and depleted uranium with the above thicknesses allows for a compensating calorimeter, which leads to optimal hadron energy resolution [33].

The calorimeter is mechanically divided into three components: the Forward Calorimeter (FCAL), the Barrel Calorimeter (BCAL) and the Rear Calorimeter (RCAL). Although there are differences between the 3 calorimeter components, they share a basic common structure. They are longitudinally separated into an inner electromagnetic section (EMC) and an outer hadronic section (HAC). The EMC section has a depth of $\sim 25 X_0$ (which is roughly ~ 1 interaction length (λ)). The outer HAC section depth varies from $\sim 6\lambda$ to $\sim 3\lambda$ going from forward to rear. The FHAC and BHAC sections are further subdivided into two sections (HAC1 and HAC2). Typical

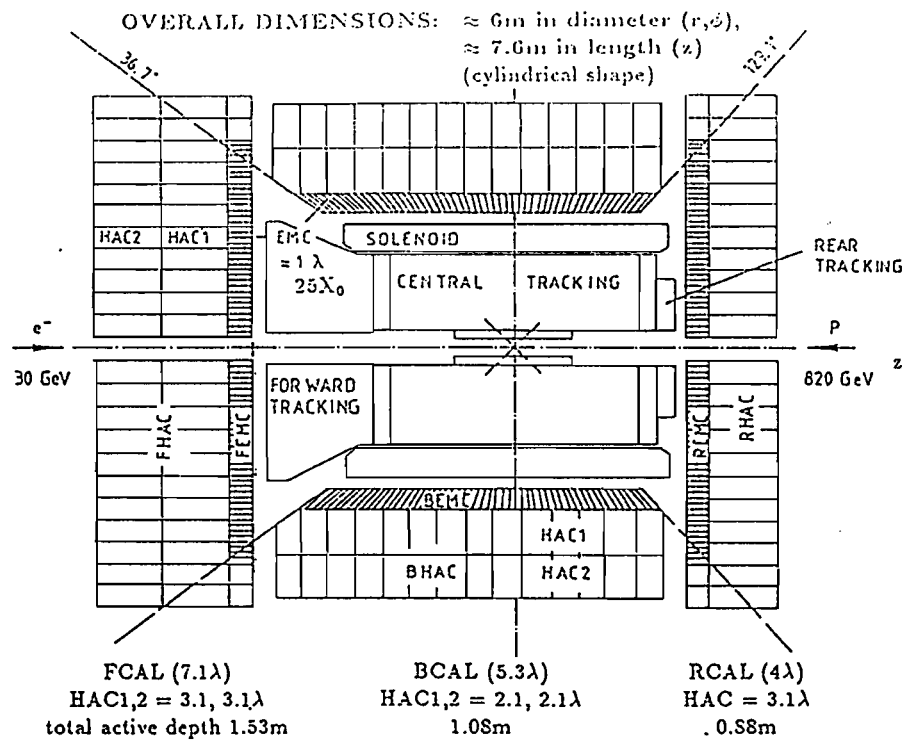

Figure 2.1: Layout of the ZEUS Uranium Scintillator Calorimeter

tower sizes are 5 $cm \times 20\ cm$ (EMC) and 20 $cm \times 20\ cm$ (HAC). FCAL covers the polar angles from $\theta = 2.2°$ to $\theta = 39.9°$, BCAL covers $\theta = 36.7°$ to $\theta = 129.1°$, and finally RCAL covers the region $\theta = 128.1°$ to $\theta = 176.5°$. The entire calorimeter provides solid angle coverage of 99.8% in the forward hemisphere and 99.5% in the rear. Figure 2.1 summarizes the geometry of the calorimeter.

2.2.1 Calorimeter Modules

The F/RCAL modules share a non-projective tower structure, differing mainly in the fact that the RCAL has only one HAC section as well as having a coarser EMC tower structure. The size of the HAC(0,1,2) towers in both FCAL and RCAL is 20 $cm\times$ 20 cm. The FEMC tower size is 5 $cm\times$ 20 cm whereas for the REMC sections the tower size is 10 $cm\times$ 20 cm. The FCAL and RCAL are both made up of 24 modules each. An FCAL module is shown in figure 2.2 [34].

The barrel calorimeter (BCAL) is made up of 32 identical modules, each covering

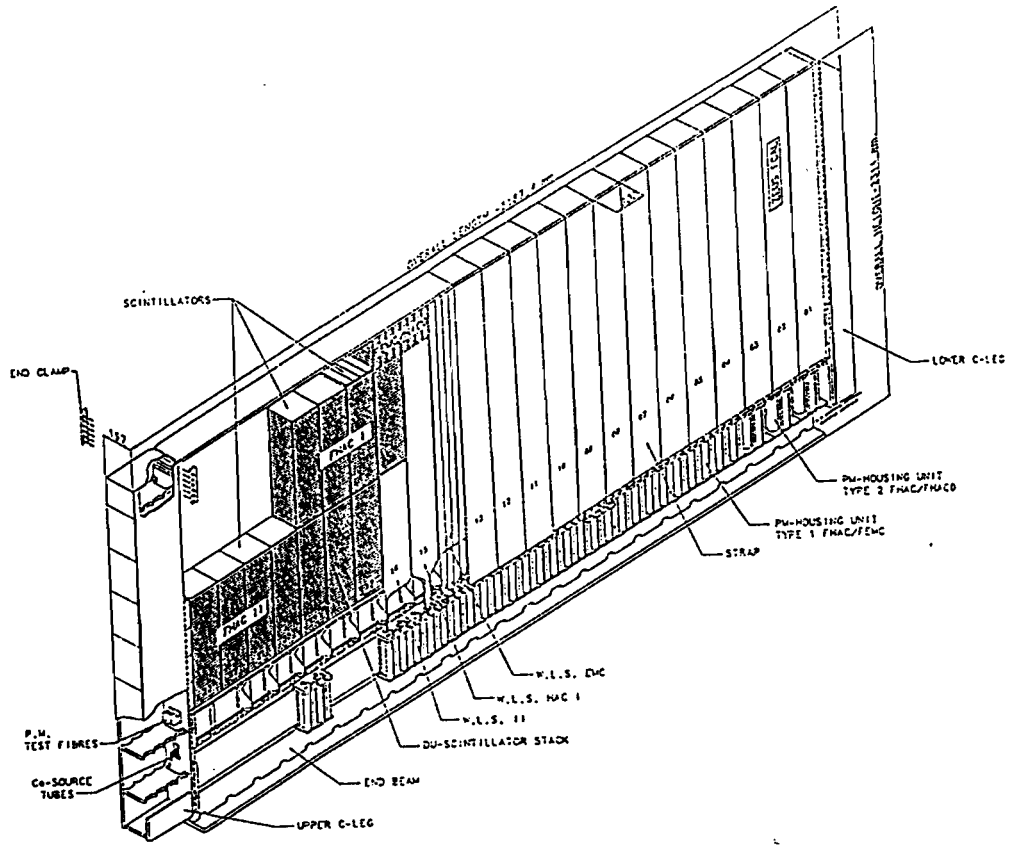

Figure 2.2: Internal Structure of a large FCAL module.

an angle of 11.25°. The modules are projective in ϕ but are tilted by 2.5° in order to avoid projective module boundaries (where passage of a particle would be poorly measured). A schematic of a BCAL module is shown in figure 2.3.

2.2.2 Optical Readout System

The optical readout of the scintillator tiles in the calorimeter is done by means of wavelength shifters and light guides. Each subtower is read out on opposite sides. When a signal is produced in the scintillator, the light from that signal crosses a small air gap to the wavelength shifter. This signal causes fluorescence in the dye of the WLS. The dye re-emits light isotropically at a longer wavelength. This re-emitted light is propagated by total internal reflection to a light guide and ultimately into a photomultiplier tube (PMT). A schematic view of the optical readout system for an F/RCAL type module tower is shown in figure 2.4 [33].

The requirements set for the optical system were as follows:

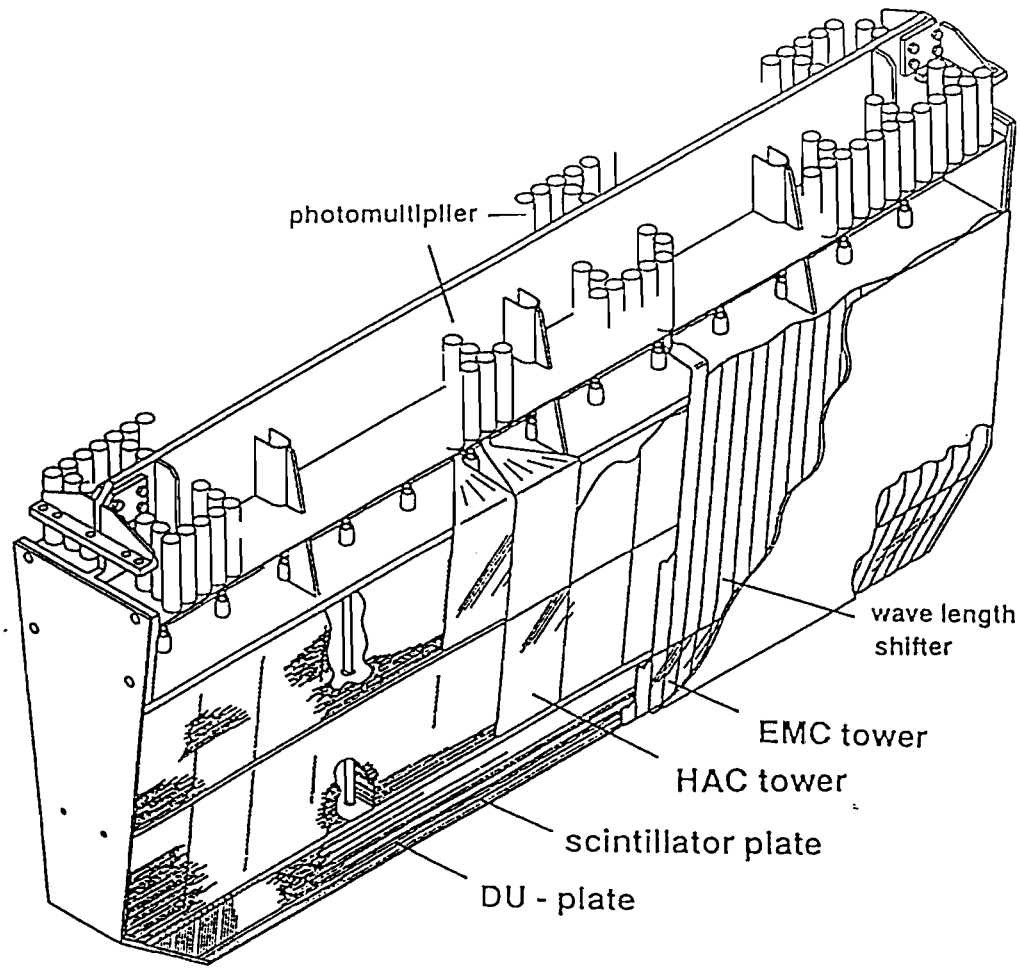

Figure 2.3: Internal Structure of a BCAL module.

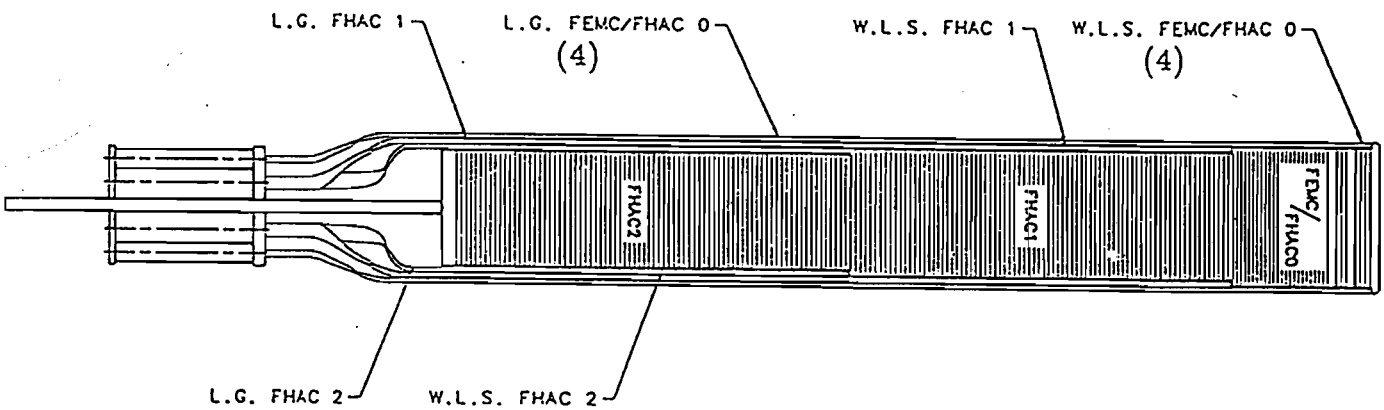

Figure 2.4: Details of optical readout system.

- Passage of a *mip* must generate at least 2 photoelectrons per photomultiplier tube per scintillator layer. This is necessary to keep the photostatistics contribution to the energy resolution small.

- The transverse optical response in the scintillator as well as the longitudinal response in the WLS must be uniform to minimize the systematic error on the energy resolution and the UNO[2] calibration. The design goal for both the SCI and WLS uniformity was $(4 \pm 2)\%$.

Scintillator

The scintillator tiles were manufactured by Kuraray Co., Ltd. of Tokyo, Japan. The material used is SCSN-38. It has a cross-linked polystyrene base doped with 2 wavelength shifting dyes. As with most aromatic cast scintillators, SCSN-38 has superior stability against aging and radiation damage. It also has a high light yield.

Wavelength Shifter

The wavelength shifters and light guides are made from 2 mm sheets of PMMA (Polymethyl methacrylate) doped with the fluorescent dye Y-7 and an ultra-violet absorbent cutting off wavelengths less than $360nm$ in order to reduce the contribution from Cerenkov light produced by showers occuring in the intermodule cracks. These were also manufactured by Kuraray. For the F/RCAL EMC and HAC0 towers, the concentration of Y-7 was 45 ppm, whereas for all others a concentration of 30 ppm was used. The wavelength shifters and light guides were made from single plates so as to avoid glue joints.

Uniformity

For F/RCAL, strict quality control and monitoring was applied during the manufacture of the scintillator tiles and WLS. Any given calorimeter cell (subtower) uses

[2]Uranium NOise: The signal produced by the decays in the depleted uranium plates is very stable and can be used for calibration purposes. This is discussed further.

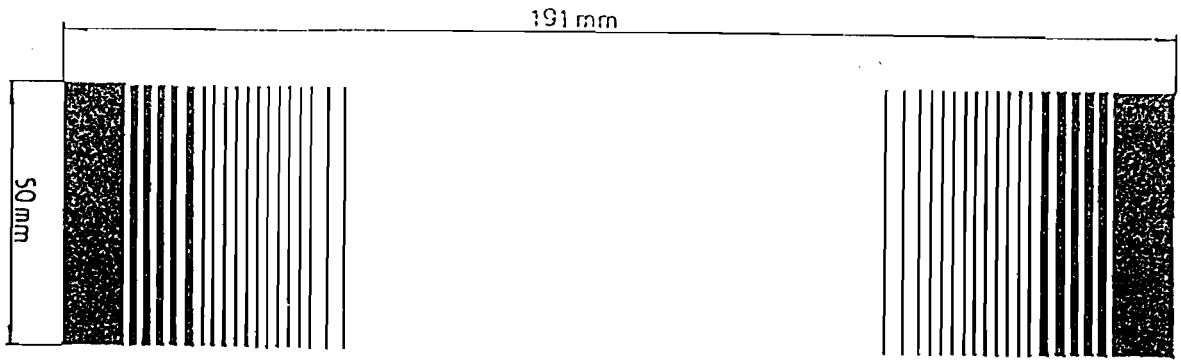

Figure 2.5: Correction pattern for an EMC scintillator tile

tiles from the same production lot. The tiles were wrapped in Tyvek paper printed with a correction pattern in order to improve uniformity as well as to protect against mechanical damage (see figure 2.5). For the WLS, back reflectors with a black dot pattern further improves uniformity. The Y-7 concentration in the WLS is a balance of conflicting constraints: for good uniformity, one requires a low concentration, but for high light yield, a higher concentration is desirable.

Because the BCAL modules' projective geometry requires many (82112) scintillator tiles, of many different sizes (22 different EMC tile types and 300 different HAC tile types), it was decided to use a laser cutting technique. This yielded a slightly worse response compared to that obtained with traditional hand cutting and polishing ($\simeq$ 2% light loss) but was judged acceptable. As with the F/RCAL modules, uniformity is improved in the WLS for BCAL modules by making use of a backing pattern.

2.2.3 Photomultipliers

Photomultiplier tubes (PMTs) are electron tube devices which convert light into a measurable electric current (or charge). They are extremely sensitive and are ideally suited for reading out the light produced in scintillating detectors. The basic components of a PMT consist of a cathode made of a photosensitive material, followed

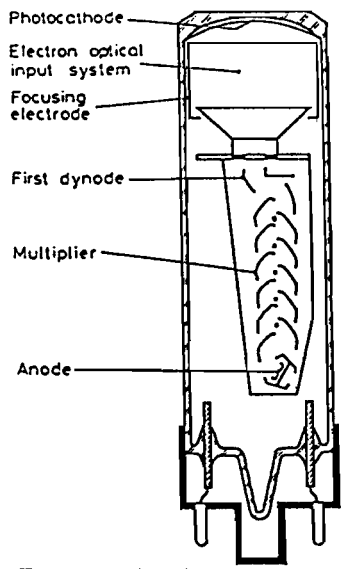

Figure 2.6: Principal components of a photomultiplier tube.

by an electron collection system, an electron multiplier section (also called dynode string) and finally an anode from which the final signal is measured (see figure 2.6). During operation, a high voltage is applied to the cathode, dynodes and anode such that a potential "ladder" is set up. When an incident photon strikes the photocathode, an electron is emitted via the photoelectric effect. This photoelectron is then directed and accelerated toward the first dynode. This causes secondary electrons to be emitted, which are in turn accelerated to the next dynode, etc. Thus an electron cascade down the dynode string is created. At the anode, the cascade is collected resulting in a current (or charge pulse) which can be measured. If the cathode and dynode systems are linear, the current at the output is directly proportional to the number of incident photons.

The basic operating parameter of a PMT is its gain G. It depends in general on the high voltage supplied to the multiplier stages, the number of dynodes, the quantum efficiencies of the photocathode and the dynodes. The main sources of fluctuations in the gain of a PMT are the fluctuations in the number of photoelectrons produced at the photocathode and to a lesser extent, fluctuations in the multiplier stages. Other possible factors include external magnetic fields, temperature and the presence of radioative materials which can cause "dark" currents (i.e. signal when no light signal

is present) [13],[18].

The requirements on the PMTs for the ZEUS calorimeter are a good gain stability, high linearity and a small dark current. On the basis of extensive prototype testing, Hamamatsu R580-12 tubes were chosen for the BCAL, RCAL and the HAC sections of the FCAL and Valvo XP1911/01 tubes for the EMC section of FCAL. There are 11836 PMTs reading out the signals from the calorimeter.

PMT Bases

Normally PMT use resistive voltage divider bases to provide the high voltages to the different stages of the multiplier section. For the ZEUS experiment, it was decided to use Cockcroft-Walton (CW) generators in the PMT bases. The CW generator is driven by a 180 kHz oscillator to produce the desired voltages internally across a chain of diodes. The advantages of the CW bases are:

- small power consumption, typically an order of magnitude lower than resistive bases, producing less heat; and
- low external operating voltage (24 V), thus improving safety.

The main difficulties of this design include the quantized voltage steps and the suppression of switching noise [33].

2.2.4 Readout Electronics

Relating the pulses produced in the PMTs to meaningful physical quantities is the main task of the electronic readout. It also has to deal with the very high rate of events produced during $e - p$ collisions.

The different functions of the electronic readout of the ZEUS calorimeter can be summarized as follows [4]:

- Shaping and amplification of the signals from the PMTs.

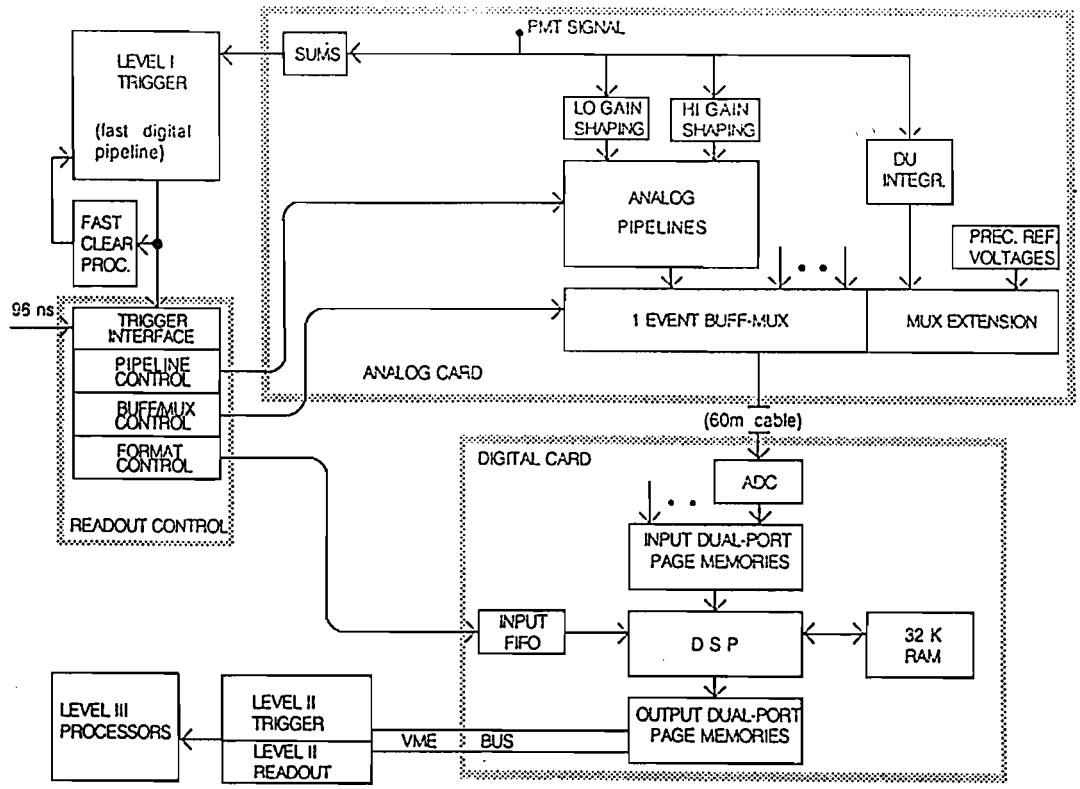

Figure 2.7: Overview of the ZEUS calorimeter readout scheme.

- Sampling of shaped signals at the HERA bunch crossing rate ($\approx 10\,MHz$). The samples are then stored in a $5\mu s$ deep, 10 MHz pipeline.
- Buffering of triggered events.
- Digitization of selected pulse samples.
- Computation of pedestal and gain corrections online.
- Reconstruction of the charge and time of the event.

Readout Scheme

A schematic overview of the readout is shown in figure 2.7. The readout divides naturally into two groups: the "analog cards", which are mounted onto the calorimeter (behind the PMTs) and the "digital cards", which are located in VME crates[3] away

[3]The VME bus is a digital data transfer system in wide use in high energy physics.

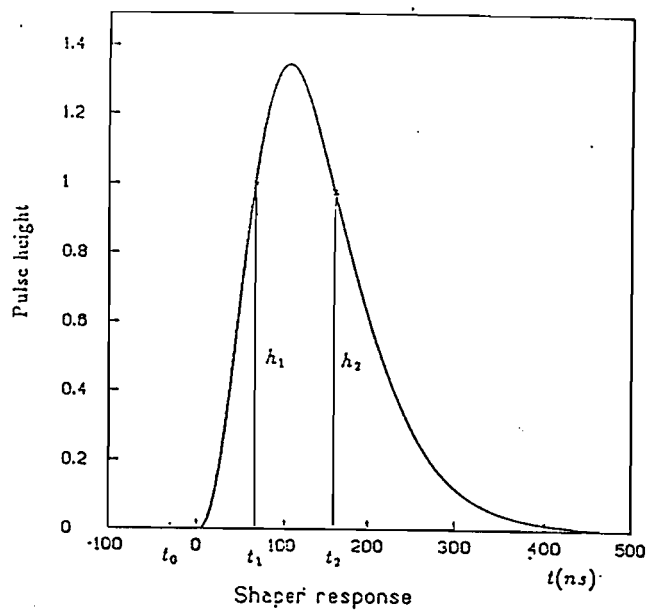

Figure 2.8: Shaper response to impulse input. The nominal sampling points are indicated.

from the detector. The entire calorimeter readout is controlled by a single set of modules called the "readout control" using specially designed "transputers".

Analog Cards

12 PMT signals are read in by an analog card and are each split resistively five ways: to a trigger sum (for the calorimeter first level trigger); to the high and low gain shapers; to the DU current measuring circuit (which integrates the signal for 20 ms) and to the input termination.

The analog cards each integrate and shape signals from the PMTs on separate high and low gain channels in order to achieve the required dynamic range. The high and low gain ranges for the three main calorimeters differ due to the asymmetric collider geometry (which cause the maximum energy deposition to have a strong angular dependence). The (high gain; low gain) ranges for FCAL, BCAL and RCAL respectively are as follows: $(0 \rightarrow 18GeV; 0 \rightarrow 400GeV)$, $(0 \rightarrow 14GeV; 0 \rightarrow 314GeV)$, $(0 \rightarrow 12\,GeV; 0 \rightarrow 60\,GeV)$.

The shaping circuit must be able to suppress high and low frequency noise, as

well as restore the baseline rapidly in order to preserve the dynamic range. The circuit chosen for ZEUS, uses high precision resistors and capacitors (with tolerances of 0.5 % and 1 % respectively), has a response to a delta-function impulse which is approximately triangular with rising and falling times somewhat larger than the sampling rate (shown in figure 2.8). The pulse height (charge) is derived from a weighted sum of the samples before and after the peak and the time measurement is provided by a scaled difference (or ratio) of these same samples (see below for more details of the reconstruction algorithms). The cards sample the shaped signals every 96 ns and delay the samples in analog pipelines. When triggered, individual cards store up to eight samples in an analog buffers which are then multiplexed to the digital cards. The charge scale for the PMT signals is 1.3 pC for 300 MeV of deposited energy in the FCAL, and 1.7 pC per 300 GeV for the BCAL and RCAL. The analog pipeline is based on a switched capacitor design which was chosen over other technologies based on its radiation hardness as well as considerations of cost and power consumption. Each pipeline chip has 58 cells, giving a storing time of 5.6 μs. Also located on the analog cards is the buffer/multiplexer chip. The buffer is needed to avoid long deadtime due to pipelines being read while samples are digitized.

Digital Cards

Traveling over 60 m of cable, signals from the PMTs are sent from the analog cards to the digitizing electronics. The digital cards reside in VME crates. Four Datel ADS-112 12-bit ADCs digitize the signals, multiplexed from the analog cards every 1.7 μs. The digitized values are placed in the four 2k $\times$ 12-bit RAM buffers.

The digital cards have on-board digital signal processors (DSPs) which perform calculations based on the information from the samples and from special calibration constants related to the analog card electronics obtained in calorimeter calibration runs. The DSPs perform the reconstruction of the deposited energy, time and other shower information as well as format the output data for the higher level trigger processing, which would not be possible to do online in a conventional centralized

computing environment. In addition the DSPs are used in the calibration runs.

Transputers

Another important element of the readout system is the transputer based readout control [24]. Transputers are microprocessors with large connectivity and can be used for parallel processing. VME modules with 2 onboard transputers were specially designed for the ZEUS calorimeter readout. One of the transputers is designated for (second level) trigger processing and the other is for readout. They reside on the same VME bus as the digital cards. When data from the DSPs are available, the digital cards signal the readout transputer which reads out a subset of the data. This data is shared with the trigger transputer on the same module which, along with the other trigger transputers, processes this data. When a positive second level trigger decision is received by the readout transputer, it reads out all the data and sends it to the global event builder system which reconstructs complete events from data from all the ZEUS detector components.

Another new use of the transputers involves performing on-line calculations of means and sigmas of the charges and times for arbitrary numbers of identical triggers (such as occurs in calibration runs) [14],[12]. This fact is exploited in the application of the UNO method of calculating the number of photoelectrons described in the next chapter.

Charge and Time Reconstruction Algorithms

As mentioned previously, the DSPs in the digital cards reconstruct the charge and time of events from the samples read out from the analog cards. A brief description of the algorithms used is given here [1].

Raw samples are first corrected for pipeline and buffer cell gains and pedestals[4]. Once this is done, the next step is to reconstruct a pulse amplitude. Referring to

[4]The complete description of how this is done would take us too far afield and can be found fully described in [1].

figure 2.8, the quantity

$$H' = (h_1 - h_{-1}) + R \cdot (h_2 - h_{-1})$$

is computed, the sample h_{-1} is the baseline sample, subtracting it from h_1 and h_2 constitutes the baseline correction. H' depends on the positions of h_1 and h_2 on the pulse. The nominal sampling time $T = 0\ ns$ is defined when $h_1 = h_2$. Variations in the sampling time can occur for several reasons e.g.: PMT transit times, different cable lengths, pipeline differences and background particles not originating from the interaction vertex. The approach adopted is as follows. The quantity R is constant for all channels and all event types and is set to 1.80. It is approximately the ratio of the slopes at h_1 and h_2. To take into account the run type corrections, a polynomial correction is applied.

For each type of event (particles, laser, LED, charge injection) a polynomial of the form:

$$H = H'(1 + \sum_{n=1}^{4} c_n T'^n)$$

where

$$T' = \frac{h_1 - h_2}{H'}$$

is computed. The c_n were determined from test beam results and are fixed for all channels.

Finally, once the time dependence of the sampling has been removed, the conversion from the amplitude H to a charge Q is done by injecting charge at different amplitudes and using a linear relation:

$$Q = a + bH$$

The constant a only appears in reconstructing charge injection events, in order to account for a small offset in the charge injector pulse, it is not used in the reconstruction of any other event types.

The time measurement is obtained from the sampling time T using a polynomial

function as follows:

$$T = \sum_{n=1}^{3} d_n T'^n$$

The constants d_n are obtained from beam data and are fixed for all channels. From this quantity one subtracts an offset T_{offset} which takes into account the sampling time differences between channels, and also depends on the event type. The corrected channel time is then:

$$t = T - T_{offset}$$

and the overall time of an event is given by an energy weighted channel time sum.

2.3 Monitoring and Calibration

There are several redundant tools available to calibrate and monitor the ZEUS calorimeter, they are listed below:

- The cobalt source scanning system.
- The DU current.
- The charge injection system with programmable on/off and amplitude.
- The light flasher system using a laser and light emitting diodes (LEDs).

Cobalt Source Scanning

The cobalt scanning system was used primarily during installation of the calorimeter modules to check for faults in construction by running radioactive cobalt sources down specially designed tubes in the modules or outside the modules and checking the response. Construction flaws would show up as unusual dips or bumps in the spectra obtained and could be corrected before the modules became essentially inaccessible. It is also used to measure the attenuation lengths of the WLS [2].

UNO Calibration

The UNO noise is used to intercalibrate the gain of the entire readout. Since the UNO signal is very stable,[5] one can maintain the relative gain between PMTs by adjusting the high voltage such that the measured UNO signal is equalized amongst the tubes.

Charge Injection System

The charge injection system is used to calibrate the readout electronics, by injecting precise amounts of charge directly into the readout. It is primarily used in calorimeter calibration runs.

2.3.1 The Light Flasher System

The light flasher [15] system of the ZEUS calorimeter injects light from a central laser onto the photocathodes of the PMTs of the calorimeter via optical fibers. The system also has distributed LEDs which can also be used for light flashing. It is used for the following monitoring tasks:

- Measurement of the number of photoelectrons/GeV/PMT and gain of the PMTs.
- Linearity of the PMT readout chain in the energy range 0 to 400 GeV.
- Time delays from the PMTs and electronics. These delays can be measured to within 1 ns and are important in order to precisely reconstruct the charge as well as separate background "beam-gas" events from interesting $e-p$ collisions.
- Short term monitoring of PMT gain variation. This has been done under varying magnetic fields to better than 1% and can also be used to monitor gain under heavy HERA background conditions.

[5]The lifetime of the uranium nuclei being $\sim 4.5 \times 10^9$ years.

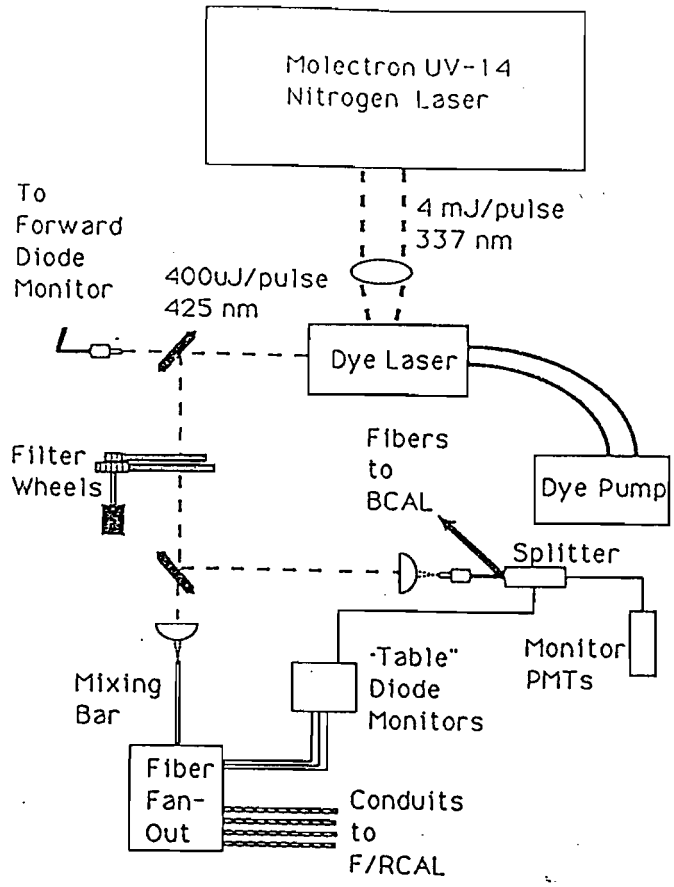

Figure 2.9: First stage of the laser calibration system.

Although the F/RCAL and BCAL share the same laser, the light distribution schemes differ somewhat. The common features will be described first followed by those specific to both systems.

The main elements of the laser system (during the first running period) are:

- a high powered N_2 laser and dye cell (wavelength 425 nm)[6];
- a PIN diode which monitors the laser on a pulse to pulse basis;
- a remotely controlled wheel containing several neutral density filters to attenuate the laser beam;
- a first distribution stage located on the laser table (away from the detector) which splits the beam into fibers which run out to F/R/BCAL;

[6]This laser has been phased out over the course of the first half of 1993, replaced by a more powerful Nd-YAG laser.

- Secondary distribution systems located on the calorimeter which transport the light into each of the 11836 PMTs;

- monitoring systems at various stage of the distribution.

A schematic of the first stage of the laser system is shown in fig 2.9. The N_2 laser was a Molectron UV-14 laser, it required a gas supply and vacuum pump to operate (the YQL-102 Nd-YAG laser which has replaced the Molectron is based on solid state technology and is thus simpler to operate, in addition to delivering pulses about 4 times more powerful [10]). The beam from the primary laser (N_2 or Nd-YAG) enters an optical enclosure where it is focused into a dye laser cell (built at Freiburg University) which is the source of laser light to the calorimeter. The dye chosen is trademarked as *Exciton LD 425*, which emits at 425 nm (blue light). The power output of the dye laser was measured to be about 400 μJ. This dye was chosen because it corresponds to the peak in the spectrum of scintillation light emitted by the SCSN-38 scintillator and is well within the absorption band of the Y7 wavelength shifter.

The primary beam from the dye cell is split by a mirror and 0.1% is measured by a PIN diode (called the forward diode monitor or FDM). The beam then passes through the remotely controlled "filter wheels". There are two discrete filter wheels which allow for combined settings ranging from 0.1% to 100% transmission. In addition a third, continuous filter wheel can be used for intensity scans as it rotates slowly while the laser flashes. Beyond the filter wheels, the beam is split again with partially reflecting mirrors between F/RCAL and BCAL systems where it is then transported into the calorimeter by optical fibers.

The main difference between the F/RCAL and BCAL systems is that the light for F/RCAL is distributed at the laser table, whereas for BCAL, only three fibers run out to the calorimeter where they are fed into the optical splitters that serve all the BCAL modules.

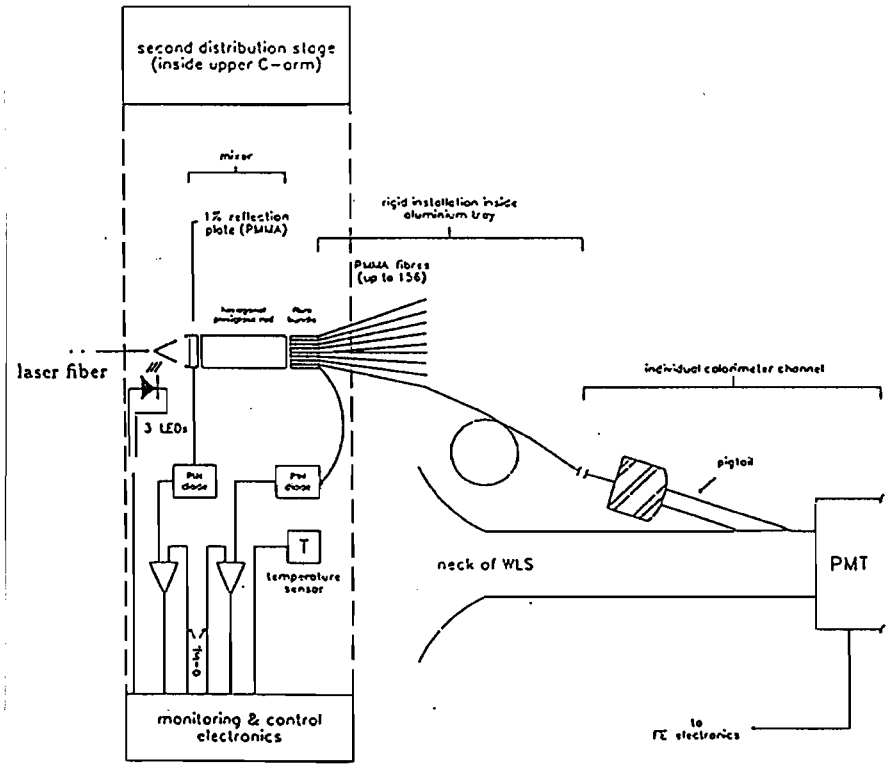

Figure 2.10: F/RCAL second distribution stage.

F/RCAL Light Distribution

A schematic of the F/RCAL second distribution stage is shown in fig 2.10. The light sent to F/RCAL passes through a lens which focuses the beam onto the end of a square acrylic "mixing bar". The laser beam reflects off of the sides of the mixing bar by total internal reflection. The result of this is that the intensity profile of the light spot after passing through the bar is much more uniform than the original beam spot. The other end of the mixing bar is connected to a cluster of 90 fused silica fibers. Each of these are connected via screw-on (SMA) connectors to the fibers which run to the calorimeter. Four of these fibers are connected to PIN diodes to allow intensity measurements at the laser table. The signals from these diodes are sent to the calorimeter to be read out by the standard readout. The 90 fibers are run from the laser table through four metal conduits (FCAL/RCAL $\times$ South/North) to the calorimeter where each of the fibers are run through a protective tube to an SMA connectors on the back face of each calorimeter module. Light is then carried

via an extension/delay fiber to the second stage of the distribution system. Incoming light passes through a partially reflecting plate (1%) which illuminates one of the monitor diodes (PD or "phial" diode). The light is then guided by a mixing bar of hexagonal cross section 18 *mm* across onto the head of a fiber bundle containing up to 165 secondary fibers. The fibers have equal length so as to insure equal timing and attenuation. The material chosen was PMMA instead of quartz or silica fibers because of the high radiation levels near the centre of FCAL. PMMA fibers have a worse attenuation length however than the other fiber types. The individual secondary fibers are coupled to the PMTs by an obliquely sliced PMMA rod "pigtail" which is glued onto the light guides near the photocathode. The feedback and phial diode monitor signals are read out by the same electronics as the PMTs.

F/RCAL LED System

In addition to the laser, the F and RCAL have an additional LED system which can provide pulsed or continuous light to the PMTs. The LEDs have very small pulse-to-pulse variations, unlike the laser, which makes them well suited for short-term gain monitoring. The LEDs reside in the distribution boxes of the second distribution stage. The light intensity is selected by a remotely controlled digital to analog converter.

BCAL Light Distribution

At the laser table, after the initial split, the BCAL beam is focused by a short focal length lens onto a holder containing a 1 mm diameter fiber. This fiber is used as a "mixer" to remove spatial variations in the beam spot. This fiber is coupled to four .75 *mm* diameter output fibers. The BCAL light distribution is done in specially manufactured fan-outs located on the calorimeter, so only three fibers are sent from the laser table. Two of these plug directly into the fan-outs, each of which was designed to service half of the BCAL modules, and the third is connected directly to one module which has a damaged light distribution system (thus needing more light

which would be attenuated by the intervening distribution points). As with F/RCAL, a monitoring system exists for the BCAL. It consists of a 1-to-2 fiber splitter (50%-50% intensity splitting) sending light into two WLS transition pieces each of which is attached to a low-gain PMT. The signals from the monitor PMTs are split and sent to a CAMAC ADC/TDC system. The fan-outs are connected to the fibers that feed each BCAL module, for a total of 64 BCAL laser inputs. Each fiber input serves the left or right side of a module. Within each module there is an additional 1-to-111 split. For each side of a module, 81 fibers transport the light to the WLS to which the fibers are coupled, feeding the light into the PMTs. The reason different laser distribution systems exist for F/RCAL and BCAL is because they were each developed separately before the final assembly of the entire calorimeter at DESY.

Chapter 3

Photoelectron Calculations

The main reason for calculating the number of photoelectrons per GeV for the PMTs of the ZEUS calorimeter is that it is essentially a measurement as well as a monitor of the gain of the PMT. Although the UNO current can be used to maintain the overall gain of the entire readout chain (essentially by adjusting the high voltage of the PMTs to compensate for any drop in gain), if one wants to disentangle changes due to the optical readout, the electronics or PMT aging, one needs a measure of the gain of each component. The number of photoelectrons is also a measure of the quality of the calorimeter's light yield. It is important that the light yield be high enough such that it does not impair the energy resolution of the calorimeter as there is a component of the resolution which improves with the number of photoelectrons.

Several methods are used to determine this quantity. Among these, two will be discussed in this chapter, the method using the laser data taken from the cosmic muon test stand in Hall II at DESY (hereafter referred to as the "Hall 2 method") and a new method which uses the UNO signal ("UNO method"). Other methods not discussed in this thesis include the LED method which uses light from the LED system instead of the laser to extract the number of photoelectrons [22] and a method based on the left-right asymmetry of the pairs of PMTs that form a channel. This last method was primarily used during the initial beam tests of the prototype calorimeter modules [34].

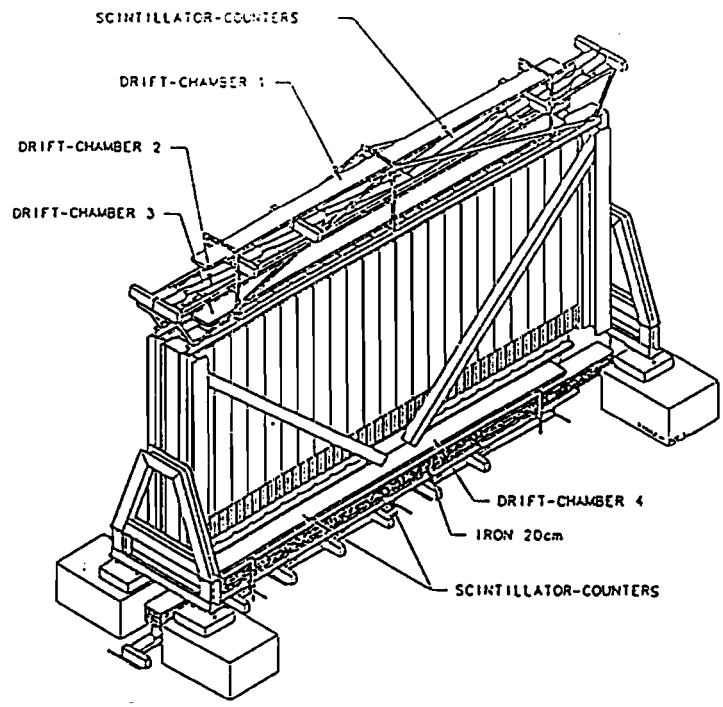

Figure 3.1: Setup of the cosmic ray test stand in DESY hall II.

3.1 Hall 2 Method

3.1.1 Background

From September 1990 to April 1991, 20 FCAL and 20 RCAL modules (from a total of 48) were tested at the cosmic ray test stand at DESY experimental hall II. The main purpose of these tests was to intercalibrate the modules using cosmic rays as well as to compare the calibration to that obtained for some of the modules in test beams (done at CERN for the F/RCAL modules).

The setup is shown in figure 3.1. It consisted of an upper frame with scintillation trigger counters and drift chambers, which could be placed on top of the calorimeter module to be tested. The modules were oriented in "stacking" position, i.e. with the side that would face the interaction (in ZEUS) pointing up. Below the module were placed a 10 *cm* thick iron absorber, a frame with scintillation counters and another drift chamber.

Although the PMT signals were read out with the same electronics that are currently used in the ZEUS experiment, it should be noted that the DSPs in the digital cards were only used to transfer the raw data. Charge and time corrections were

instead calculated offline [7].

The laser used during these tests was a PRA LN103 nitrogen laser pumping a dye cell sending green light ($\lambda = 500\ nm$) pulses to the PMTs. Due to the fairly large pulse to pulse fluctuations of the pulse intensity, monitoring is essential. The data were taken asynchronously (i.e. the laser fired at random with respect to the 96 ns clock used by the readout) so timing corrections are crucial and have to be applied. Laser runs of 500 shots each were taken at a number of different filter settings ranging from 0.1 % to 100 % transmission. Only fixed filter setting data exists as the continuous filter wheel of the current laser setup was not available during the Hall II tests. The raw data was stored on cartridges on the DESY IBM mainframe where standard calibrations as well as charge reconstruction were applied. The reconstructed charges were written out in machine independent ASCII files which were transferred to a workstation (DECstation 3100 running ULTRIX) where the final calculations of the number of photoelectrons per GeV per PMT (n_{pe}) were done [35].

3.1.2 Description of Model

The essential feature of the calculation of n_{pe}'s using laser data is the observation that the number of photoelectrons (N_{pe}) produced at the photocathode of a PMT can to a good approximation be described by a Poisson distribution [18],[35]. The basic model in its simplest form is described here. Suppose the laser provides a series of identical pulses to the PMTs of the calorimeter. Let the mean number of photoelectrons produced at the photocathode of a PMT be N_{pe}. We can look upon the multiplier chain of the PMT as a black box which takes N_{pe} photoelectrons produced at the photocathode and gives out a signal of mean charge Q given by:

$$Q = G \cdot N_{pe}$$

where G is the gain of the PMT. If the only contribution to the spread in the distribution of Q is from fluctuations in N_{pe} at the photocathode (with a corresponding

$\sigma_{N_{pe}}$ given by $\sqrt{N_{pe}}$ from Poisson statistics [1]) then the spread in Q is given by:

$$\sigma_Q = G\sqrt{N_{pe}}$$

Thus one can extract N_{pe} or G from the following ratios:

$$N_{pe} = (Q/\sigma_Q)^2$$

and

$$G = \sigma_Q^2/Q$$

The quantity n_{pe} is related to N_{pe} and G as

$$n_{pe} = \frac{\partial N_{pe}}{\partial E} = \frac{\partial N_{pe}}{\partial Q}\frac{\partial Q}{\partial E} = \frac{Q}{c\sigma_Q^2} = \frac{1}{cG}$$

where c is the conversion factor from charge to energy (pC to GeV) i.e. $\frac{\partial E}{\partial Q}$ determined from test beam calibration of the modules with beams of different particles at known energies.

Of course things are not so simple, the signal width that is measured has several contributions in addition to the photostatistics; the radioactivity from the depleted-uranium (UNO) and electronics noise are responsible for a constant term and the laser has a pulse to pulse jitter which can be fairly large and which scales linearly with Q. We can write an expression for the spread taking into account the above contributions as follows:

$$\begin{aligned}\sigma_Q^2 &= \sigma_1^2 + \sigma_2^2 + \sigma_3^2 \\ &= c_1 + c_2 N_{pe} + c_3 N_{pe}^2\end{aligned}$$

where σ_1 is the term related to UNO and electronics noise, σ_2 is the photostatistics term and σ_3, that due to fluctuations in laser pulse height. In order to extract only the

[1] Recall that for a Poisson distribution given by:

$$P(x) = \frac{m^x}{x!}e^{-m}$$

the mean is given by m and the σ of the distribution is given by $\sqrt{m}$.

photostatistics contribution from the total width, one can remove σ_1^2 by subtracting the pedestal width obtained from a separate pedestal run. The laser fluctuations can be removed by monitoring the laser pulses (with photodiodes or a sum over PMTs).

3.1.3 Data Analysis

We describe here the method used to extract the number of photoelectrons per GeV as applied to a specific module.

Time Corrections

The first step in the n_{pe} calculation is the determination of the timing corrections for the out of time laser shots. The timing of the laser was measured by a photodiode which was hit by the primary laser beam and was read out by a TDC. The normalized charge for each PMT of a module *vs* the laser time as determined by the TDC is histogrammed. By normalized charge, we mean the reconstructed charge from the PMT divided by the pulse height from a photodiode monitor (in order to remove the pulse to pulse fluctuations). The resulting charge *vs* time plot is fit to a quadratic for each PMT and is saved for later use.

Typical plots of these fits are shown in figure 3.2. Also shown are the linear and quadratic terms obtained for a specific module in figure 3.3. One can see the separation between the two systems in this module at channel 132 (the large F/RCAL modules have two secondary light distribution systems whereas for the smaller modules with fewer PMTs there is only one). The quadratic terms are almost all consistent with a single value, due to the high precision components used in the 4 pole filter system in the shaper circuit, however we did not attempt to use a single value for the calculations that followed.

We determine the time corrections with one run and apply them to all the runs used in the n_{pe} calculation for a given module. The choice of which run to use is determined by the need to have high enough light levels (and hence charge) so that accurate measurements are possible (within the dynamic range of the readout)

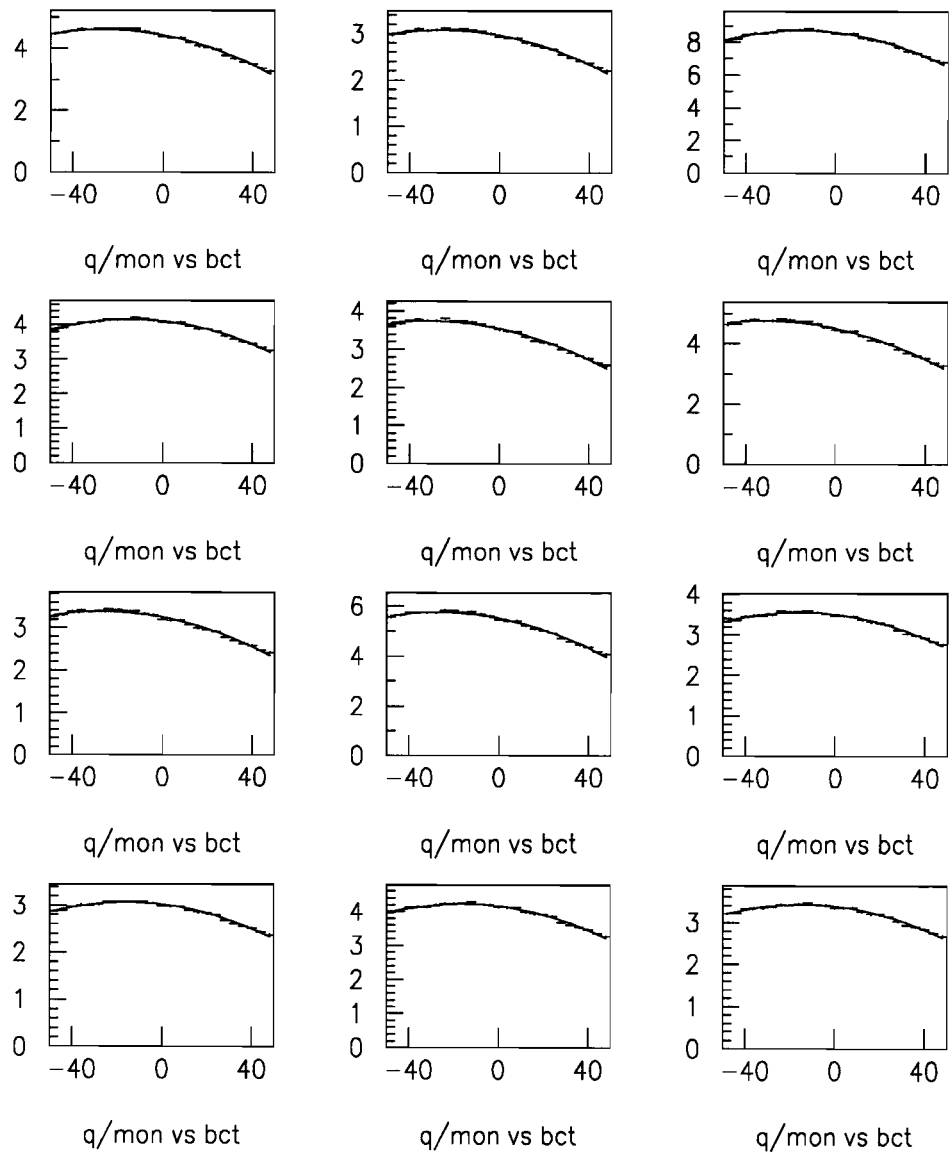

Figure 3.2: Typical normalized charge *vs* TDC time plots. The x axis is in ns. Because of the 96 ns readout period, the events occur within ± 48 ns. The curve which overlays the points is from the fit. These are a mix of EMC and HAC tubes from FCAL module 8.

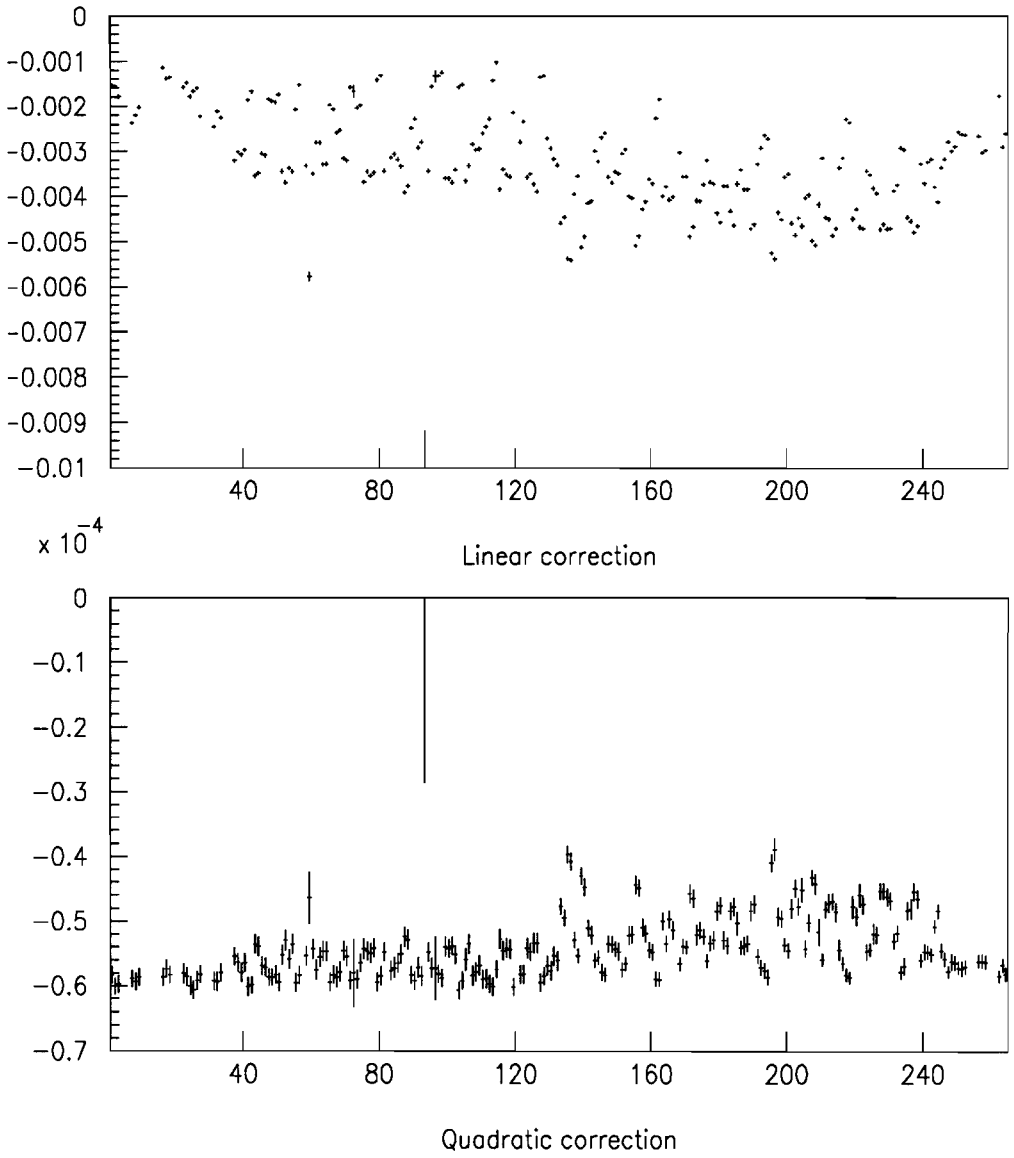

Figure 3.3: Linear and quadratic correction terms for the entire F8 module. Note that one can clearly see the separation between the two fiber distribution systems(which occurs at channel 132 in this module). They have different fiber lengths and thus not surprisingly the timing corrections differ. The channel numbering in these and similar figures is that of the readout at Hall II, which is different from the numbering later used in ZEUS. Also note that with this numbering, the EMC and HAC tubes are mixed in these plots. Unless explicitly stated otherwise, the reader should assume that in similar plots to follow, the numbering will be according to module channel number thus mixing EMC and HAC tubes.

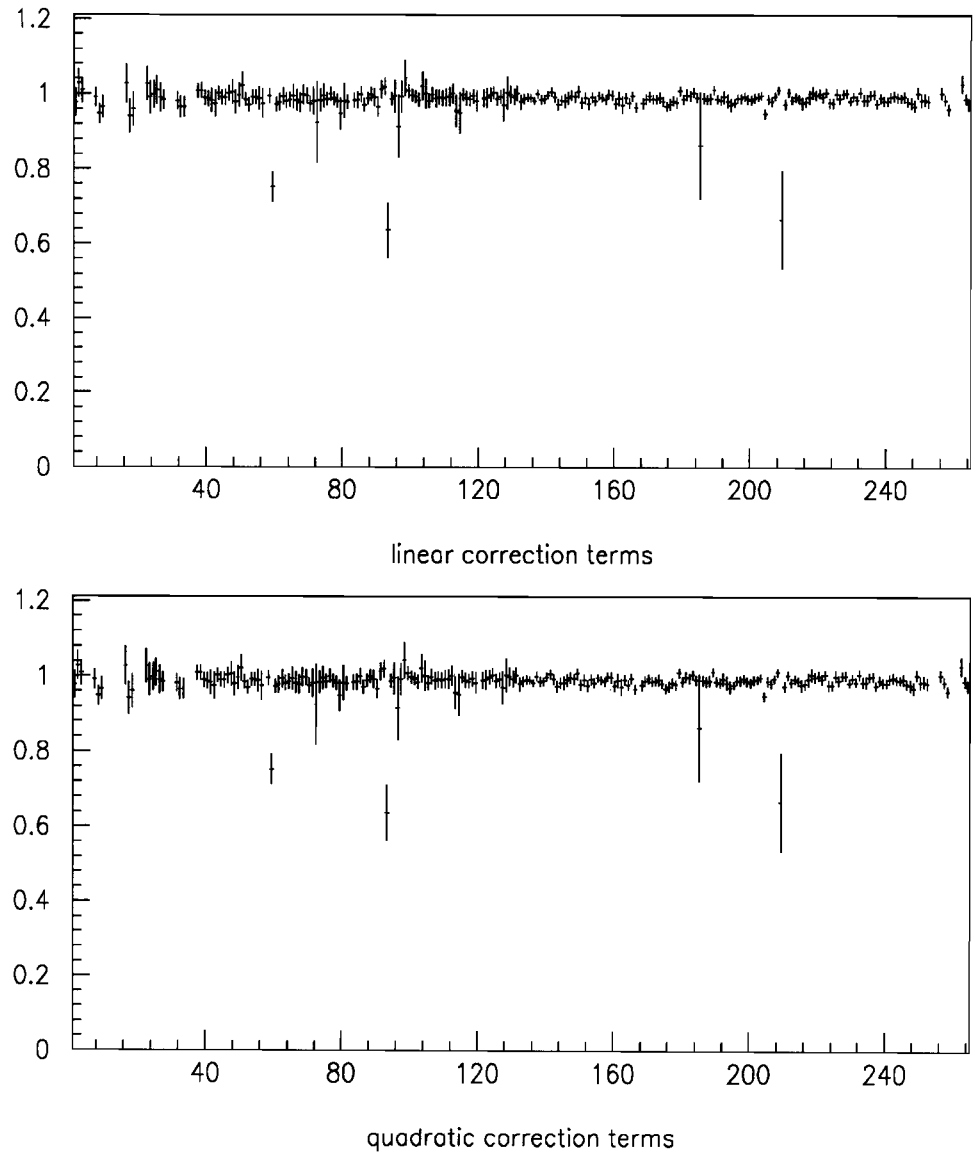

Figure 3.4: Ratio of linear and quadratic terms as obtained from two different filter settings (10% and 4%). These numbers are for Module F8.

without causing saturation in any of the channels (since the laser, unlike the other light flashing tools, can easily produce light levels that saturate the PMTs). Typically runs at filter settings between 4% and 10% were used. The corrections obtained are independent of the run used. This is shown in figure 3.4 where the ratio of the linear and quadratic terms for each tube obtained from a 10% filter setting run and a 4% filter setting is shown. The numbers are consistent within errors apart for a small number of bad tubes.

Monitoring

The charge monitor used for the n_{pe} calculation is a sum over a selection of PMTs. The reasons for this choice deserve some discussion. As is true in the case of the current laser system, there were a number of monitors in the Hall II system. These consist of photodiodes deployed at various stages of the light distribution scheme (many of which are the same as are used in the current laser setup). They are poor monitors for computing photoelectrons as compared to a simple sum over PMTs, however. Although there was a mixing bar in the Hall II laser system, it proved to be too short to be effective. Without uniformity of the laser beam spot, pulse to pulse fluctuations of the laser cause different amounts of light to be sent down the different optical paths with the fractions changing slightly from shot to shot. This happens whenever the light is split, for example at the fanouts located on each module (as well as at the primary fanout of the current laser system where light is divided among FCAL, RCAL and BCAL). Although there are photodiodes monitoring the light at the fanouts on the modules, the light levels used in the n_{pe} method are low enough that the light that reaches the photodiodes is too low to be useful. The photodiodes are mostly used for linearity studies, where high light levels cause the PMTs to saturate and one cannot expect the sum over PMTs to be a good monitor.

To provide an accurate monitor, we choose 25 PMTs (which do not saturate or suffer other problems) from each secondary fanout system to serve as a monitor for that system. The choice of 25 tubes is motivated by the need to minimize the effect of

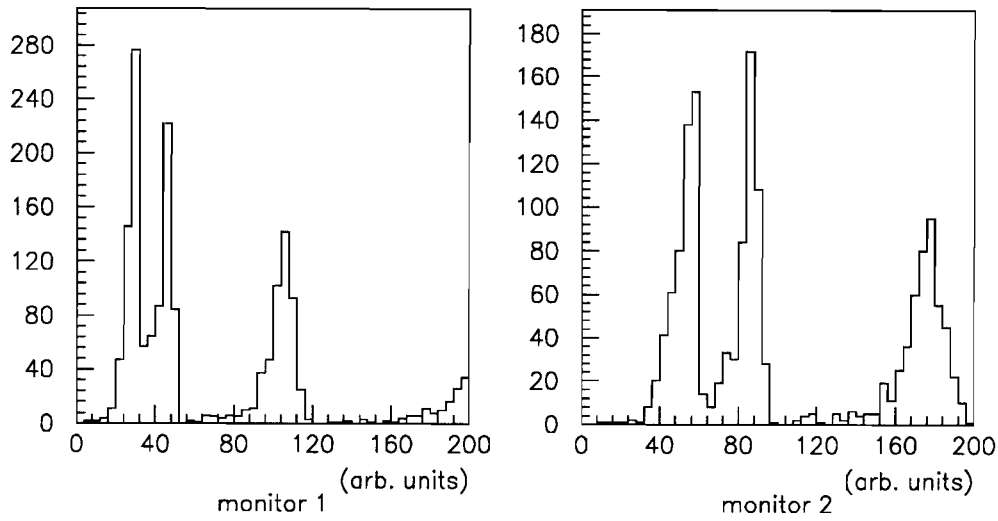

Figure 3.5: Overlap of monitors, caused by laser pulse height jitter. Each monitor is actually the sum of the signals from 25 arbitrarily chosen "well-behaved" tubes. One can see the different runs by the peaks in the distributions. Both monitors are from the same set of runs.

photostatistics in the monitor itself (by having a large number of PMTs, the statistics improve). Also we choose not to sum over all the PMTs in a given system because of the invariable presence of a few bad channels which would degrade the monitor. One can also check the effect of using a PMT based monitor by changing the set of tubes used. Choosing exactly 25 tubes had no special significance, it was merely chosen as a convenient standard.

Once the choice of monitor is made, we pass through the data that will be used in the photoelectron calculation and histogram the monitor amplitude for each laser shot. An example of the resulting distribution is shown in figure 3.5. Note that there is some overlap from run to run. This is caused by the laser pulse height jitter, i.e. a poor pulse from the laser at a given filter setting will have the same value as a good pulse from a run at a lower filter setting. This overlap should be avoided as subtle PMT gain changes from run to run can shift the means of the charge distributions of individual PMTs even though the monitor has the same value. In the overlapping regions, this leads to a broader distribution of pulses for a given monitor value. This extra width,

which has nothing to do with photostatistics, would lead to an underestimation of n_{pe}. Thus we introduce cuts on the monitor value, eliminating the low energy tails and ensuring that no overlap exists so that the monitors constructed for a given run apply only to data in that run.

Calculation of n_{pe}

Once the timing corrections are determined and a good monitor is chosen, we can proceed. The first step is the pedestal subtraction. We first run through the pedestal run (taken with the laser beam blocked) in order to remove the effects of the first contribution to the overall width (σ_1) which is due to UNO, electronics etc. The pedestals for one module are shown in figure 3.6. It should be noted that these "pedestals" are not restricted to values > 0 like one would expect from a typical ADC offset. This is an effect of the sampling-shaping-reconstruction readout system. The next step involves passing through the data, making profile histograms of charge *vs* monitor for each PMT. These profiles are fit to a polynomial which, if the PMTs are linear and the pedestals properly subtracted, is a straight line with an intercept at zero. Some typical plots are shown in figure 3.7.

On a second pass through the data, the residuals from the fit are profiled. The square of the width of the residual distribution as a function of charge in the PMT is what we want. According to our model, this should behave linearly. We then fit this distribution to a straight line (see figure 3.8 for some sample fits for the same tubes shown in figure 3.7).

The slope from this fit is what we are interested in and is in fact the gain[2] G of our model as it relates σ^2 to Q. Hence to get n_{pe} we simply invert the slope and multiply by the conversion factor ($pC \rightarrow GeV$). The conversion factor for the Hall II tests was 4.75 pC/GeV per PMT.

The results for a few modules are shown in figures 3.9, 3.10 and 3.11. Typically

[2]The units of the gain are pC as we used unit charge = 1 for simplicity in the description of the model.

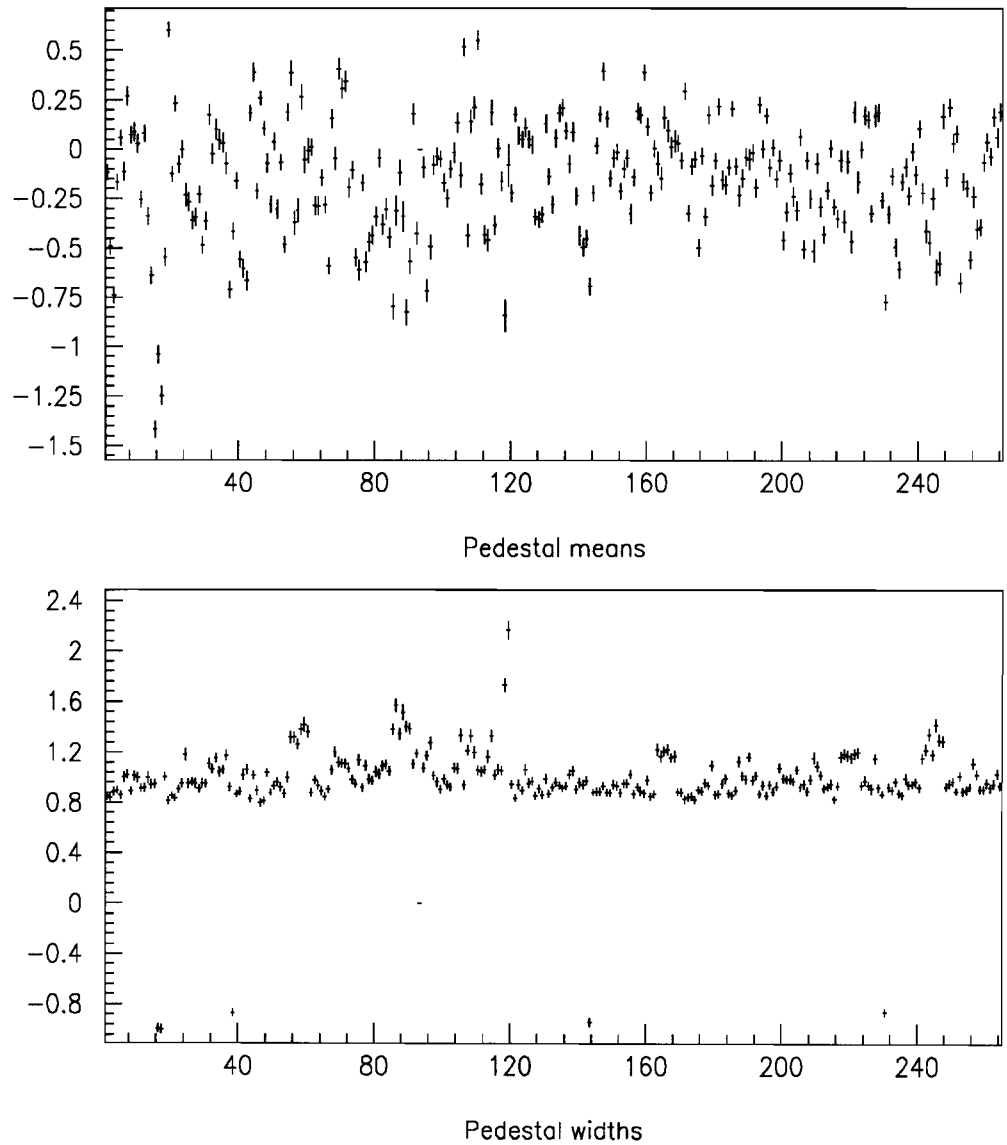

Figure 3.6: Pedestal means and σ's for FCAL module 8. The y axis is in arbitrary units.

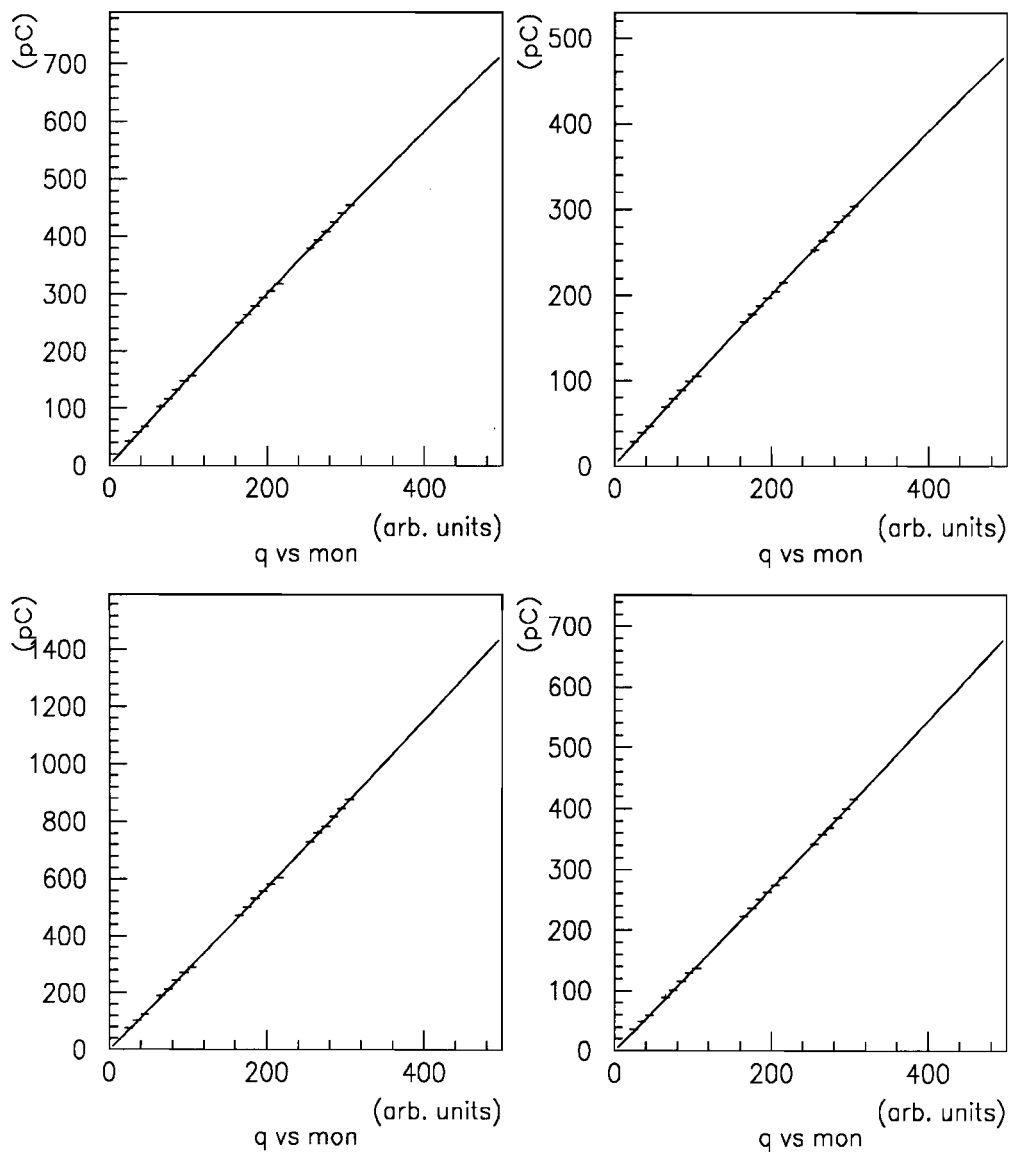

Figure 3.7: Typical Q *vs* monitor plots with straight line fit overlaid.

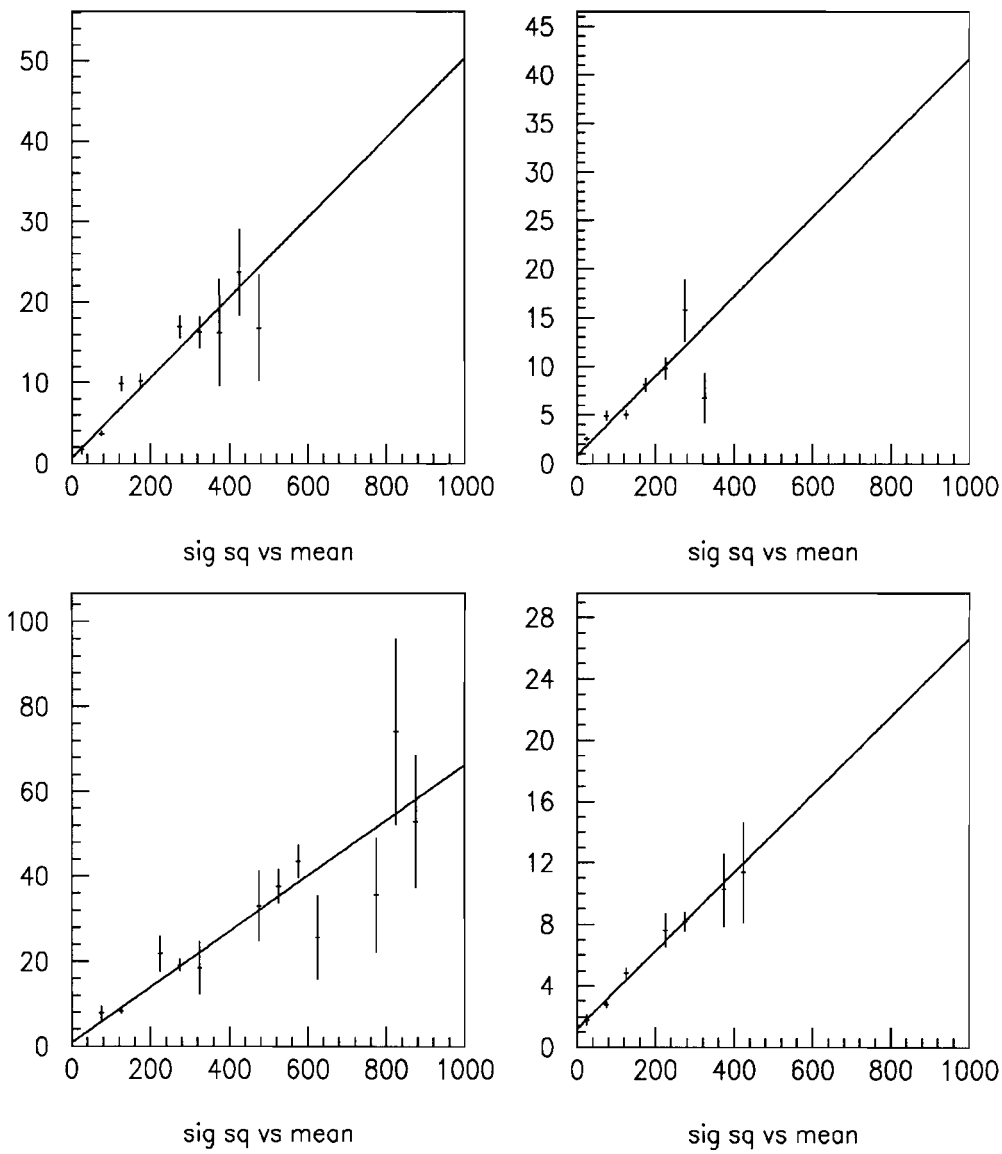

Figure 3.8: Typical σ^2 *vs* Q plots with straight line fit overlaid.

the numbers come from three or four 500 shot runs leading to a error of the order of 10 %. In order to improve the statistical error, one would need an order of magnitude more data for each PMT. Given that there are $\sim$ 12000 PMTs and that the laser cannot fire at rates much greater than 1 Hz, this is not easy to do in practice. The UNO method, as will be described further, is fast and the data takes up much less physical storage space due to the transputer code. One can appreciate the benefits of such a system.

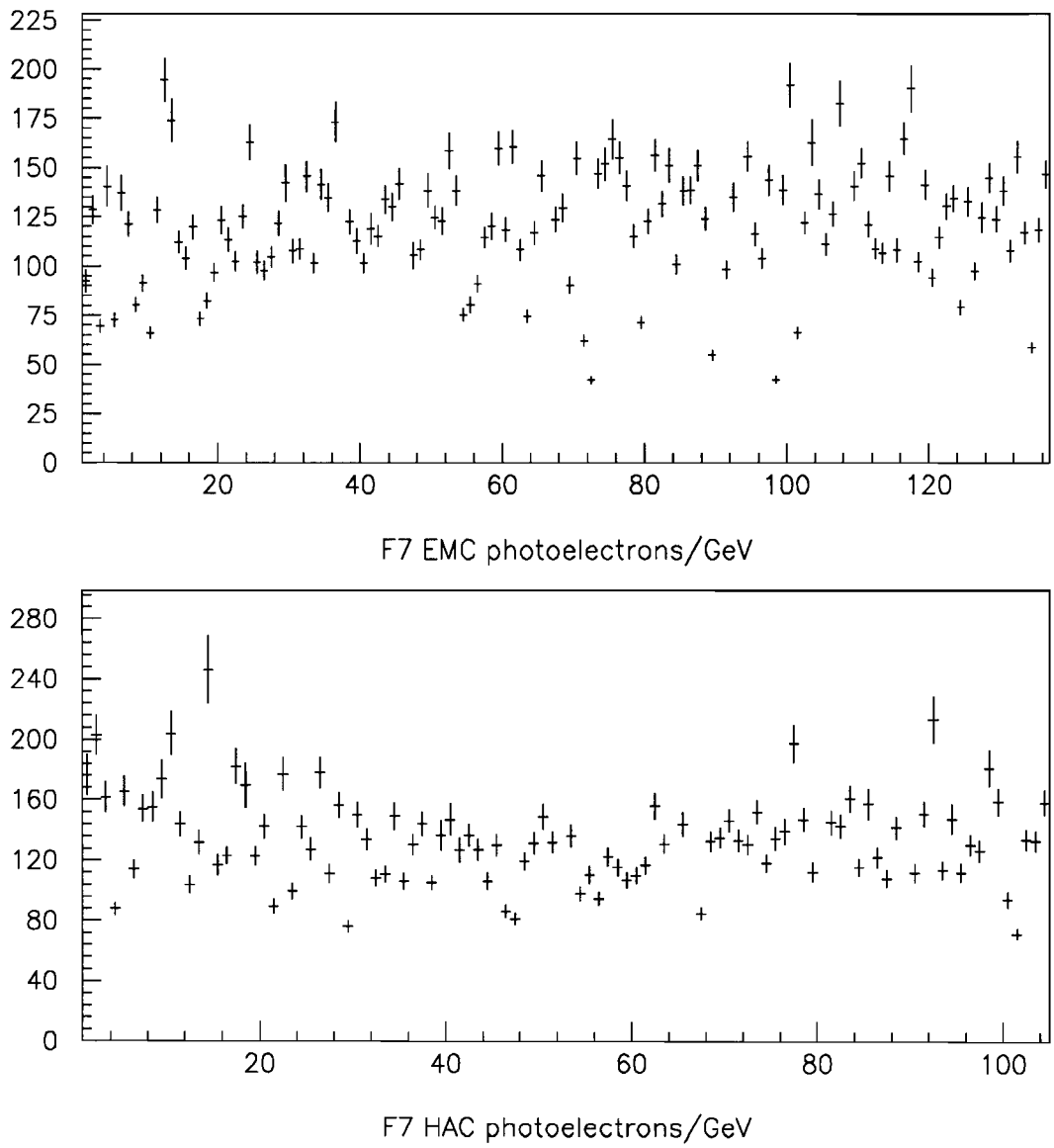

Figure 3.9: Photoelectrons per GeV for module F7 using Hall II method. The upper plot shows the EMC tubes, the lower plot, the HAC tubes.

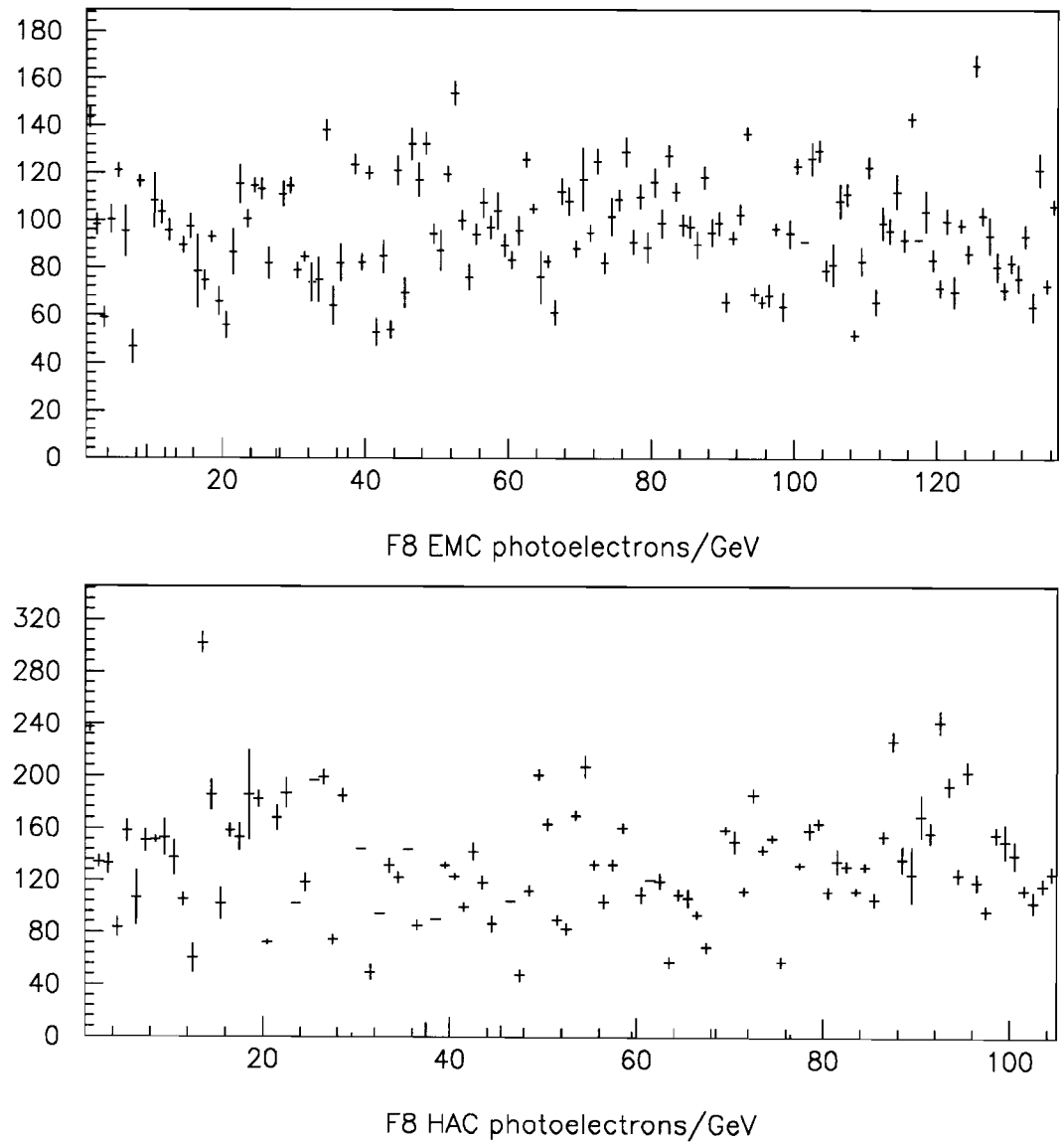

Figure 3.10: Photoelectrons per GeV for module F8 using Hall II method. The upper plot shows the EMC tubes, the lower plot, the HAC tubes.

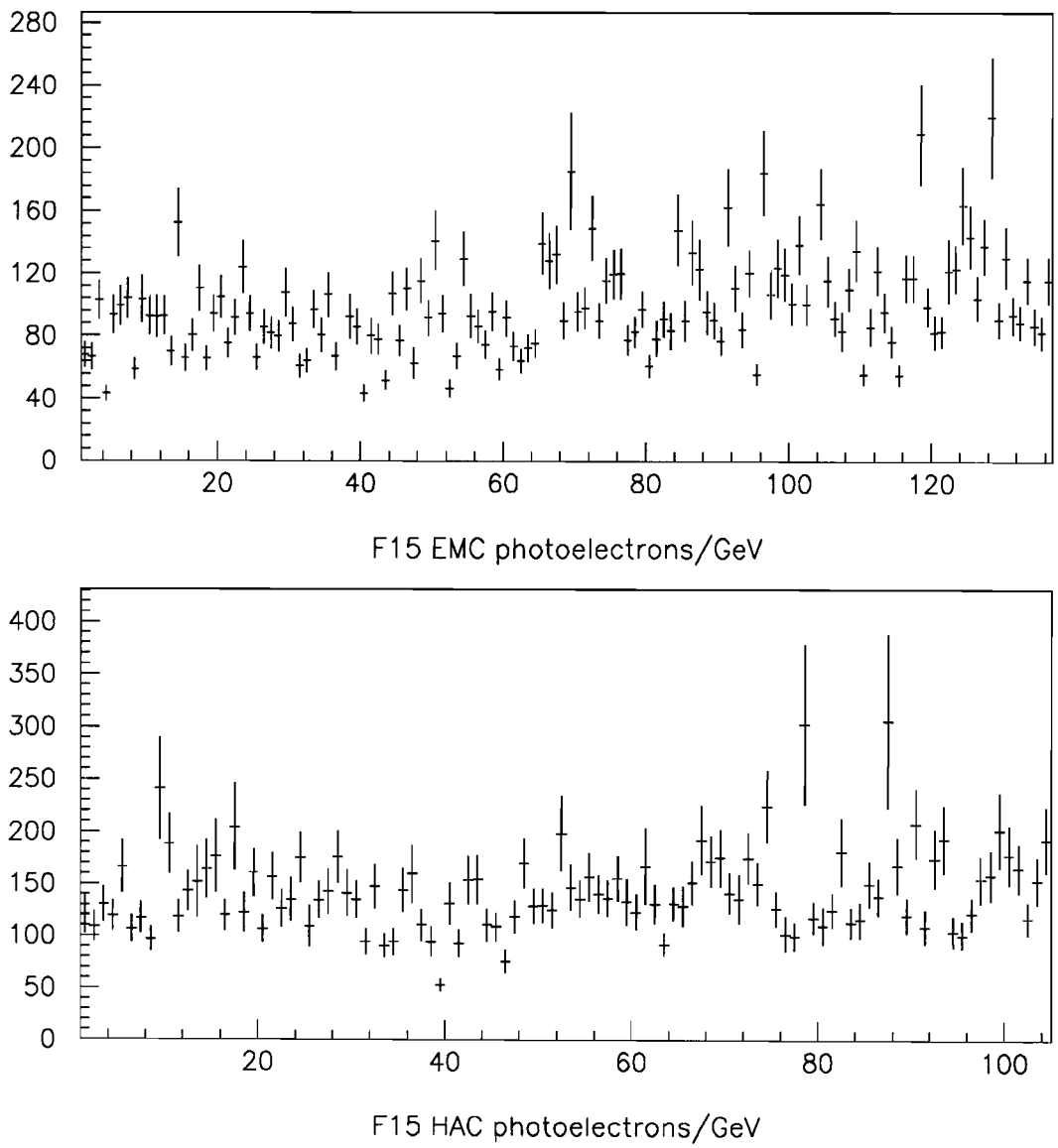

Figure 3.11: Photoelectrons per GeV for module F15 using Hall II method. The upper plot shows the EMC tubes, the lower plot, the HAC tubes.

3.2 UNO Method

3.2.1 Motivation

Instead of flashing light into the PMTs from a test beam, LEDs, or the laser, a new method, which exploits the presence of the uranium noise (UNO) in the calorimeter, was proposed in late 1992. The method also makes use of the computing power of the transputer network of the calorimeter readout. Although the standard readout from the DSPs includes the samples from the PMTs, for certain types of data runs this information is not actually necessary (and in fact for UNO current there are no samples, the signal is simply integrated for 20 ms). Using the transputers, it is possible to perform calculations of the means and sigmas of the charge (and time) for a given number of triggers online instead of later offline. This is useful for calibration type runs, where one is interested in high statistics and one takes large amounts of identical triggers (such as "LED" or "PED" runs). Clearly this is not intended for real physics triggers, where from event to event one has completely different event types and such averages would not be particularly useful. These online "means and sigmas" runs also take less time to complete and typically take up less storage space on disk, allowing for the possibility of daily high precision monitoring of the PMTs stability.

3.2.2 Description of the Model

The method is based on a simple model which is described below [6],[5]. It has been shown that the UNO signal measured in ZEUS type calorimeters (i.e. with uranium-scintillator tiles and WLS optical readout) is well described by an exponential energy spectrum i.e.:

$$dP(E) = Ae^{-E/\epsilon}dE$$

(with a mean energy ϵ) and that the number of UNO pulses, x, within a given gate, τ, obeys a Poisson distribution with mean given by:

$$m = R\tau$$

where

m = Mean number of pulses in the gate τ

and

R = Observed rate of UNO pulses (Hz)

With this it is possible to write the uranium current (I_{UNO})as:

$$I_{UNO} = cR\epsilon$$

where

c = Conversion factor $pC \leftrightarrow GeV$.

Also the uranium noise (which contributes the largest component to the pedestal width measured during a "PED" run), denoted σ^2_{UNO} can be written as:

$$\sigma^2_{UNO} = 2\Delta_s R\epsilon^2$$

where

Δ_s = the effective gate width of the readout electronics and is approximately $347ns$ [3].

Combining these quantities appropriately we can write:

$$\frac{\sigma^2_{UNO}}{I_{UNO}} = \frac{2\Delta_s R\epsilon^2}{cR\epsilon} = (\frac{2\Delta_s}{c})\epsilon$$

where all but ϵ are known constants.

If one now makes the assumption that the energy from the UNO signal seen by a PMT is due to single photoelectrons then n_{pe}, the number of photoelectrons per GeV, is simply given by

$$n_{pe} = 1/\epsilon = (\frac{2\Delta_s}{c})\frac{I_{UNO}}{\sigma^2_{UNO}}$$

[3]The effective gate width of the electronics depends on the choice of algorithm used to reconstruct the charge. The value of 347 ns is for the standard algorithm [1].

It should be noted that this last point is the only special assumption made in the model so far. All other statements (exponential energy distribution, Poisson behaviour of UNO pulses, effective gate width) have been tested experimentally.

3.2.3 Application of the Method

If the width measured for the pedestal distribution of the PMTs was due solely to the UNO contribution then to make the n_{pe} calculation all one would need is a single measurement of I_{UNO} and σ^2 (which would then simply be equal to σ^2_{UNO}) for each PMT. As "UNO" and "PED" runs are an integral part of the normal calibration procedure of the calorimeter (made faster with the transputers), this data is already available and no special run types need to be implemented in addition to those that already exist (this, of course, only matters when ZEUS is in a data taking mode but it is clear that one does not want to introduce any more overhead to the calibration process if one can avoid it).

There are, however, other contributions to the width due to, in particular, the front end electronics connected to the PMT and the PMT base noise which are of roughly the same order of magnitude as σ_{UNO} (though smaller) and must be taken into account. We can write the following:

$$\sigma^2 = \sigma_0^2 + \sigma^2_{UNO}$$

where σ is the total width and σ_0 is the contribution from the front end electronics and PMT base noise.[4] Thus we have:

$$\begin{aligned} \sigma^2 &= \sigma_0^2 + 2R\Delta_s\epsilon^2 \\ &= \sigma_0^2 + \frac{2\Delta_s}{c^2R} I^2_{UNO} \end{aligned}$$

[4]We will see further, however, that this needs to be modified in the low UNO current region as the PMT base noise contribution increases slightly with high voltage in that range.

From the above, we can see that we can also extract the rate of UNO pulses, R, from the slope of σ^2 versus I^2_{UNO} or (using σ_0) as:

$$R = \frac{2\Delta_s}{c^2}\frac{I^2_{UNO}}{\sigma^2 - \sigma_0^2}$$

Thus if we can vary I_{UNO} and measure the corresponding pedestal width at each I_{UNO}, we can extract σ_0 and determine the number of photoelectrons per GeV as:

$$n_{pe} = (\frac{2\Delta}{c})\frac{I_{UNO}}{(\sigma^2 - \sigma_0^2)}$$

where we evaluate at a fixed UNO current which we take to be the nominal value for each tube.

The basic procedure consisted of setting the PMTs to different high voltages (the high voltages settings can be controlled from the equipment computer by issuing commands to a high voltage server running on the equipment computer that controls and monitors the high voltage system of the calorimeter) and taking "UNO" and "PED" runs at each setting. A least squares fit to a straight line through the (I^2,σ^2) points is performed in order to extract σ_0 and the slope for each PMT. The data were taken using the calorimeter stand-alone run control, which is separate from the global DAQ chain and is run from the calorimeter equipment computer. Data were taken during four sessions each spaced roughly a month apart, in order to study the reproducibility of the method. The first session (done on February 23, 1993) was during the winter shutdown period and only BCAL module 29 had high-voltage supplied to its PMTs, the rest of the calorimeter was off. For the subsequent sessions, the entire calorimeter was available and thus it was possible to obtain data for all 11836 PMTs of the calorimeter. Figures 3.12 and 3.13 show plots of σ^2 versus I^2_{UNO} for some PMTs from modules in BCAL and FCAL. Each point corresponds to a different high-voltage setting. The lines through the points are obtained from a least-squares fit used to extract the σ_0's and the slopes (for R). These tubes are from BCAL module 29 and FCAL module 8.

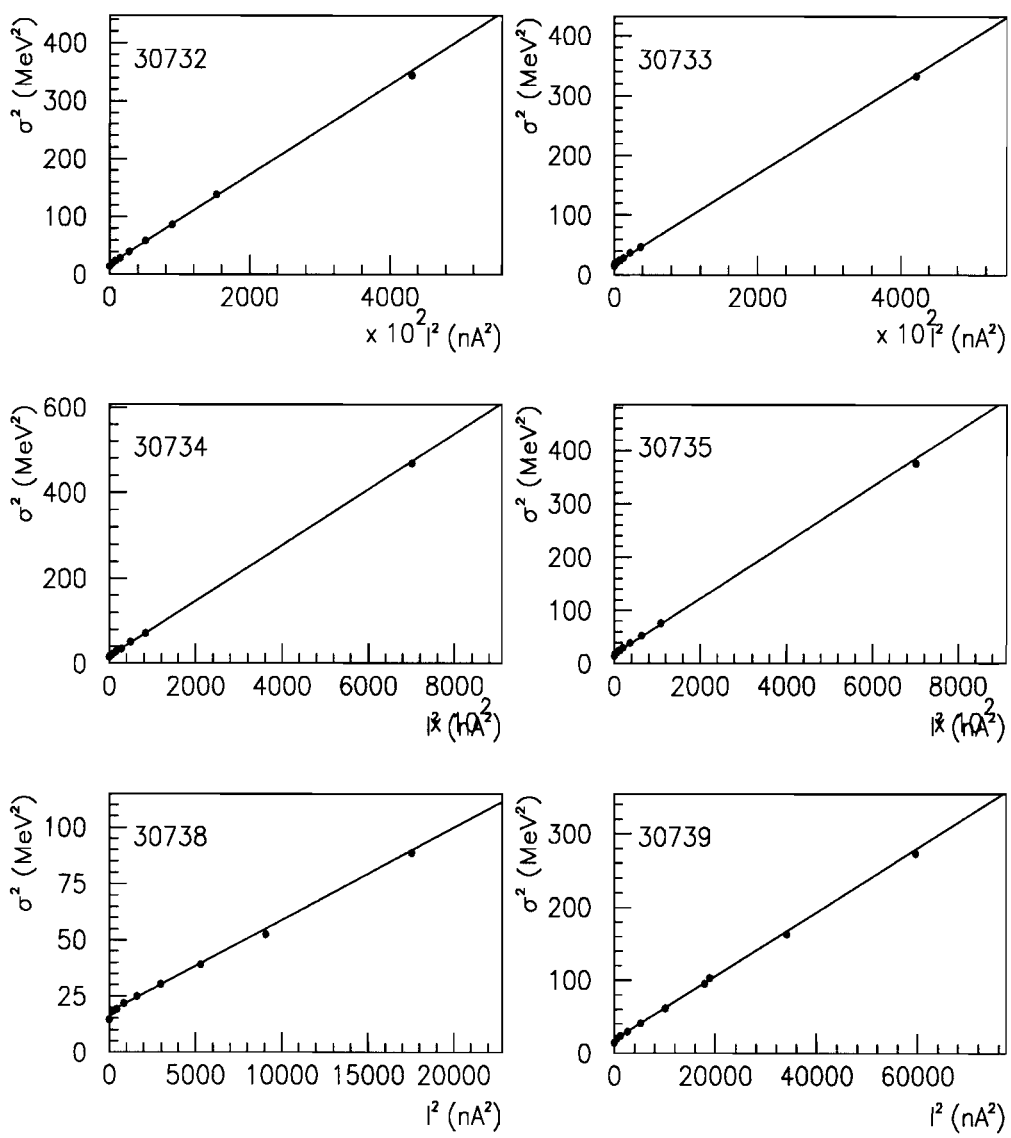

Figure 3.12: Some typical σ^2 vs I^2_{UNO} plots. Note that the error bars are typically smaller than the size of the points which are enlarged solely to aid the eye. These tubes are from module B29.

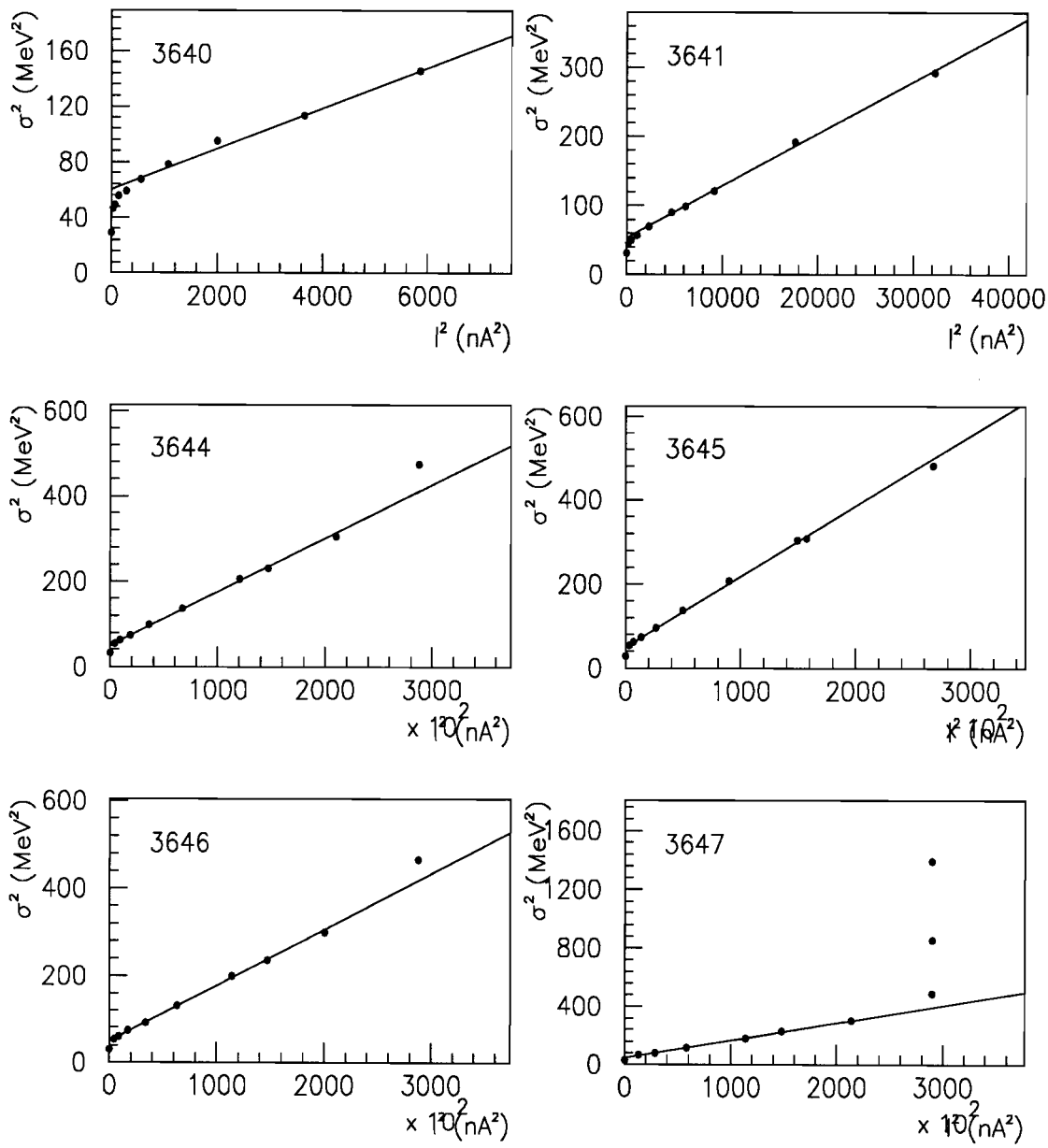

Figure 3.13: Typical σ^2 vs I^2_{UNO} plots. Note that some tubes display saturation of the I_{UNO} current integration circuit at around 29000 $(nA)^2$. These tubes are from module F8.

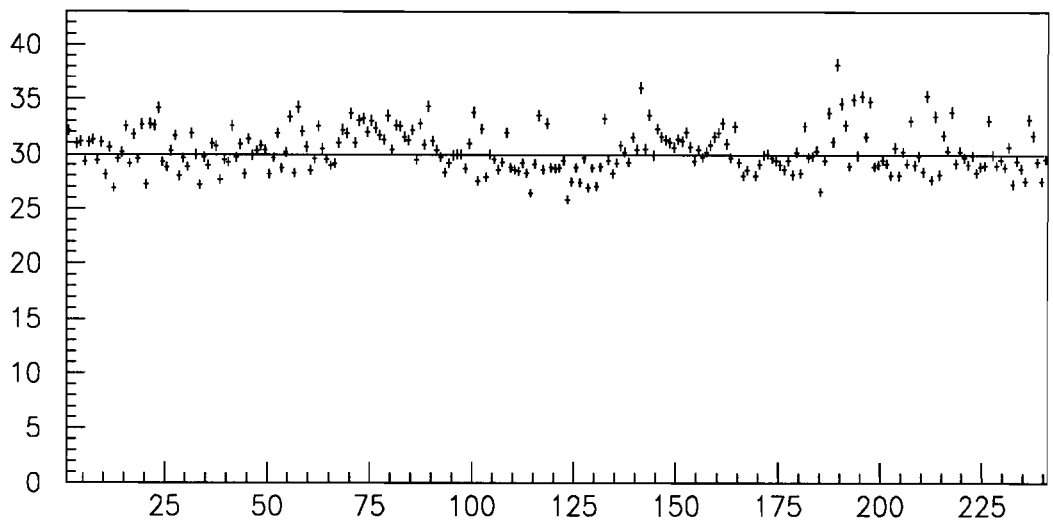

Figure 3.14: σ_E^2 for module F8. The line at 30 (MeV^2) is to guide the eye.

3.2.4 Contributions to the Total Width

Close inspection of a given σ^2 vs I_{UNO}^2 plots reveals that the points do not follow a straight line all the way down to $I_{UNO} = 0$. In the low I_{UNO}^2 region ($\sim 2000\ nA^2$) the points fall away from the line, intercepting the σ^2 axis lower than one would expect from an extrapolation of a straight line derived from the higher I^2 points (or from a fit to these points).

This behaviour can be thought of as due to the contribution of PMT base noise to the width. We can rewrite the total width, separating the two contributions to σ_0 as follows:

$$\sigma^2 = \sigma_B^2 + \sigma_E^2 + \sigma_{UNO}^2$$

where the subscript B denotes PMT base noise and E refers to the front end electronics noise.

The electronics contribution has been shown to be roughly Gaussian and also independent of charge (and hence I_{UNO}). It can be estimated from the value of σ^2 obtained with the high voltage off. A plot of σ_E^2 for the tubes of module F8 is shown in figure 3.14.

The other component that we consider is the PMT base noise. If we fit excluding

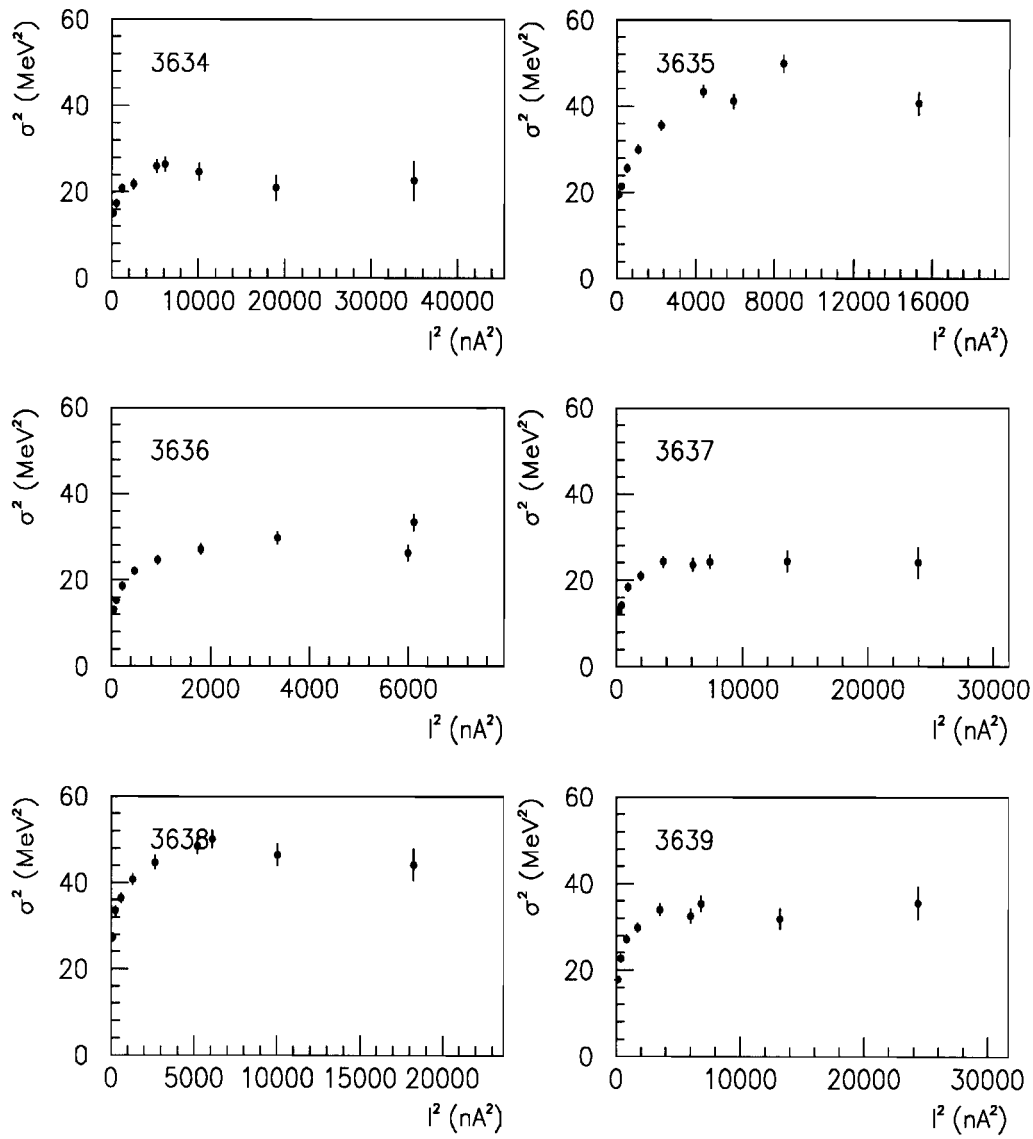

Figure 3.15: PMT base noise as a function of UNO current. Module F8 tubes.

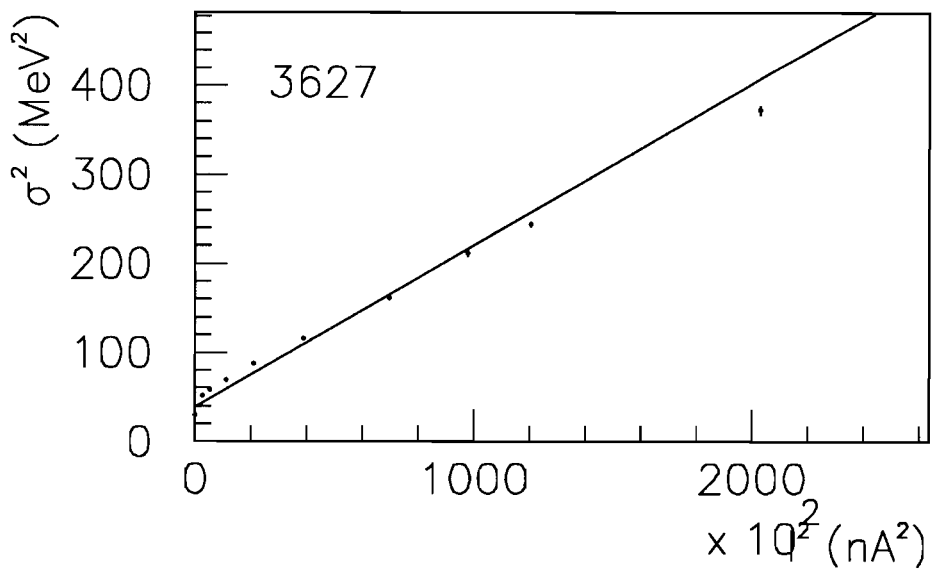

Figure 3.16: Effect of including all HV points in fit, one can plainly see how the slope of the fit is overestimated, leading to an underestimation of n_{pe}.

the low I_{UNO} points, we can estimate σ_B at each I_{UNO} point by evaluating σ_{UNO} from the slope and calculating

$$\begin{aligned} \sigma_B^2 &= \sigma^2 - \sigma_E^2 - \sigma_{UNO}^2 \\ &= \sigma^2 - \sigma_E^2 - \frac{2\Delta_s}{c^2 R} I_{UNO}^2 \end{aligned}$$

to extract the base noise. Some plots of σ_B versus I_{UNO} are shown in figure 3.15. One can see that σ_B rises sharply in the low I_{UNO}^2 region and tapers off at higher values. Interesting as it is, to fully investigate this source of noise would lead us too far afield for the purposes of this thesis. It is enough to note that at high I_{UNO}^2, the PMT noise reaches a constant value and we can use σ_0 obtained from fits as long as we are careful to exclude the lower I_{UNO} points (see for example, figure 3.16 for an example of a fit including all the points). One can see how the slope is increased and the resulting σ_0 is artificially lowered. The low I_{UNO} region (the 4 or 5 lowest high voltage points) is excluded from the fits used to obtain the results shown further.

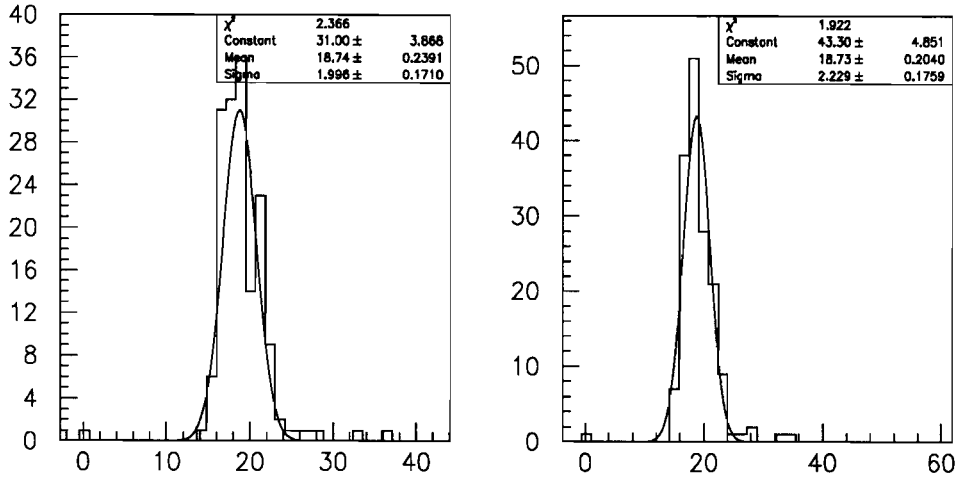

Figure 3.17: Distribution of σ_0. Left plot: April 15, right plot: May 12. A Gaussian fit is superimposed.

3.2.5 Reproducibility

With the above considerations, reproducibility of the method was examined by comparing the values of σ_0 and n_{pe} obtained for the two last sessions. (the March 19 session is not used as the poor choice of high voltage settings results in too many low I_{UNO} points). The results for σ_0 are quite consistent and are shown in figures 3.17 and 3.18. Also shown are some comparisons of n_{pe} in figure 3.19 and 3.20. The typical statistical errors on n_{pe} for a given PMT are of the order of 2% for both runs shown in these plots. Thus the error on the ratio will be $\approx \sqrt{2} \cdot \delta_{n_{pe}} \approx 3\%$. Therefore the width of figure 3.19 is consistent with the statistical errors of the individual PMTs. These results are from module B29.

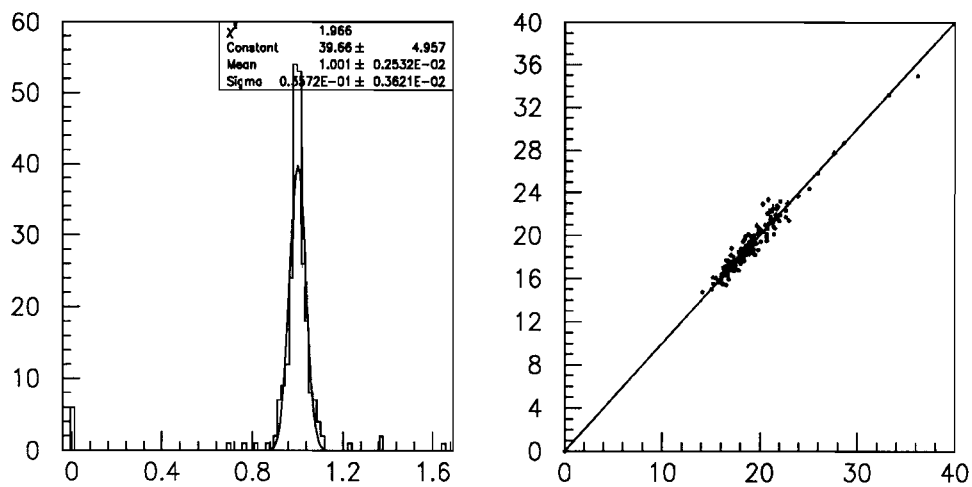

Figure 3.18: Left: ratio of σ_0 for May 12 and April 15. A Gaussian fit is superimposed. Right: correlation plot of the σ_0's from the two runs. Note that the 45° line is merely to guide the eye.

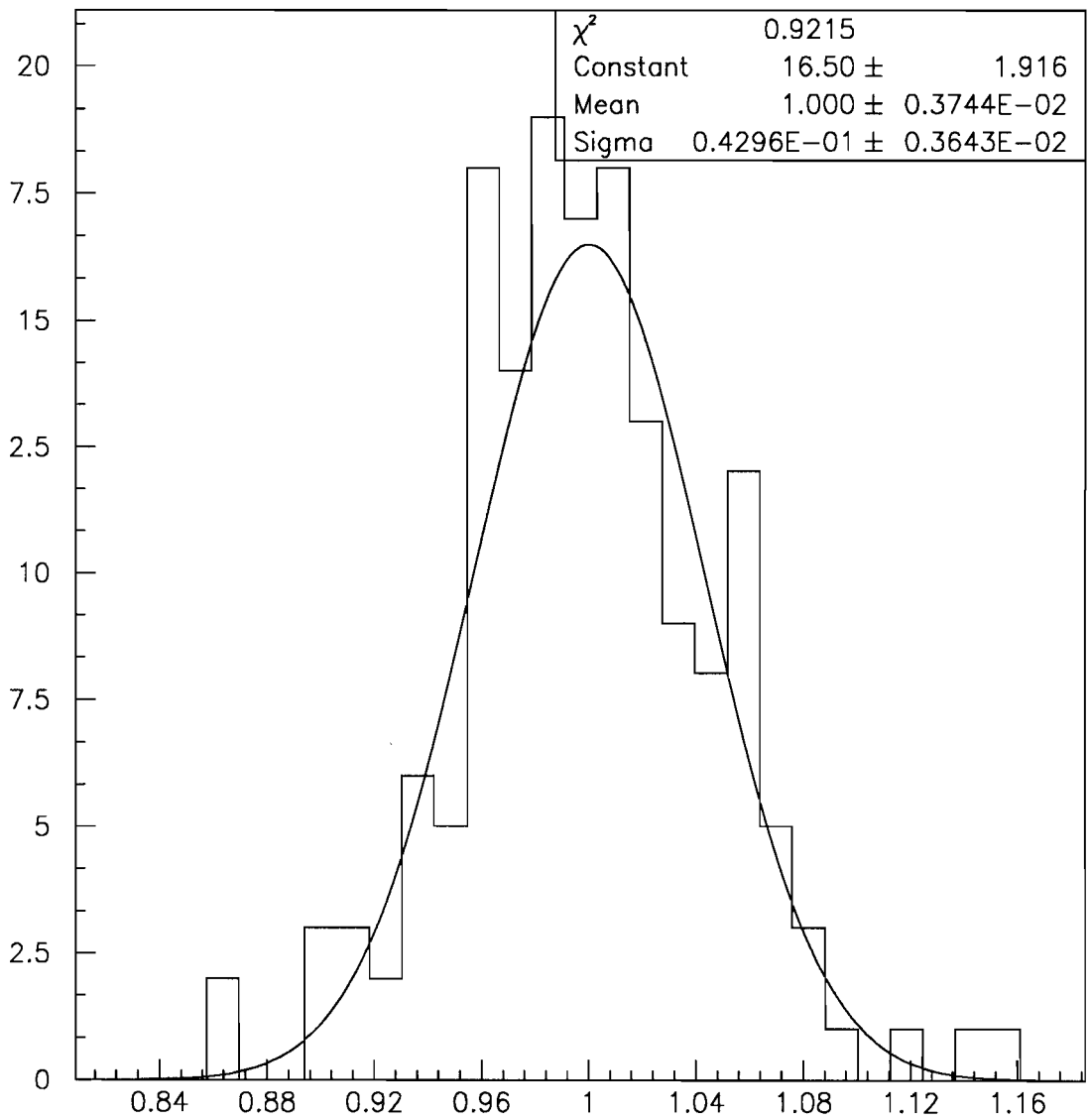

Figure 3.19: ratio of n_{pe} calculated from May 12 and April 15 data. Module B29.

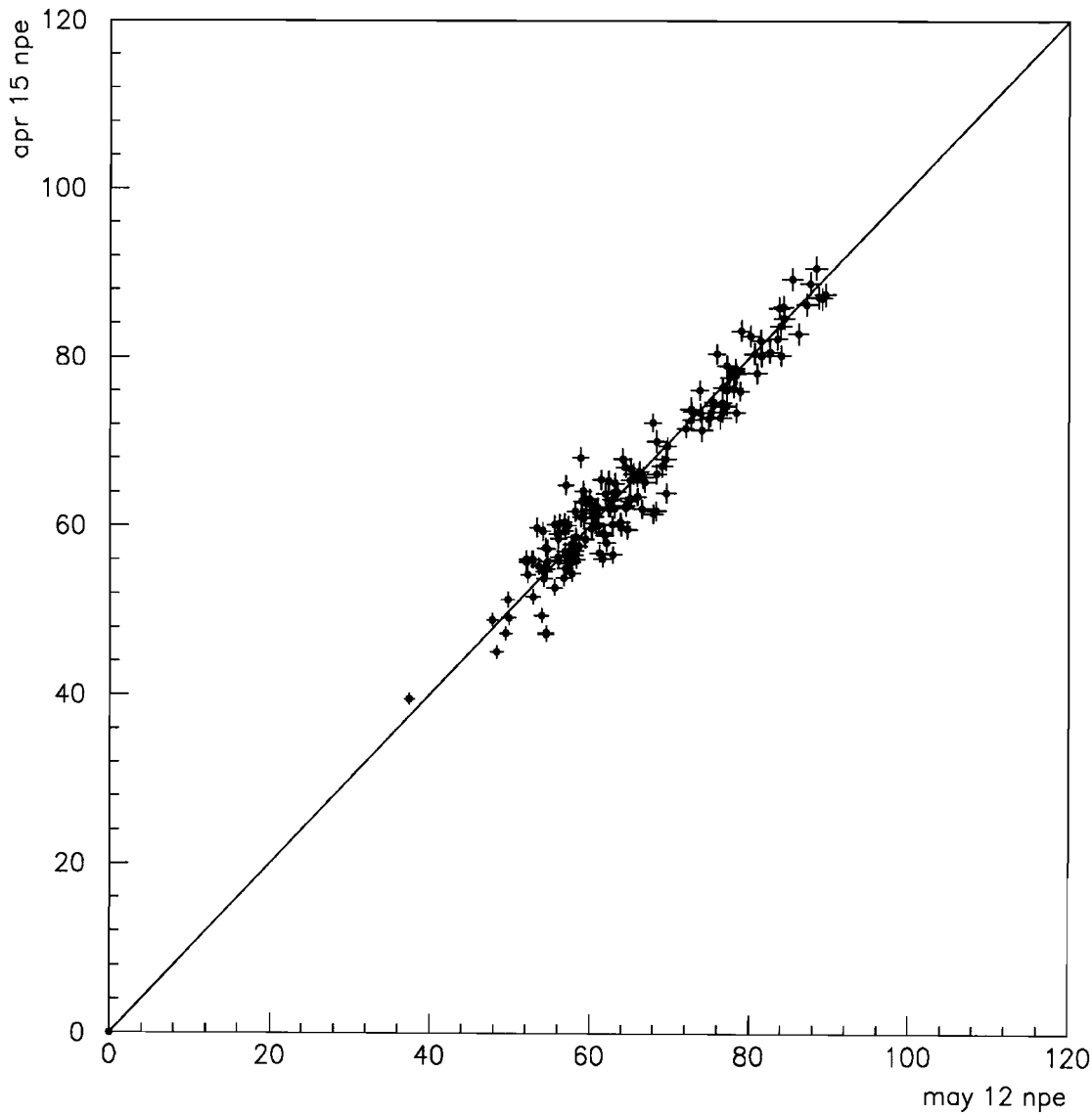

Figure 3.20: correlation plot of n_{pe} from May 12 and April 15 data. Module B29.

3.2.6 Results of n_{pe} and R Calculations

This chapter concludes with some results of R and n_{pe} calculations for representative modules. Figures 3.21 , 3.22 and 3.23 show the observed UNO rates, R, derived from the slopes of the fits for representative modules in FCAL, BCAL and RCAL. For the rate calculation, some comments are in order. Although we cannot measure the absolute rate of UNO pulses with this method (due to the intervening attenuation lengths of the scintillator and WLS as well as the quantum efficiency of the PMT photocathode), the relative rates from the HAC and EMC sections should be consistent with the relative amount of uranium in these sections. We can clearly see that the rates are different for the EMC (lower points) and HAC (upper points) tubes. Consider the rates for F8 in figure 3.21. From the plot, the ratio of the rate for the HAC tubes (upper points around 3000 KHz) to the EMC tubes (the lower points clustered around 500 KHz) is ~ 6. The EMC sections consist of 25 layers of $5\,cm \times 20\,cm$ whereas the HACs are 80 layers $\times 20\,cm \times 20\,cm$ giving a ratio of ~ 13. The rates do not seem to scale as we expect. Whether this is due to a problem with the model or to other factors (different PMTs for EMC and HAC sections, different lengths of WLS for EMC and HACs, etc.) is not clear. Further investigation of this is certainly warranted.

Figures 3.24 , 3.25 and 3.26 show the corresponding n_{pe} for these modules. One notices immediately that the numbers are lower than those of the corresponding Hall II data (and of the LED data shown in the next chapter). The large errors bars on the RCAL HAC tubes illustrate the effect of a shorter lever arm in the fit as many of the HV points had to be excluded due to early saturation of the UNO circuit as well as those in the low I_{UNO} region due to the effects of the PMT base noise. It should be stated that if the UNO method is to become a "standard", a more optimized choice of high voltage settings should be made, for instance such as taking settings at HV_{NOM}, $HV_{NOM} - 50\,V$, $HV_{NOM} + 50\,V$ or something similar to avoid problems with saturation of the UNO integration circuit at the high end and PMT base noise at the low.

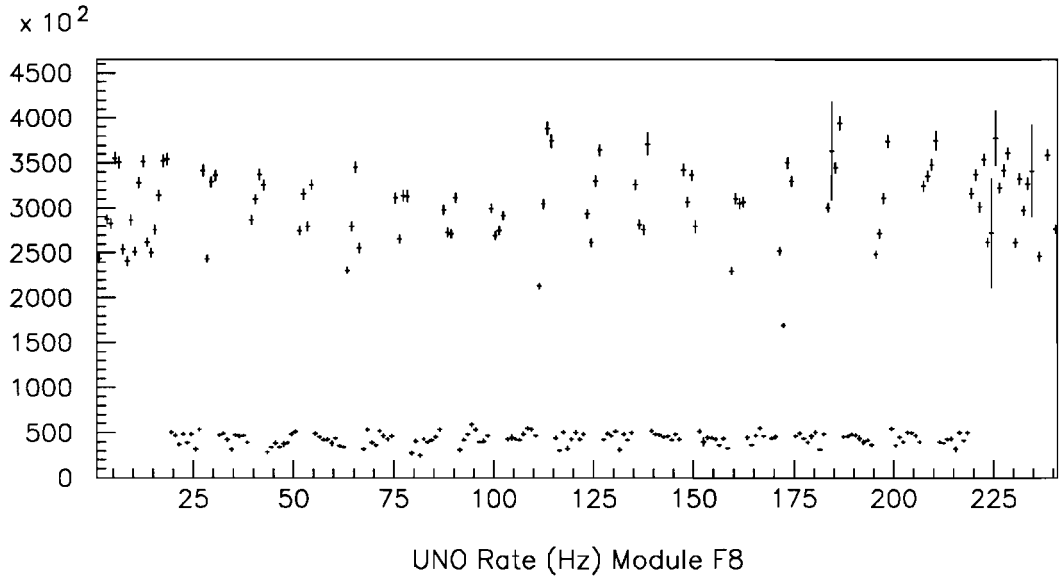

Figure 3.21: Observed UNO rate in Hz for module F8.

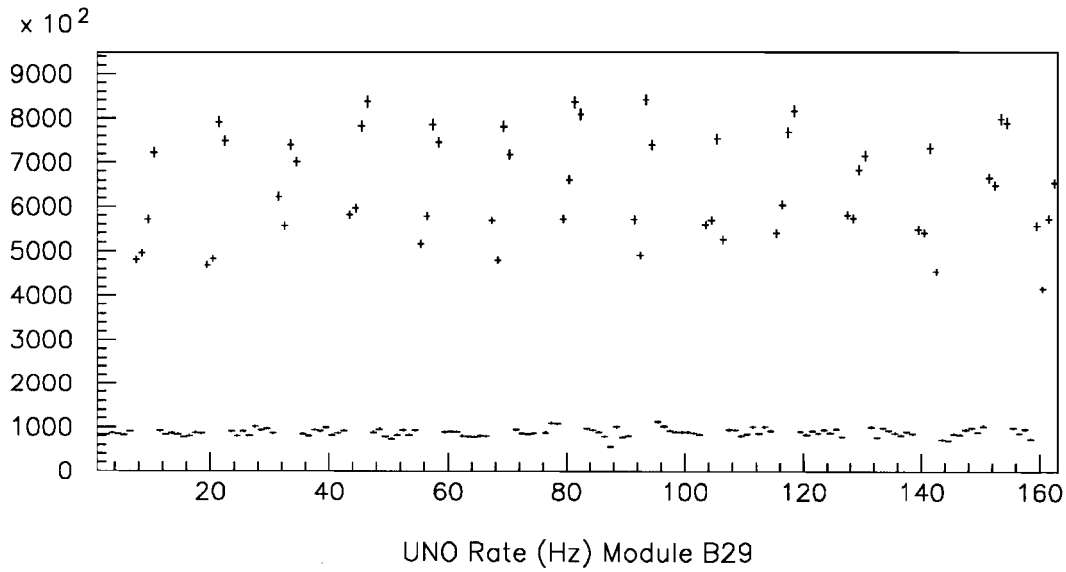

Figure 3.22: Observed UNO rate in Hz for module B29.

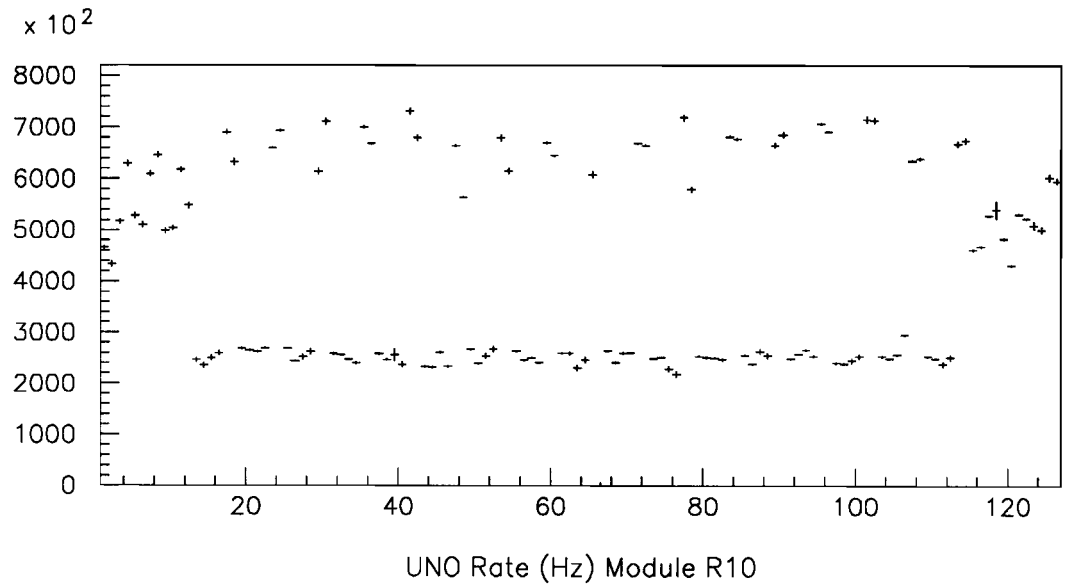

Figure 3.23: Observed UNO rate in Hz for module R10.

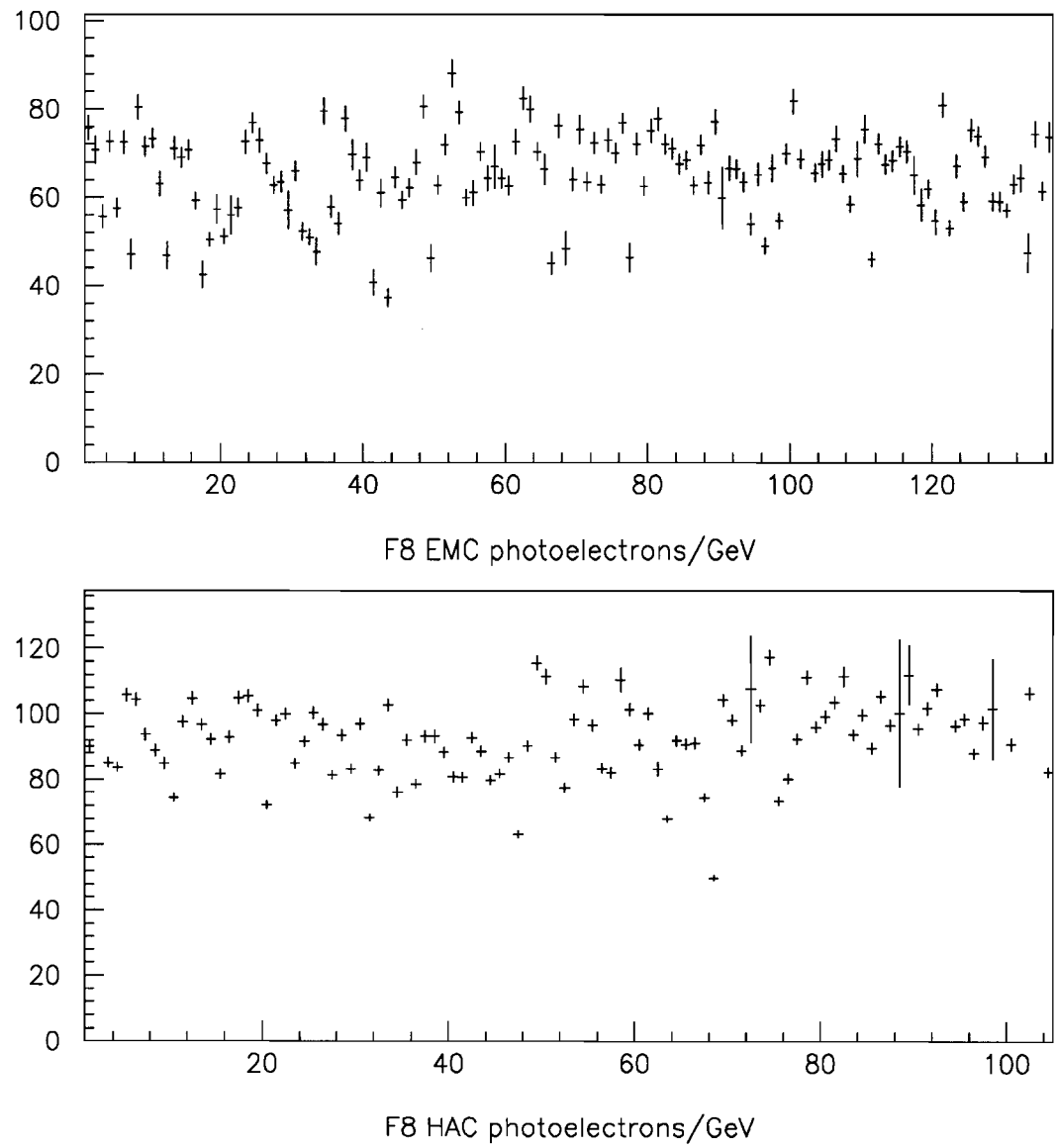

Figure 3.24: Photoelectrons per GeV for module F8 using the UNO method. The upper plot shows the EMC tubes, the lower plot, the HAC tubes.

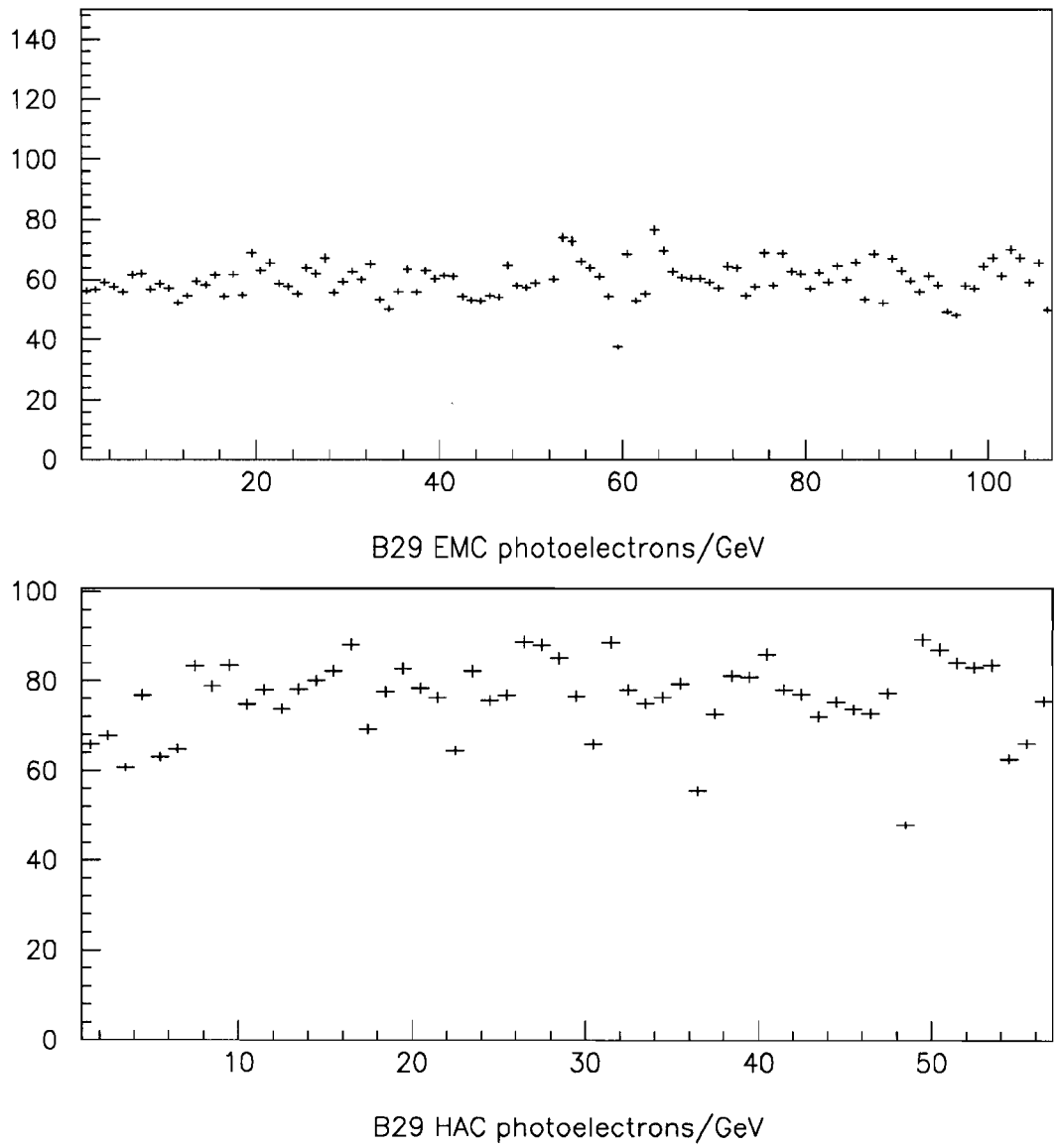

Figure 3.25: Photoelectrons per GeV for module B29 using the UNO method. The upper plot shows the EMC tubes, the lower plot, the HAC tubes.

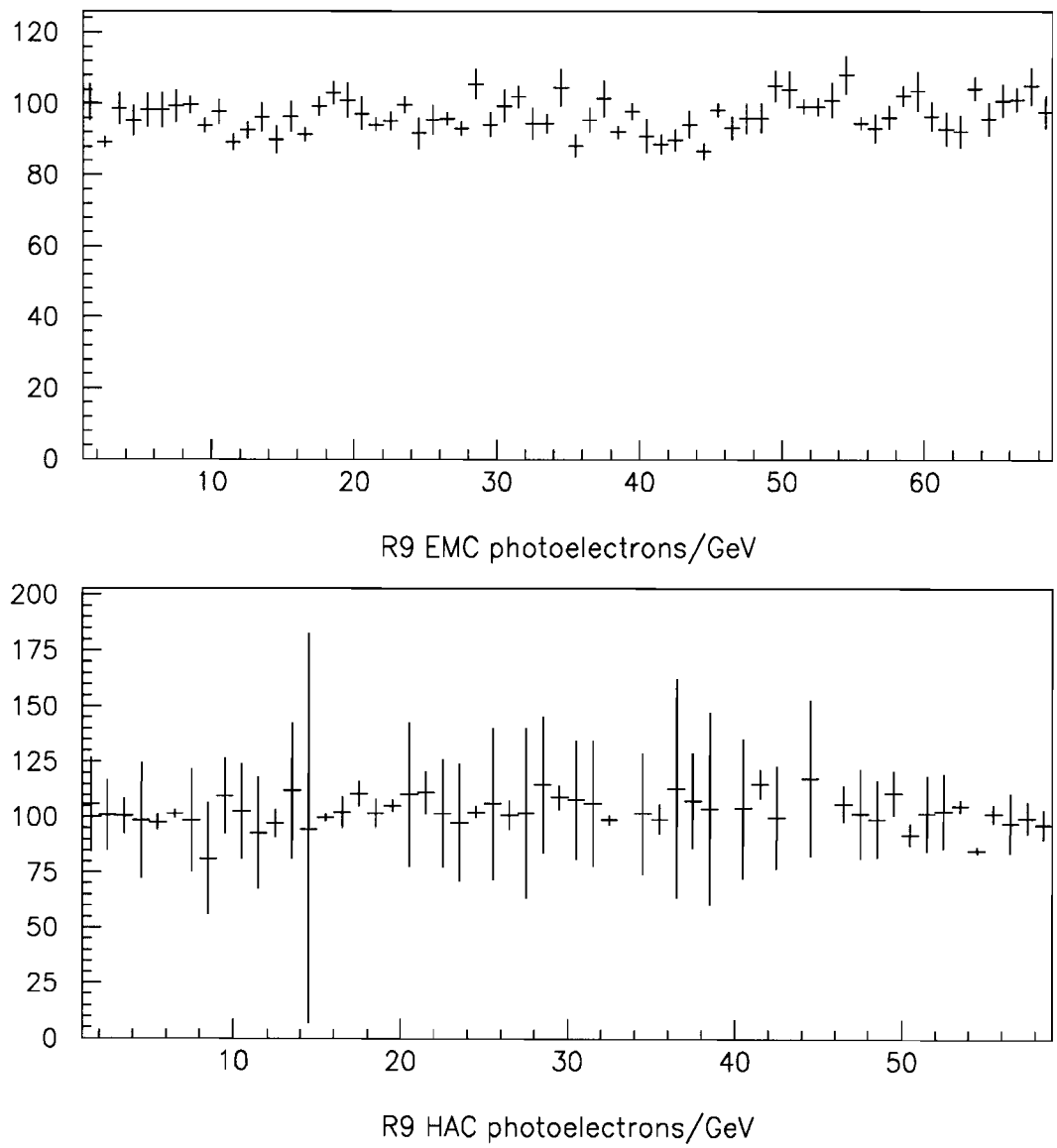

Figure 3.26: Photoelectrons per GeV for module R9 using the UNO method. The upper plot shows the EMC tubes, the lower plot, the HAC tubes. Note the particularly large error bars for the HACs due to the non-optimal choice of high voltage settings resulting in fewer points included in the fit.

Chapter 4

Comparisons of Results

In this chapter, comparisons of the results from the Hall II and UNO methods to LED n_{pe} and recent laser results are presented. The LED data was obtained from October 26 to November 13, 1992 and consists of 4788 LED events per PMT. This particular set of data was chosen for comparison purposes because it covers all of F/RCAL.

We use the new laser n_{pe} data (obtained using a method similar to the Hall II method) to compare to the UNO BCAL data since there is no LED system for BCAL. The data were obtained with the Molectron laser in the spring of 1993.

4.1 Hall II – LED/Laser comparison

Correlation plots of Hall II *vs* LED data are shown for EMC and HAC tubes of FCAL modules F7, F8 and F15 in figures 4.1, 4.2; 4.3, 4.4 and 4.5, 4.6 respectively. Also a comparison of the Hall II *vs* spring 93 laser data is shown in figures 4.7 and 4.8. The line drawn in all the plots represents a slope of 1 in order to guide the eye.

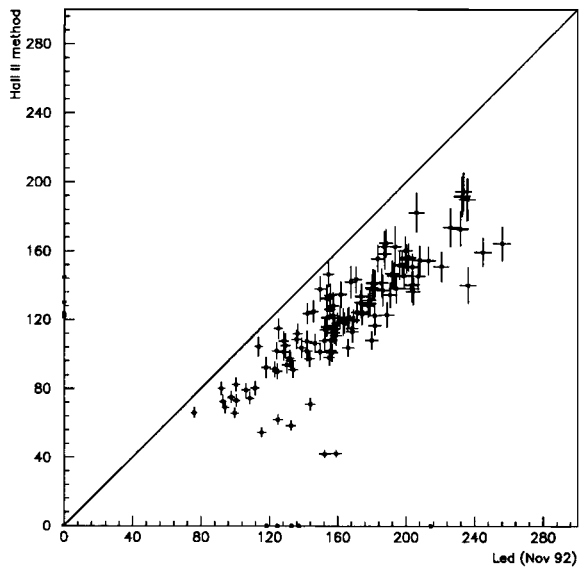

Figure 4.1: Hall II laser–LED n_{pe} correlation, EMC tubes, FCAL 7.

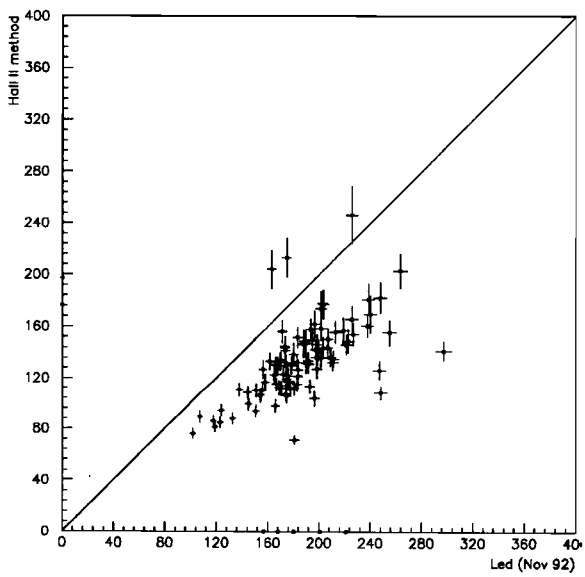

Figure 4.2: Hall II laser–LED n_{pe} correlation, HAC tubes, FCAL 7.

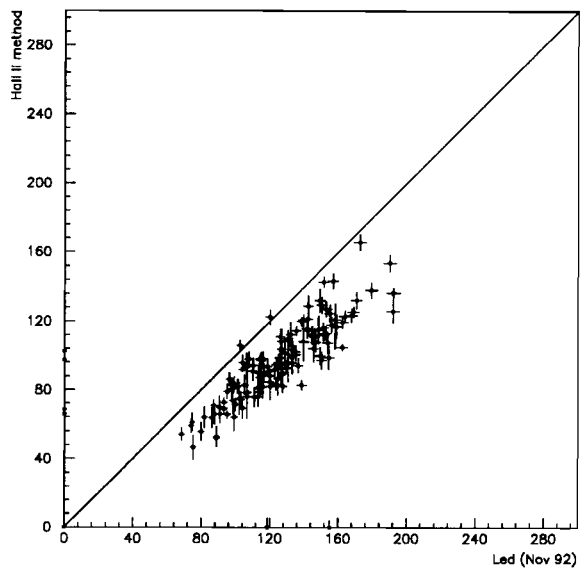

Figure 4.3: Hall II laser–LED n_{pe} correlation, EMC tubes, FCAL 8.

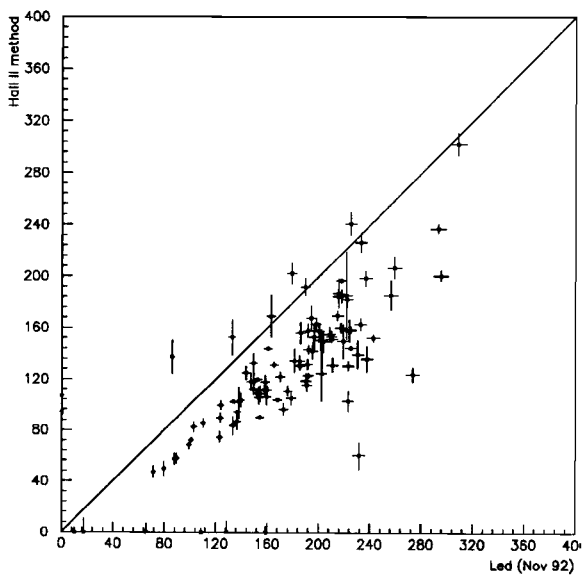

Figure 4.4: Hall II laser–LED n_{pe} correlation, HAC tubes, FCAL 8.

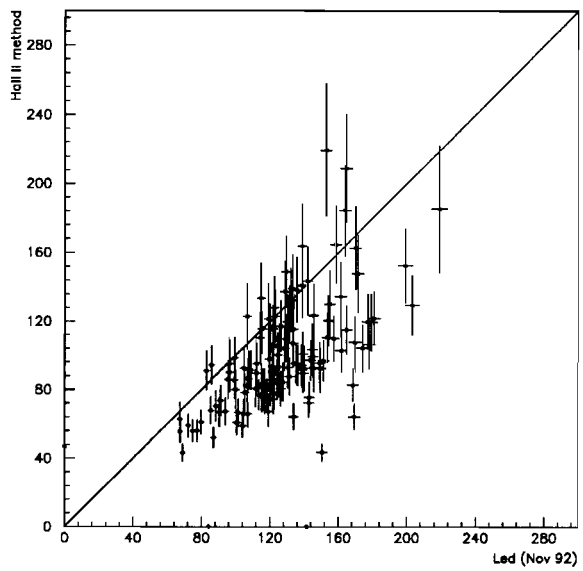

Figure 4.5: Hall II laser–LED n_{pe} correlation, EMC tubes, FCAL 15.

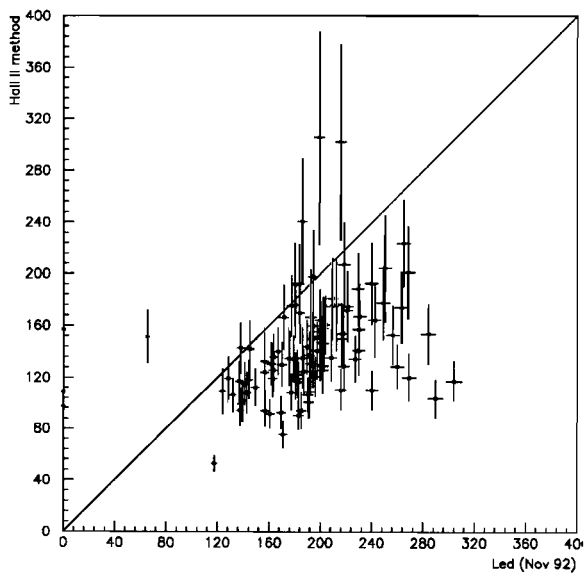

Figure 4.6: Hall II laser–LED n_{pe} correlation, HAC tubes, FCAL 15.

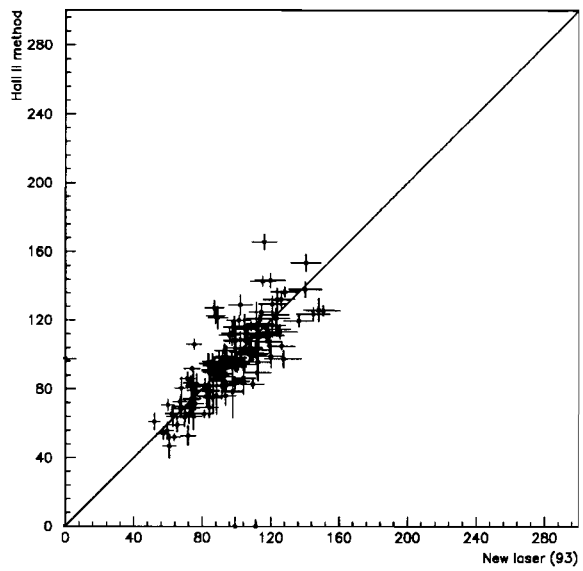

Figure 4.7: Hall II laser–Laser (93) n_{pe} correlation, EMC tubes, FCAL 8.

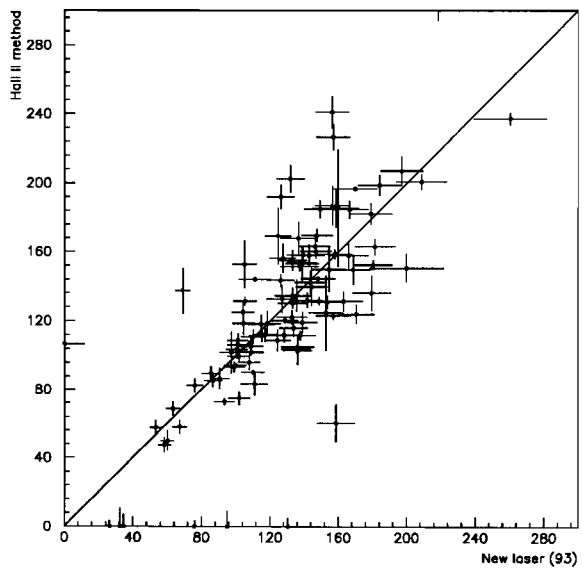

Figure 4.8: Hall II laser–Laser (93) n_{pe} correlation, HAC tubes, FCAL 8.

From the plots one can clearly see that the laser results consistently underestimate the LED numbers. There is a good correlation between the two (Hall II and 1993) laser results for module F8. Although the Hall II and LED data correlate, there is a systematic scale difference with a slight offset. Also the error bars of the Hall II results are larger due to the smaller amount of data ($\sim 1500 - 2000$ shots compared to the $\sim$ 5000 shots for the LED). A possible source of the systematic difference is the LED pulse shape effect[1], known to be on the order of a few %. Despite the time separation between these two measurements, the correlation is rather good.

4.2 UNO – LED/Laser comparison

In this section, correlation plots of UNO *vs* LED and recent laser data are shown for some representative modules (figures 4.9 and 4.10 show module F8, figures 4.11 and 4.12 show module R10 for the F/RCAL modules and BCAL modules 10 and 29 are compared with laser data in figures 4.13 and 4.14 and figures 4.15 and 4.16). One can see clearly from the plots that the UNO n_{pe} and LED data correlate well but are far from being equal. The error bars are statistical. The BCAL modules on the other hand seem to have better agreement between the UNO and laser data, although for the EMCs, the points tend to cluster around a central value, and thus the correlation is not totally clear. The larger error bars on the laser data are due to the lower statistics available. One observes that the UNO results for n_{pe} seem to "saturate"[2] at $\sim$ 100 photoelectrons/GeV. Recall that the UNO method relies on one particular assumption that could very well not hold. Specifically, the assumption that the UNO signal produces single photoelectrons at the photocathode was suggested as a reasonable first guess. The results here would suggest that this probably not be the

[1] Recall that the shaper response assumes a delta function input, for particle signals or the laser this is a good approximation. The LED input pulse shape is quite different and additional corrections have to be applied to the charges obtained from the readout [23].

[2] It should be made clear that by calling this effect "saturation", we do not mean actual saturation of the PMTs, it is merely jargon that describes the shape of the correlation.

Module	Type	Hall II	UNO	LED	Laser (93)
F7	EMC	125 ± 50	74 ± 11	164 ± 47	-
F7	HAC	129 ± 45	95 ± 10	181 ± 40	-
F8	EMC	95 ± 33	67 ± 12	164 ± 40	97 ± 28
F8	HAC	134 ± 62	94 ± 17	164 ± 40	138 ± 57
F15	EMC	95 ± 32	65 ± 10	164 ± 47	-
F15	HAC	130 ± 72	97 ± 8	164 ± 47	-
B10	EMC	-	73 ± 5	-	65 ± 11
B10	HAC	-	94 ± 14	-	89 ± 30
B29	EMC	-	60 ± 7	-	54 ± 11
B29	HAC	-	76 ± 27	-	86 ± 47

Table 4.1: Summary of module averaged n_{pe}s for some of the modules presented in this thesis. Note that the RCAL modules are not shown here as there are too few EMC and HAC tubes per module to make sensible Gaussian fits.

case. One could suggest that in fact the UNO signal produces some small number of photoelectrons (on the order of 1) such that the quantity $1/\epsilon$ would not be equal to n_{pe}. The rough agreement for the BCAL modules may be explained by the fact that the BCAL modules have less efficient light transmission (in the scintillator and WLS) than F/RCAL. This could have the effect of making the single photoelectron model applicable in this case. In fact, one can see that some of the BCAL HAC tubes seem to show the onset of the "saturation" effect that is so evident in RCAL. To finish this section, table 4.2 shows the module averaged n_{pe} (with the σ of the distribution) for the various modules and methods described in this thesis.

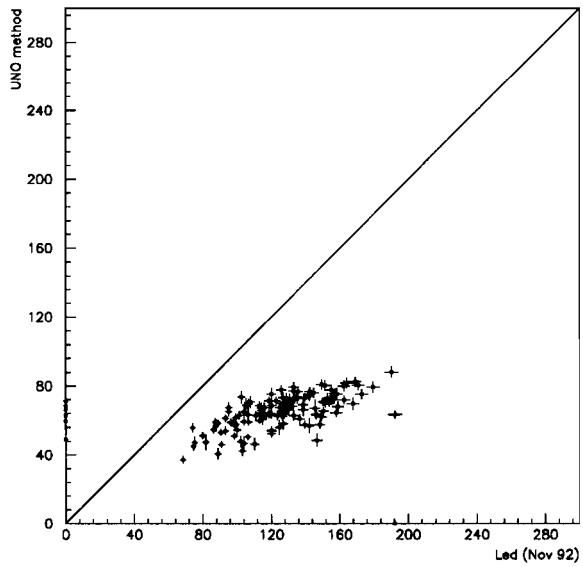

Figure 4.9: UNO–LED n_{pe} correlation, EMC tubes, FCAL 8.

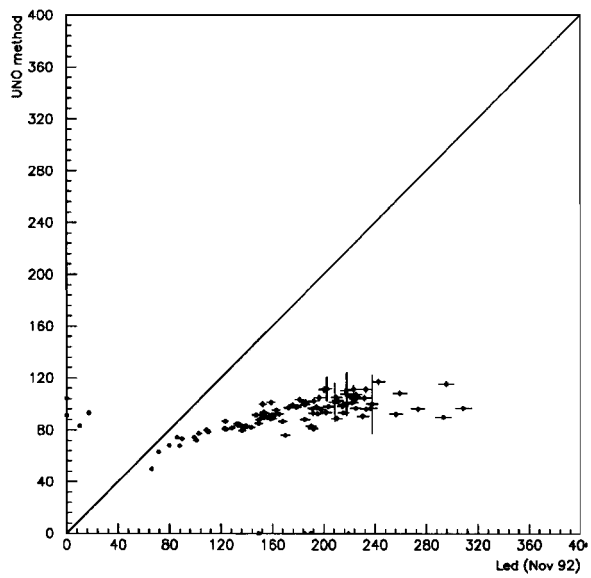

Figure 4.10: UNO–LED n_{pe} correlation, HAC tubes, FCAL 8.

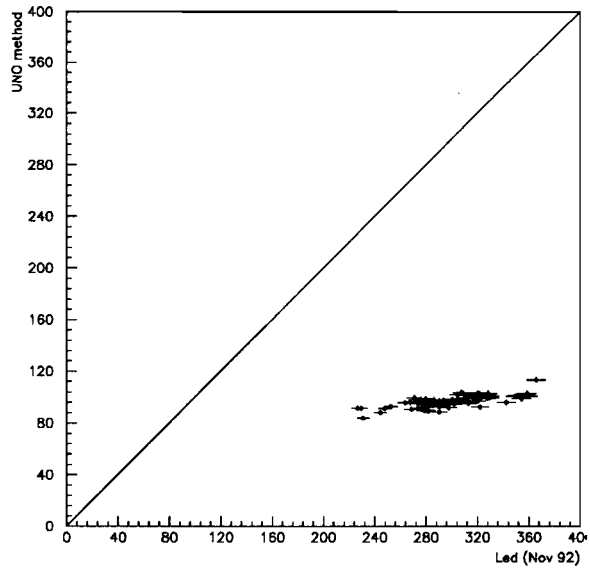

Figure 4.11: UNO–LED n_{pe} correlation, EMC tubes, RCAL 10.

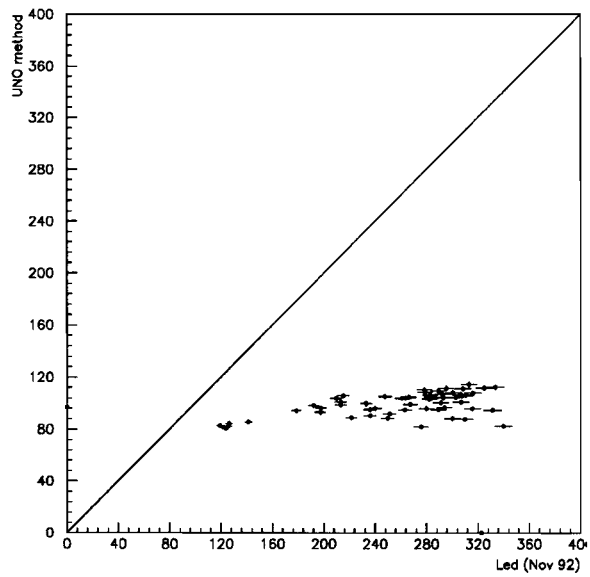

Figure 4.12: UNO–LED n_{pe} correlation, HAC tubes, RCAL 10.

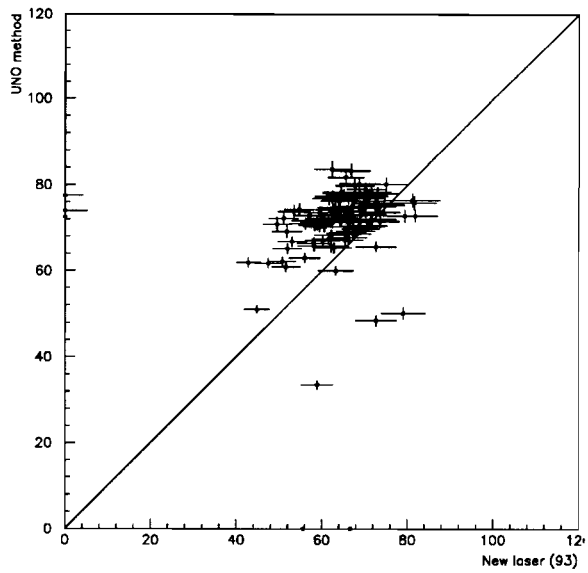

Figure 4.13: UNO–Laser (93) n_{pe} correlation, EMC tubes, BCAL 10.

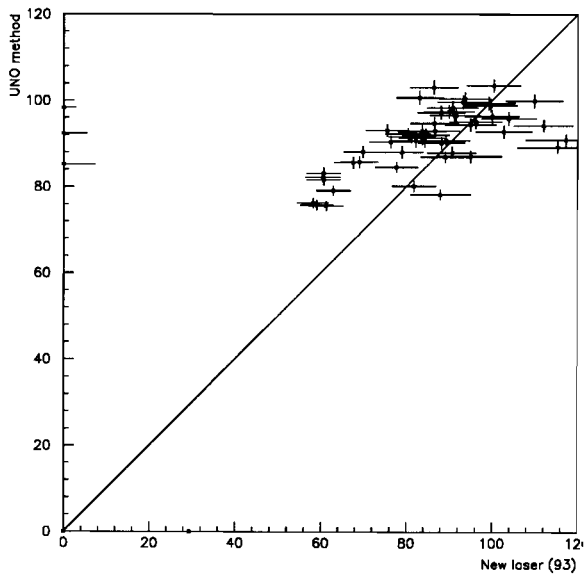

Figure 4.14: UNO–Laser (93) n_{pe} correlation, HAC tubes, BCAL 10.

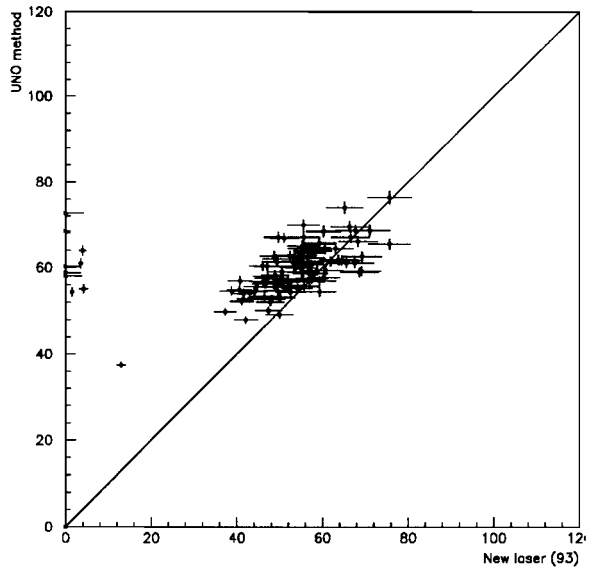

Figure 4.15: UNO–Laser (93) n_{pe} correlation, EMC tubes, BCAL 29.

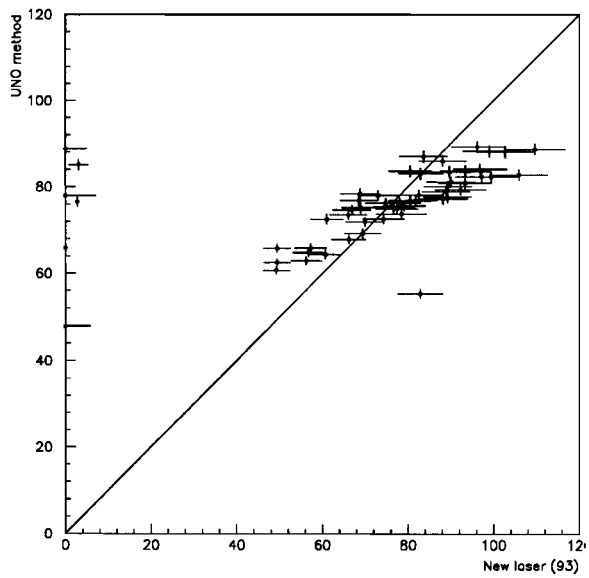

Figure 4.16: UNO–Laser (93) n_{pe} correlation, HAC tubes, BCAL 29.

4.3 Conclusions and Outlook

The Hall II method, although somewhat involved in its application, is not completely intractable and yields reasonable results that compare favorably with other methods such as LED, although some systematic effect remains. It is not clear whether this is due to the LED or Hall II or a combination of both. However the method seems internally consistent as more recent laser data appear to agree rather well with hall II results. It will be of interest to see any effects due to the new Nd-YAG laser. With its simplified operation, it will be possible to take frequent laser runs, thus making the laser a possible tool for short term as well as long term monitoring of the PMT gain.

Although the UNO method has a physically intuitive and appealing motivation as well possessing the advantage of being almost trivial to apply in practice, it suffers the principal drawback that it does not produce anywhere near the same numbers as the laser or LED methods in the F/RCAL although there is somewhat better agreement in the BCAL. It seems clear that the single photoelectron assumption most likely does not hold if the light transmission through the scintillator, WLS and light guides is "too" efficient. The extraction of the observed rate of UNO pulses does not suffer from this difficulty, however, and could also be used as a monitor of the readout stability, as it essentially measures the stability of the optical readout up to the PMT. The apparent scaling problem in the FCAL warrants further investigation and it would be interesting to determine if the BCAL rates scale as we expect, however it is not as simple to determine as in the FCAL due to BCAL's projective geometry.

Another possible source of systematic error in the UNO method may be due to the PMT base noise. Recall that the "σ_0" approach assumes that the PMT base noise is flat at high I_{UNO}, if it in fact has another dependence on I_{UNO} (or equivalently, the high voltage) this may lead to an overestimation of the UNO width and thus an underestimation of n_{pe}.

Work has been started investigating modifications to the model, taking into ac-

count the possibility of multiple photoelectrons produced by the UNO pulses, as well as the PMT base noise, however this work is still very preliminary.

List of Figures

List of Tables

Bibliography

[1] A. Bernstein et al.; Calibration of the Calorimeter Readout Electronics Version 1.0; ZEUS 91-114 (1991)

[2] U. Behrens et al.; Quality Control and Calibration of the ZEUS Forward and Rear Calorimeters with cobalt-60 Sources; DESY-92-064 (1992)

[3] R. Brun and J. Zoll; PAW–Physics Analysis Workstation, CERN program library entry Q121; CERN, Geneva (1992)

[4] A. Caldwell et al.; Design and Implementation of a High Precision Readout System for the ZEUS Calorimeter; ZEUS 92-022 (1991)

[5] A. Caldwell et al.; Measurement of the Background Signal (Noise) from DU– Computer Modeling of the DU Noise; ZEUS 87-017

[6] A. Caldwell; private communication

[7] G. Cases et al.; Calibration of the Forward and Rear ZEUS Calorimeter using Cosmic Ray Muons; ZEUS 92-068

[8] G. Drews et al.; Experimental Determination of Sampling Fluctuations in Uranium and Lead Hadronic Calorimeters; DESY 89-159 (1989)

[9] F. Halzen and A. D. Martin; Quarks and Leptons: An Introductory Course in Modern Particle Physics; Wiley (1984)

[10] D. Hanna; Checkout of the YQL-102 (Nd-YAG) Laser; unpublished (1993)

[11] J. Krüger; The Uranium Scintillator Calorimeter for the ZEUS Detector at the Electron-Proton Collider HERA; DESY F35-92-02

[12] A. Kruse; private communication

[13] W. R. Leo; Techniques for Nuclear and Particle Physics experiments; Springer-Verlag (1987)

[14] R. Meijer-Drees; private communication

[15] J. W. Mitchell et al.; The Pulsed Light Calibration System of the ZEUS Calorimeter; Nucl. Phys. B (Proc. Suppl.) 32 (1993) 106-114

[16] W.R. Nelson, H. Hirayama, and D.W.O. Rogers; SLAC Report 165, Stanford: SLAC (1985)

[17] D. H. Perkins; Introduction to High Energy Physics; Addison-Wesley (1986)

[18] RTC; Photomultiplicateurs; (1981)

[19] Proceedings of the study of an ep facility for Europe; Ed. U. Amaldi; DESY 79/48 (1979) 391-394

[20] Proceedings of the HERA Workshop Vol. 1 and 2; Ed. R.D. Peccei; DESY (1988)

[21] Review of Particle Properties; Phys. Lett. 170B (1986) 45;

[22] R. Ullmann; Diplom Arbeit; Universität Freiburg (1991)

[23] R. Ullmann; private communication

[24] H. van der Lugt et al.; Transputer network for Calorimeter Readout and Calorimeter Second Level Trigger; ZEUS 90-14 (1990)

[25] G. Wolf; First Results from HERA; DESY 92-190 (1986)

[26] G. Wolf; HERA: Physics, Machine and Experiments; DESY 86-089 (1986)

[27] R. Wigmans; Energy Loss of Particles in Dense Matter- Calorimetry; NIKHEF-H/87-12 (1987)

[28] R. Wigmans; On the Energy Resolution of Uranium and other Hadronic Calorimeters; Nucl. Instr. and Meth. A259 (1987) 389

[29] R. Yoshida; The ZEUS Uranium Calorimeter: Main Characteristics and First Operating Experience; NIKHEF-H/92-15 (1992)

[30] ZEUS Collaboration; Search for excited electrons using the ZEUS dectector; DESY 93-075 (1993)

[31] ZEUS Collaboration; Search for leptoquarks with the ZEUS detector; DESY 93-017 (1993)

[32] ZEUS Collaboration; The ZEUS Detector, Status Report 1989 (1989)

[33] ZEUS Collaboration; The ZEUS Detector, Status Report 1993 (1993)

[34] ZEUS Calorimeter Group; Construction and Beam Test of the ZEUS Forward and Rear Calorimeter; (1991)

[35] ZEUS Laser Group; Determination of Photoelectrons for FCAL Modules with Hall 2 Laser Data; unpublished (1992)